

150844

**FRACTURE BEHAVIOUR OF WELDED
NODULAR CAST IRON**

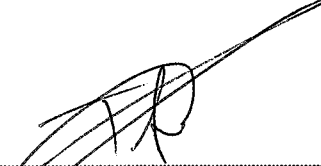
**A Thesis Submitted to the
Graduate School of Natural and Applied Sciences of
Dokuz Eylül University
In Partial Fulfillment of the Requirements for
the Degree of Doctor of Philosophy
in Metallurgical and Materials Engineering, Materials Science
Program**

by
Hakan ÇETİNEL
150844

April, 2004
İZMİR

Ph.D. THESIS EXAMINATION RESULT FORM

We certify that we have read the thesis, entitled "FRACTURE BEHAVIOUR OF WELDED NODULAR CAST IRON" completed by HAKAN ÇETİNEL under supervision of PROF. DR. TEVFIK AKSOY and that in our opinion it is fully adequate, in scope and in quality, as a thesis for the degree of Doctor of Philosophy.



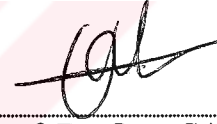
Prof. Dr. Tefvik AKSOY

Supervisor



Prof. Dr. Ahmet ÇAKIR

Jury Member



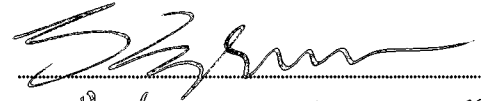
Prof. Dr. Onur SAYMAN

Jury Member



Prof. Dr. A. Ceylan ÇAKIR

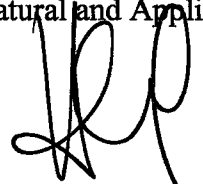
Jury Member



Prof. Dr. Kazım ÖNEL

Jury Member

Approved by the
Graduate School of Natural and Applied Sciences



Prof. Dr. Cahit HELVACI
Director

ACKNOWLEDGMENTS

I am deeply grateful to my supervisor, Prof. Dr. Tevfik AKSOY for his patient supervision, valuable guidance, constructive suggestions and continuous encouragement throughout this study.

I also would like to thank Prof. Dr. Ahmet ÇAKIR and Prof. Dr. Onur SAYMAN for their valuable suggestions, continued interest, and their endless support in my study.

I also wish to express my gratitude to Bahadır UYULGAN and my other colleagues at the Department of Metallurgical and Materials Engineering for their help and support.

Finally, I would like to thank my wife and my parents for their encouragement and continuous moral support.

Hakan ÇETİNEL, İzmir - 2004

ABSTRACT

In this study, fracture behavior of welded nodular cast iron was investigated experimentally and theoretically. Ferritic nodular cast irons were joined by cold arc welding method by using the nickel base electrode as filling material in order to obtain under-matched weldment which yield strength of weld metal is lower than that of base metal. Various regions with different mechanical properties appeared in welded specimens. The mechanical and the metallographical properties of these regions (weld metal, heat-affected zone and base metal) affect the fracture behavior of welded specimens.

In experimental part of the study, firstly, mechanical and metallographical properties of the welded specimens were identified. Then, J-Integral toughness values were determined by fracture toughness tests for different crack locations including base metal, HAZ and weld metal.

In numerical part of the study, finite element (FE) analyses were conducted by fixing 3-D models precracked on different locations. In these models, after stress – strain analyses, stress triaxiality and plastic deformation characteristics around crack tip were determined for each crack locations and different crack sizes. It was found that stress triaxiality and plastic strain values increase with growing crack length. Different regions with different strength levels in weldment, affect the extension of plastic deformation in the models. Hindrance on the extension of plastic deformation at HAZ and diffusion line causes extra increase in stress triaxiality at crack tip.

ÖZET

Bu çalışmada, kaynaklanmış küresel grafitli dökme demirin kırılma davranışı deneysel ve teorik olarak incelenmiştir. Kaynak metali akma mukavemeti esas metalden daha düşük olan alt-uyum kaynağı elde etmek için ferritik küresel grafitli dökme demirler soğuk ark kaynağı metoduyla dolgu maddesi olarak nikel bazlı elektrot kullanılarak birleştirilmiştir. Kaynaklanmış numunelerde farklı mekanik özelliklere sahip çeşitli bölgeler ortaya çıkmaktadır. Bu farklı bölgelerin (kaynak metali, ısı tesiri altında kalmış bölge ve esas metal) mekanik ve metalografik özellikleri kaynaklanmış numunelerin kırılma davranışını etkilemektedir.

Çalışmanın deneysel kısmında, ilk olarak, kaynaklanmış numunelerin mekanik ve metalografik özellikleri tanımlanmıştır. Ardından, kırılma tokluğu deneyleri ile J-integrali kırılma tokluğu değerleri esas metal, ısı tesiri altında kalmış bölge ve kaynak metalini içeren farklı çatlak bölgeleri için belirlenmiştir.

Çalışmanın sayısal kısmında, sonlu elemanlar analizleri farklı bölgelerinde ön çatlaklar içeren 3 boyutlu modeller oluşturularak gerçekleştirilmiştir. Bu modellerde, gerilme - şekil değiştirme analizlerinden sonra çatlak civarındaki üç eksenli gerilme ve plastik deformasyon karakteristikleri her bir çatlak bölgesi ve farklı çatlak boyları için belirlenmiştir. Üç eksenli gerilme ve plastik şekil değiştirme değerlerinin büyüyen çatlak boyuyla arttığı tespit edilmiştir. Kaynaklı birleştirmede farklı mukavemet değerlerine sahip çeşitli bölgeler model içinde plastik deformasyon yayılmasını etkilemektedir. Plastik deformasyon ilerlemesinin ısı tesiri altında kalmış bölgede ve difüzyon çizgisinde engellenmesi çatlak ucunda fazladan bir üç eksenli gerilme artışına neden olmaktadır

CONTENTS

	Page
Contents.....	IV
List of Figures.....	VIII
List of Tables.....	XVIII
Nomenclature.....	XIX

Chapter One INTRODUCTION

1.1 Introduction.....	1
1.2 Previous Works.....	3
1.3 Scope of the Present Study.....	6

Chapter Two NODULAR CAST IRON

2.1 History of Nodular Cast Iron Development.....	7
2.2 The Nodular Cast Iron Advantage.....	7
2.3 A Matter of Confidence.....	9

Chapter Three WELDING OF NODULAR CAST IRON

3.1 Introduction.....	10
-----------------------	----

3.2 Welding.....	13
3.2.1 Arc Welding.....	13
3.2.2 Flux Cored Arc Welding.....	15
3.2.3 Joint Design and Preparation.....	16
3.2.4 Thermal Treatments.....	17

Chapter Four FRACTURE MECHANICS

4.1 Introduction.....	18
4.2 Linear Elastic Fracture Mechanics (LEFM).....	18
4.3 Elastic Plastic Fracture Mechanics.....	22
4.3.1 Formulation of J-Integral.....	24
4.4 Constraint and Triaxiality of Stresses around Crack Tip.....	25

Chapter Five MISMATCHING

5. Mismatching.....	27
---------------------	----

Chapter Six FINITE ELEMENT METHOD

6.1 Introduction.....	29
6.2 Interpolation Concepts In Three Dimension.....	30
6.3 Strain - Displacement Transformation Matrix.....	30
6.4 Evaluation of Stresses.....	31
6.5 Material Nonlinearity in ANSYS Software.....	32
6.5.1 Rate – Independent Plasticity.....	32

6.5.1.1 Yield Criterion.....	33
6.5.1.2 Flow Rule.....	33
6.5.1.3 Hardening Rule.....	34
6.5.2 Plastic Strain Increment.....	34
6.5.3 Specialization for Hardening.....	34

Chapter Seven

EXPERIMENTAL STUDY

7.1 Material.....	37
7.2 Specimen Configurations.....	37
7.3 Tensile Testing.....	38
7.4 Micro-Hardness Testing.....	39
7.5 Microstructural Examination.....	39
7.6 J Fracture Toughness Tests.....	40

Chapter Eight

THEORETICAL STUDY

8.1 FE Model.....	43
8.2 Input Data.....	45
8.2.1. Linear and Nonlinear Material Properties.....	45
8.2.2 Loads.....	48
8.2.3 Annealed Models.....	49

Chapter Nine

RESULTS AND DISCUSSION IN TERMS OF EXPERIMENTAL STUDY

9.1 Tensile Properties.....	51
-----------------------------	----

9.2 Micro-Hardness Values.....	51
9.3 Microstructures.....	52
9.4 Fracture Toughness Properties.....	58

Chapter Ten
RESULTS AND DISCUSSION IN TERMS OF
THEORETICAL STUDY

10.1 Stress Triaxiality and Equivalent Plastic Strain Values around Crack Tip.....	64
10.2 Equivalent Plastic Strain Distribution on the Models.....	97
10.2.1 Even-Matched Models.....	97
10.2.2 Under-Matched Models.....	100
10.2.3 Annealed Models.....	110

Chapter Eleven
CONCLUSIONS

11. Conclusions.....	120
----------------------	-----

Chapter Twelve
FURTHER WORK

12. Further Work.....	123
-----------------------	-----

REFERENCES

References.....	124
-----------------	-----

LIST OF FIGURES

	Page
Figure 2.1 Comparison of the engineering characteristics of nodular cast iron versus competitive ferrous cast materials.....	8
Figure 3.1 Relationship between carbon equivalent and no-crack temperature for cast irons.....	11
Figure 3.2 Schematic representation of the zones in a typical nodular cast iron weldment	12
Figure 3.3 Rotating-bending fatigue strength of welded and unwelded ferritic nodular cast iron.....	14
Figure 3.4 Rotating-bending fatigue strength of welded and unwelded pearlitic nodular cast iron.....	15
Figure 3.5 Joint design improvements.....	17
Figure 4.1 Three modes of loading used in linear elastic fracture mechanics analyses.....	20
Figure 4.2 Stress state in the vicinity of a crack tip showing coordinates.....	21
Figure 4.3 Formation of plastic zone at a crack tip when yielding occurs.....	21
Figure 4.4 Different regimes of a cracked elasto-plastic body. (a) LEFM, (b) EPFM, (c) net section yield, (d) general yield.....	23
Figure 4.5 Co-ordinates and typical contour used to evaluate the J-integral.....	25
Figure 6.1 Uniaxial behaviors for multilinear isotropic hardening and σ_k determination.....	36
Figure 7.1 Configuration of the groove joint.....	38
Figure 7.2 Two different locations where the measurements were made.....	39
Figure 7.3 The four different crack locations.....	40

Figure 7.4 Configuration of the bend specimen.....	41
Figure 7.5 Definition of area for J integral.....	42
Figure 8.1 a) Crack locations and half thickness of the specimen with symmetric cross-section b) FEM mesh in a global scale for the crack location 1....	43
Figure 8.2 a) Details of mesh core for the crack location 1 and b) singular elements around crack tip.....	44
Figure 8.3 Yield strength - micro-hardness relationship.....	46
Figure 8.4 Vickers micro-hardness values in different regions.....	47
Figure 8.5 True stress-true strain values of the different regions.....	48
Figure 8.6 Load vs. crack mouth opening displacement curves obtained in FE analysis and experimental results for crack location 1.....	49
Figure 8.7 True stress – strain curves of different regions on the annealed models..	50
Figure 9.1 The hardness values (a) on the root and (b) on the cap regions.....	52
Figure 9.2 Graphite size and distribution of the graphite nodules in the (a) base metal and (b) the weld metal.....	53
Figure 9.3 EDAX result of electrodes used in welding process.....	54
Figure 9.4 The variations of the nickel and iron amounts on the root region.....	55
Figure 9.5 The variations of the nickel and iron amounts on the cap region.....	55
Figure 9.6 HAZ with coarse grains.....	56
Figure 9.7 SEM micrograph of diffusion region.....	56
Figure 9.8 EBSD image of diffusion region (for FCC).....	57
Figure 9.9 EBSD image of diffusion region (for BCC).....	57
Figure 9.10 Load vs. load line displacement curve of pre-cracked three point bend specimen for location 1.....	58
Figure 9.11 Load vs. crack mouth opening displacement curve of pre-cracked three point bend specimen for location 1.....	59
Figure 9.12 Load vs. crack mouth opening displacement curve of pre-cracked three point bend specimen for location 2.....	59
Figure 9.13 Load vs. crack mouth opening displacement curve of pre-cracked three point bend specimen for location 3.....	60
Figure 9.14 Load vs. crack mouth opening displacement curve of pre-cracked three point bend specimen for location 4.....	60

Figure 9.15 Load versus crack propagation curve of the crack on location 1.....	61
Figure 9.16 Load versus crack propagation curve of the crack on location 2.....	62
Figure 9.17 Load versus crack propagation curve of the crack on location 3.....	62
Figure 9.18 Load versus crack propagation curve of the crack on location 4.....	63
Figure 9.19 J resistance curves for all locations.....	63
Figure 10.1 (a) Stress triaxiality, (b) equivalent plastic strain values along y-axis around crack tip in the centre and on the surface of the under-matched, annealed and even-matched models for 5 mm crack length on the location 1.....	66
Figure 10.2 (a) Stress triaxiality, (b) equivalent plastic strain values along crack front in the centre and on the surface of the under-matched, annealed and even-matched models for 5 mm crack length on the location 1.....	66
Figure 10.3 (a) Stress triaxiality, (b) equivalent plastic strain values along y-axis around crack tip in the centre and on the surface of the under-matched, annealed and even-matched models for 5.05 mm crack length on the location 1.....	67
Figure 10.4 (a) Stress triaxiality, (b) equivalent plastic strain values along crack front in the centre and on the surface of the under-matched, annealed and even-matched models for 5.05 mm crack length on the location 1.....	67
Figure 10.5 (a) Stress triaxiality, (b) equivalent plastic strain values along y-axis around crack tip in the centre and on the surface of the under-matched, annealed and even-matched models for 5.1 mm crack length on the location 1.....	68
Figure 10.6 (a) Stress triaxiality, (b) equivalent plastic strain values along crack front in the centre and on the surface of the under-matched, annealed and even-matched models for 5.1 mm crack length on the location 1.....	68
Figure 10.7 (a) Stress triaxiality, (b) equivalent plastic strain values along y-axis around crack tip in the centre and on the surface of the under-matched, annealed and even-matched models for 5.2 mm	

crack length on the location 1.....69

Figure 10.8 (a) Stress triaxiality, (b) equivalent plastic strain values along crack front in the centre and on the surface of the under-matched, annealed and even-matched models for 5.2 mm crack length on the location 1.....69

Figure 10.9 (a) Stress triaxiality, (b) equivalent plastic strain values along y-axis around crack tip in the centre and on the surface of the under-matched, annealed and even-matched models for 5.85 mm crack length on the location 1.....70

Figure 10.10 (a) Stress triaxiality, (b) equivalent plastic strain values along crack front in the centre and on the surface of the under-matched, annealed and even-matched models for 5.85 mm crack length on the location 1.....70

Figure 10.11 (a) Stress triaxiality, (b) equivalent plastic strain values along y-axis around crack tip in the centre and on the surface of the under-matched, annealed and even-matched models for 5 mm crack length on the location 2.....72

Figure 10.12 (a) Stress triaxiality, (b) equivalent plastic strain values along crack front in the centre and on the surface of the under-matched, annealed and even-matched models for 5 mm crack length on the location 2.....72

Figure 10.13 (a) Stress triaxiality, (b) equivalent plastic strain values along y-axis around crack tip in the centre and on the surface of the under-matched, annealed and EM models for 5.05 mm crack length on the location 2.....73

Figure 10.14 (a) Stress triaxiality, (b) equivalent plastic strain values along crack front in the centre and on the surface of the under-matched, annealed and even-matched models for 5.05 mm crack length on the location 2.....73

Figure 10.15 (a) Stress triaxiality, (b) equivalent plastic strain values along y-axis around crack tip in the centre and on the surface of the under-matched, annealed and even-matched models for 5.1 mm

crack length on the location 2.....	74
Figure 10.16 (a) Stress triaxiality, (b) equivalent plastic strain values along crack front in the centre and on the surface of the under-matched, annealed and even-matched models for 5.1 mm crack length on the location 2.....	74
Figure 10.17 (a) Stress triaxiality, (b) equivalent plastic strain values along y-axis around crack tip in the centre and on the surface of the under-matched, annealed and even-matched models for 5.2 mm crack length on the location 2.....	75
Figure 10.18 (a) Stress triaxiality, (b) equivalent plastic strain values along crack front in the centre and on the surface of the under-matched, annealed and even-matched models for 5.2 mm crack length on the location 2.....	75
Figure 10.19 (a) Stress triaxiality, (b) equivalent plastic strain values along y-axis around crack tip in the centre and on the surface of the under-matched, annealed and even-matched models for 5.85 mm crack length on the location 2.....	76
Figure 10.20 (a) Stress triaxiality, (b) equivalent plastic strain values along crack front in the centre and on the surface of the under-matched weld, annealed and even-matched models for 5.85 mm crack length on the location 2.....	76
Figure 10.21 (a) Stress triaxiality, (b) equivalent plastic strain values along y-axis around crack tip in the centre and on the surface of the under-matched, annealed and even-matched models for 5 mm crack length on the location 3.....	78
Figure 10.22 (a) Stress triaxiality, (b) equivalent plastic strain values along crack front in the centre and on the surface of the under-matched, annealed weld and even-matched models for 5 mm crack length on the location 3.....	78
Figure 10.23 (a) Stress triaxiality, (b) equivalent plastic strain values along y-axis around crack tip in the centre and on the surface of the under-matched, annealed and even-matched models for 5.05 mm	

crack length on the location 3.....	79
Figure 10.24 (a) Stress triaxiality, (b) equivalent plastic strain values along crack front in the centre and on the surface of the under-matched, annealed and even-matched models for 5.05 mm crack length on the location 3.....	79
Figure 10.25 (a) Stress triaxiality, (b) equivalent plastic strain values along y-axis around crack tip in the centre and on the surface of the under-matched, annealed and even-matched models for 5.1 mm crack length on the location 3.....	80
Figure 10.26 (a) Stress triaxiality, (b) equivalent plastic strain values along crack front in the centre and on the surface of the under-matched, annealed and even-matched models for 5.1 mm crack length on the location 3.....	80
Figure 10.27 (a) Stress triaxiality, (b) equivalent plastic strain values along y-axis around crack tip in the centre and on the surface of the under-matched, annealed and even-matched models for 5.2 mm crack length on the location 3.....	81
Figure 10.28 (a) Stress triaxiality, (b) equivalent plastic strain values along crack front in the centre and on the surface of the under-matched, annealed and even-matched models for 5.2 mm crack length on the location 3.....	81
Figure 10.29 (a) Stress triaxiality, (b) equivalent plastic strain values along y-axis around crack tip in the centre and on the surface of the under-matched, annealed and even-matched models for 5.85 mm crack length on the location 3.....	82
Figure 10.30 (a) Stress triaxiality, (b) equivalent plastic strain values along crack front in the centre and on the surface of the under-matched, annealed and even-matched models for 5.85 mm crack length on the location 3.....	82
Figure 10.31 (a) Stress triaxiality, (b) equivalent plastic strain values along y-axis around crack tip in the centre and on the surface of the under-matched, annealed and even-matched models for 5 mm	

crack length on the location 4.....	84
Figure 10.32 (a) Stress triaxiality, (b) equivalent plastic strain values along crack front in the centre and on the surface of the under-matched, annealed and even-matched models for 5 mm crack length on the location 4.....	84
Figure 10.33 (a) Stress triaxiality, (b) equivalent plastic strain values along y-axis around crack tip in the centre and on the surface of the under-matched, annealed and even-matched models for 5.05 mm crack length on the location 4.....	85
Figure 10.34 (a) Stress triaxiality, (b) equivalent plastic strain values along crack front in the centre and on the surface of the under-matched, annealed and even-matched models for 5.05 mm crack length on the location 4.....	85
Figure 10.35 (a) Stress triaxiality, (b) equivalent plastic strain values along y-axis around crack tip in the centre and on the surface of the under-matched, annealed and even-matched models for 5.1 mm crack length on the location 4.....	86
Figure 10.36 (a) Stress triaxiality, (b) equivalent plastic strain values along crack front in the centre and on the surface of the under-matched, annealed and even-matched models for 5.1 mm crack length on the location 4.....	86
Figure 10.37 (a) Stress triaxiality, (b) equivalent plastic strain values along y-axis around crack tip in the centre and on the surface of the under-matched, annealed and even-matched models for 5.2 mm crack length on the location 4.....	87
Figure 10.38 (a) Stress triaxiality, (b) equivalent plastic strain values along crack front in the centre and on the surface of the under-matched, annealed and even-matched models for 5.2 mm crack length on the location 4.....	87
Figure 10.39 (a) Stress triaxiality, (b) equivalent plastic strain values along y-axis around crack tip in the centre and on the surface of the under-matched, annealed and even-matched models for 5.85 mm	

crack length on the location 4.....	88
Figure 10.40 (a) Stress triaxiality, (b) equivalent plastic strain values along crack front in the centre and on the surface of the under-matched, annealed and even-matched models for 5.85 mm crack length on the location 4.....	88
Figure 10.41 The results of stress triaxiality values at 0.01 mm crack ahead vs. crack lengths in the center of the under-matched, annealed and even-matched specimens for the crack location 1.....	89
Figure 10.42 The results of stress triaxiality values at 0.01 mm crack ahead vs. crack lengths in the center of the under-matched, annealed and even-matched specimens for the crack location 2.....	90
Figure 10.43 The results of stress triaxiality values at 0.01 mm crack ahead vs. crack lengths in the center of the under-matched, annealed and even-matched specimens for the crack location 3.....	90
Figure 10.44 The results of stress triaxiality values at 0.01 mm crack ahead vs. crack lengths in the center of the under-matched, annealed and even-matched specimens for the crack location 4.....	91
Figure 10.45 The results of stress triaxiality values at 0.01 mm crack ahead vs. crack lengths in the center of the (a) under-matched (b) annealed specimens comparing even-matched specimens for the all crack locations.....	92
Figure 10.46 The results of equivalent plastic strain values at 0.01 mm crack ahead vs. crack lengths in the center of the under-matched, annealed and even-matched specimens for the crack location 1.....	93
Figure 10.47 The results of equivalent plastic strain values at 0.01 mm crack ahead vs. crack lengths in the center of the under-matched, annealed and even-matched specimens for the crack location 2.....	94
Figure 10.48 The results of equivalent plastic strain values at 0.01 mm crack ahead vs. crack lengths in the center of the under-matched, annealed and even-matched specimens for the crack location 3.....	94
Figure 10.49 The results of equivalent plastic strain values at 0.01 mm	

	crack ahead vs. crack lengths in the center of the under-matched, annealed and even-matched specimens for the crack location 4.....	95
Figure 10.50	The results of equivalent plastic strain values at 0.01 mm crack ahead vs. crack lengths in the center of the (a) under-matched (b) annealed specimens comparing even-matched specimens for the all crack locations.....	96
Figure 10.51	Equivalent plastic strain distribution (a) on the surface and (b) in the center of the even-matched model for 5 mm crack length.....	98
Figure 10.52	Equivalent plastic strain distribution (a) on the surface and (b) in the center of the even-matched model for 5.85 mm crack length.....	99
Figure 10.53	Equivalent plastic strain distribution (a) on the surface and (b) in the center of the under-matched model for 5 mm crack length in the crack location 1.....	101
Figure 10.54	Equivalent plastic strain distribution (a) on the surface and (b) in the center of the under-matched for 5.85 mm crack length model in the crack location 1.....	102
Figure 10.55	Equivalent plastic strain distribution (a) on the surface and (b) in the center of the under-matched for 5 mm crack length model in the crack location 2.....	103
Figure 10.56	Equivalent plastic strain distribution (a) on the surface and (b) in the center of the under-matched model for 5.85 mm crack length in the crack location 2.....	104
Figure 10.57	Equivalent plastic strain distribution (a) on the surface and (b) in the center of the under-matched model for 5 mm crack length in the crack location 3.....	106
Figure 10.58	Equivalent plastic strain distribution (a) on the surface and (b) in the center of the under-matched model for 5.85 mm crack length in the crack location 3.....	107
Figure 10.59	Equivalent plastic strain distribution (a) on the surface and (b) in the center of the under-matched model for 5 mm crack	

length in the crack location 4.....	108
Figure 10.60 Equivalent plastic strain distribution (a) on the surface and (b) in the center of under-matched model for 5.85 mm crack length in the crack location 4.....	109
Figure 10.61 Equivalent plastic strain distribution (a) on the surface and (b) in the center of the annealed model for 5 mm crack length in crack the location 1.....	111
Figure 10.62 Equivalent plastic strain distribution (a) on the surface and (b) in the center of the annealed model for 5.85 mm crack length in the crack location 1.....	112
Figure 10.63 Equivalent plastic strain distribution (a) on the surface and (b) in the center of the annealed model for 5 mm crack length in the crack location 2.....	113
Figure 10.64 Equivalent plastic strain distribution (a) on the surface and (b) in the center of the annealed model for 5.85 mm crack length in the crack location 2.....	114
Figure 10.65 Equivalent plastic strain distribution (a) on the surface and (b) in the center of the annealed model for 5 mm crack length in the crack location 3.....	116
Figure 10.66 Equivalent plastic strain distribution (a) on the surface and (b) in the center of the annealed model for 5.85 mm crack length in the crack location 3.....	117
Figure 10.67 Equivalent plastic strain distribution (a) on the surface and (b) in the center of the annealed model for 5 mm crack length in the crack location 4.....	118
Figure 10.68. Equivalent plastic strain distribution (a) on the surface and (b) in the center of the annealed model for 5.85 mm crack length in the crack location 4.....	119

LIST OF TABLES

	Page
Table 3.1 Average transverse tensile properties of short-arc mig-welds between 25mm thick plates.....	14
Table 3.2 Mechanical properties of joints welded with flux-cored wire Ni-Rod FC55: base material ASTM grade 60/45/10 nodular cast iron.....	16
Table 7.1 Chemical composition of test material (mass percent).....	37
Table 7.2 Mechanical properties of the nodular iron.....	37
Table 7.3 Welding parameters.....	38
Table 8.1 Micro-hardness values and entered data of WM, BM and HAZ.....	47
Table 8.2 Microhardness and calculated yield strengths of different regions on the annealed model.....	50
Table 9.1 Mechanical properties of the weld metal.....	51
Table 9.2 Chemical composition of the weld metal.....	54

NOMENCLATURE

a	: Crack length
B	: Specimen thickness
$[B]$: Transformation matrix
$[D]$: Elasticity matrix
E	: Young's modulus
h	: Stress triaxiality parameter
J	: J-integral
K	: Linear elastic stress intensity factor
$[K]$: stiffness matrix
M	: Mismatch factor
n	: Hardening exponent
P	: Applied force
W	: Width of the specimen
δ	: Displacement
ε	: Strain
ν	: Poisson's ratio
σ	: Stress
σ_e	: Equivalent von-Mises stress
σ_h	: Hydrostatic (mean normal) stress
σ'_i	: Deviatoric stress
σ_i	: Principal stress ($i = 1-3$)
σ_0	: Yield stress, general

Abbreviations

BM	: Base metal
CE _{CI}	: Carbon equivalent for cast iron
CMOD	: Crack mouth opening displacement
CTOD	: Crack tip opening displacement
EBSD	: Electron back-scatter diffraction
EM	: Even-matched weldment
EPS	: Equivalent plastic strain
FE	: Finite element
HAZ	: Heat-affected zone
HV	: Vickers hardness
LLD	: Load line displacement
SEN(B)	: Single edge notched bar in three point bending
ST	: Stress triaxiality
UM	: Under-matched weldment
WM	: Weld metal

CHAPTER ONE

INTRODUCTION

Introduction

Nodular cast iron also known as Spheroidal-Graphite Cast Iron, Ductile Iron and Nodular Iron is a modern engineering material distinguished by its high strength, toughness, hardenability, hot workability and ductility combined with excellent casting properties (low melting temperature, good fluidity) and good machinability. Therefore, such material can economically replace steel in a very wide variety of applications. Additionally, cheapness, good wear resistance, high damping capacity, perfect heat resistance properties make them excellent candidate material for structural applications (Huke, E. E. & Udin, H., 1953; Minkoff, I., 1983; Elliot, R., 1988). For example, nodular irons are employed in pipe and automotive industry as part of crank shafts, cam shafts, steering knuckles for disc steering brakes, exhaust manifold, ring gears and pinions (ASM, 1997). In the past 40 years the use of nodular cast iron has grown rapidly, mainly through conversions from gray and malleable iron castings and steel castings, forgings and fabrications. Nodular cast iron has offered the design engineer a combination of versatility and properties not available in any of its rivals so it has been successful. Its castability, machinability, damping properties, and economy of production are almost equal to gray iron's properties, but its mechanical properties - strength, wear resistance, fatigue strength, toughness and ductility are competitive with many cast, forged and fabricated steel components. In summary, nodular cast iron has been successful because it has offered the designer superior value - higher quality and performance at lower cost (Karsay, S.I., 1972; Morrison, J.C. & Smith, K.J., 1989).

It is generally known that a welded joint can be regarded as a structure with hybrid material properties due to the microstructural differences in the base metal (BM), weld metal (WM) and the heat affected zone (HAZ). Properties such as strength, toughness and ultimate tensile strength are distinctly different for each of these regions. Moreover, within the HAZ itself and across the fusion line, there exists a coarse grain (CGHAZ) region that displays peak hardening behavior implying highly brittle material properties (Kocak, M. & Denys, R., 1995).

On the other hand, when a mismatched welded joint is subjected to static or dynamic loads, residual stresses may occur in weld area. These residual stresses cause a crack occurrence in welded joint and the presence of a crack in mismatched weld influences the deformation characteristics of the weld joint. Because of these reasons, the strength mismatch significantly affects deformation and fracture behaviour of the welded joints. Therefore, the adequate crack resistance properties of each part of the welded joint (base metal, weld metal and HAZ) are required in addition to tensile strength properties for safety analysis (Sedmak, S. et al., 1979).

A lot of research has been undertaken to evaluate the toughness properties of welded joints by application of fracture mechanics. It has been shown for base materials that the fracture mechanics philosophy works quite well. Fracture mechanics leads to toughness parameters of the base material which can be used to predict the safety of a construction. Some specific problems occur if fracture mechanics is applied when examining the toughness properties of welded joints. These problems are mainly caused by the great differences in material parameters and residual stresses (Thaoulow, C. et al., 1999).

Problems occur if the existing failure assessment concepts based on the fracture mechanics philosophy are used to predict the behaviour of welded constructions. For optimum efficiency of construction materials a quantification of the requirements for the material and its properties must be precisely laid down. Therefore the influence of the materials' inhomogeneity on deformation and fracture behaviour should be described exactly. Elastic-plastic finite element calculations should contribute to a

better understanding of the deformation process at the crack tip in inhomogeneous material zones. Numerical solutions could allow an exact failure prediction of welded constructions (Heuser, A. et al., 1987).

1.1. Previous Works

Weldability of nodular iron depends on its original matrix (Pease, G. R., 1960; Voight, R.C. & LoperJR., C. R., 1983; Ishizaki, K. et al., 1984; Elliot, R., 1988; Ogi, K. et al., 1988; Kiser, S. D. & Irving, B., 1993), chemical composition (Pease, G. R., 1960; Ishizaki, K. et al., 1984; Ya, S. K. & Loper Jr., C. R., 1988), mechanical properties, welding process and working conditions [Voight, R.C. & LoperJR., C. R., 1983; Hallen, G., 1984; Ishizaki, K. et al., 1984; Kelly, J. J. et al., 1985; Ya, S. K. & Loper Jr., C. R., 1988; McKeown, D., 1990). The formation of martensite in the Heat Affected Zone (HAZ), and the development of hard, brittle iron carbide in the zone of partial fusion are two factors that determine the poor weldability of ductile iron (Pease, G. R., 1960; Nippes, E. F., 1960; Megahed, H., 1995). Most of the welding performed on cast iron is repair welding. It is either the repair of discontinuities produced during the cast process or those developed in cast component itself while in service (Kiser, S. D. & Irving, B., 1993).

All weld joints have bi-material nature. In many cases, the yield strength levels of the different parts of the welded joint can differ significantly. This strength mismatching occurs as over-matched (OM) (i.e., weld metal has higher strength than the base metal) and under-matched (UM) welds. However, Under-matched weldments are recommended for high-strength low-alloy (HSLA) steel in order to avoid cold crack (Sato, K. & Toyoda, M., 1975). Even this case, the occurrence of defects or short cracks cannot be completely excluded in reality (Nichols, R.W., 1984; Reed, R.P. et al., 1984).

Schwalbe et al. (Schwalbe, K.-H. & Cornec, A., 1991) and Kocak et al. (Kocak et al., 1989) presented the so-called Engineering Treatment Model (ETM) for

measuring the crack tip opening displacement (CTOD) for weldments. This model provides analytical expressions to compute the CTOD for matched, overmatched and undermatched welds at loads below the yield strength of the weld, between the yield strength of the weld and that of the base metal and above the yield strength of the base metal in the case of undermatching. The reverse order holds for the overmatching. Some of the criticism this model has received is that it is too simplistic and does not provide reliable results for materials with large hardening behavior. Much work on welding has been done by Toyoda and coworkers (Toyoda, M. & Minami, F., 1989) and Satoh et al. (Satoh, K. & Toyoda, M., 1975). They have produced information on the fracture toughness evaluations of different weldments. They have performed significant number of tests for fracture toughness of HAZ using a modified CTOD procedure. They have concluded that in most cases, the CTOD testing does not always reflect the fracture toughness of the material at the crack tip. This reflects the drastic difference in microstructural properties of a growing crack in the HAZ. Kirk and Dodds (Kirk, M.T. & Dodds, R.H., 1991) have also investigated the influence of weld strength mismatch on crack tip constraint for different weld mismatch conditions. Although they have presented some interesting results regarding the constraint effect in finite three point bend specimens, their analysis is not simple enough for practical engineering problems. Fracture behavior of undermatched weld in presence of short surface cracks was addressed by Petrovski et al. (Petrovski, B. et al., 1991). Their results were obtained in terms of the J-integral on tensile specimens with different crack locations. The experimental data were not sufficiently accurate to describe the HAZ fracture behavior and they have concluded that is not possible to generalize a fracture scheme without considering the specific performance requirements for any particular weld joint.

Additionally, the presence of micro- and macro-heterogeneities of the welded joints, caused by different microstructures and mechanical properties of base metal, weld metal and HAZ develops an unequal plastic strain distribution in real structures (Sedmak, S. et al., 1979). If the base metal has a higher strength than the weld deposit (weld metal under-matching), fracture of transverse butt joints normally takes place in the weld metal. So, the presence of a defect or crack in mismatched weld can

significantly influence the deformation behaviour of the weld joint. Therefore, fracture characteristics of the mismatched welds should carefully be studied with realistic crack configurations and different crack locations. Some researchers have recently conducted analysis by examining small and large scales specimens to clarify the effect of mismatching on global deformation and on fracture mechanics parameters, CTOD and J-integral characterizing crack initiation, growth and instability in many structural materials (Kocak, M. et al., 1989; Kocak, M. et al., 1990; Petrovski, B. & Sedmak, S., 1990; Denys, R. M., 1990; O'Dowd, N. P. & Shih, F., 1991; Fu, J.Q. & Shi, Y. W., 1996; Thaulow, C. et al., 1997; Xue, H. & Shi, Y., 1998; Kim, Y-J. & Schwalbe, K., 2001; Kim, Y.-J., 2002).

A study on HSLA steel plates have presented that if a defect exists in the UM weld, a combination of the low weld metal toughness and strain concentration in the weld metal lead to the poor fracture performance. Even a 6 percent over-matched weld provided an effective shielding to the small surface crack from applied plastic strains. This beneficial effect was pronounced particularly for small HAZ crack: this effect was, however lost for large crack (Petrovski, B. & Kocak, M., 1994).

The dominance of J-based (Rice, J.R., 1968) HRR singularity fields (Hutchinson, J.W., 1968; Rice, J.R. & Rosengren, G.F., 1968) in a near crack-tip zone depends upon specimen geometry and loading conditions (McMeeking, R.M. et al., 1979; Shih, C.F. & German, M.D., 1981; Shih, C.F., 1985). The varied ability of attaining HRR dominance at crack tips of different specimens is attributed to the difference in crack tip "constraint". One of the most widely used constraint parameter is the stress triaxiality, which is defined by the ratio of hydrostatic stress, $\sigma_m = 1/3\sigma_{kk}$, to the Mises equivalent tensile stress, σ_e (Sommer, E. & Aurich, D., 1991; Brocks, W. & Künecke, G., 1991). High constraint is associated with high values of σ_m / σ_e . High crack-tip constraint is often found in specimens with sufficiently deep cracks under predominantly bending load and contained yielding. Low constraint is often associated with specimens of relatively shallow cracks under predominantly tensile loading. Low constraint generally manifests itself in high crack tip ductility and high macroscopic toughness.

2.2. Scope of the Present Study

In this study, the fracture behavior of under-matched welded nodular iron with various cracks in different regions including weld metal and HAZ was investigated experimentally to determine J integral values. In order to use in theoretical study, in addition to J resistance curves, load versus crack growth and load versus crack mouth opening displacement curves were obtained by experimental study. In theoretical study, finite element (FE) analyses were done by fixing 3-D models precracked on different locations including base metal, weld metal and HAZ. In these models, after stress – strain analyses, stress triaxiality (ST) and plastic deformation characteristics around crack tip were determined for each crack locations and different crack sizes. It was found that stress triaxiality and plastic strain values increase with growing crack length. Different regions (base metal, weld metal and HAZ) with different strength levels, affect the extension of plastic deformation in the model. Hindrance on the extension of plastic deformation at HAZ and diffusion line causes extra increase in stress triaxiality at crack tip.

CHAPTER TWO

NODULAR CAST IRON

2.1 History of Nodular Cast Iron Development

In spite of the progress achieved during the first half of the last century in the development of gray and malleable irons, foundrymen continued to search for the ideal cast iron - an as-cast "gray iron" with mechanical properties equal or superior to Malleable Iron. J.W. Bolton, speaking at the 1943 Convention of the American Foundrymen's Society (AFS), made some statements on control of graphite shape. A few weeks later, in the International Nickel Company Research Laboratory, Keith Dwight Millis made a ladle addition of magnesium (as a copper-magnesium alloy) to cast iron and justified Bolton's optimism - the solidified castings contained not flakes, but nearly perfect spheres of graphite. Nodular cast iron (ductile iron) was born! Five years later, at the 1948 AFS Convention, Henton Morrogh of the British Cast Iron Research Association announced the successful production of spherical graphite in hypereutectic gray iron by the addition of small amounts of cerium (Everest, A.B., 1950; Bornstein, H., 1957).

2.2 The Nodular Cast Iron Advantage

The advantages of nodular cast iron which have led to its success are numerous, but they can be summarized easily - versatility, and higher performance at lower cost. As illustrated in Figure 2.1, other members of the ferrous casting family may have individual properties which might make them the material of choice in some applications, but none have the versatility of nodular cast iron, which often provides the designer with the best combination of overall properties. This versatility is

especially evident in the area of mechanical properties where ductile iron offers the designer the option of choosing high ductility, with grades guaranteeing more than 18% elongation, or high strength, with tensile strengths exceeding 825 MPa. Austempered Ductile Iron (ADI), offers even greater mechanical properties and wear resistance, providing tensile strengths exceeding 1600 MPa.

Gray

Characteristic	Ductile Iron	Malleable Iron	Grey Iron	0.3% C Cast Steel	White Iron
Castability					
Ease of Machining					NA
Vibration Damping					
Surface Hardenability					NA
Modulus of Elasticity					NA
Impact Resistance					NA
Corrosion Resistance					
Strength/Weight					NA
Wear Resistance					
Cost of Manufacture					


BEST  WORST

Figure 2.1. Comparison of the engineering characteristics of nodular cast iron versus competitive ferrous cast materials.

In addition to the cost advantages offered by all castings, ductile iron, when compared to steel and malleable iron castings, also offers further cost savings. Like most commercial cast metals, steel and malleable iron decrease in volume during solidification, and as a result, require attached reservoirs (feeders or risers) of liquid metal to offset the shrinkage and prevent the formation of internal or external shrinkage defects. The formation of graphite during solidification causes an internal expansion of ductile iron as it solidifies and as a result, it may be cast free of

significant shrinkage defects either with feeders that are much smaller than those used for malleable iron and steel or, in the case of large castings produced in rigid molds, without the use of feeders. The reduction or elimination of feeders can only be obtained in correctly design castings. This reduced requirement for feed metal increases the productivity of nodular cast iron and reduces its material and energy requirements, resulting in substantial cost savings. The use of the most common grades of nodular cast iron "as-cast" eliminates heat treatment costs, offering a further advantage (Isleib, C. & Savage, R., 1957; Simpson, B.L., 1969; Karsay, S.I., 1972; Marston, G.J., 1990).

2.3 A Matter of Confidence

The automotive industry has expressed its confidence in nodular cast iron through the extensive use of this material in safety related components such as steering knuckles and brake calipers. These and other automotive applications are used "as-cast". One of the most critical materials applications in the world is in containers for the storage and transportation of nuclear wastes. The nodular cast iron nuclear waste container is another example of the ability of nodular cast iron to meet and surpass even the most critical qualification tests for materials performance. The weight range of possible castings can be from less than 28 grams to more than 200 tons. Section size can be as small as 2 mm to more than 1/2 meter in thickness (Kinney, K. E. et al., 1984; Venugopalan D. & Alagarsamy, A., 1990).

CHAPTER THREE

WELDING OF NODULAR CAST IRON

3.1. Introduction

Although the complex shapes produced by the casting process have enabled castings to replace many fabricated components, there are many applications in which, for economic or engineering reasons, castings themselves become part of a fabrication and are joined to other castings or other materials. Although often more cost-effective than steel castings and forgings, nodular cast irons have not been used in some applications requiring joining by welding because they have been considered difficult to weld. This poor weldability of nodular cast iron is partly fact but primarily misconception. When ductile iron castings are repaired or joined by fusion welding their high carbon content can cause the formation of carbides in the fusion zone (FZ) and martensite in both the FZ and heat affected zone (HAZ) adjacent to the FZ. The formation of hard brittle phases in the FZ and HAZ can cause a significant deterioration in both machinability and mechanical properties.

Following an investigation into the weldability of various types of cast irons, the American Welding Society Committee on Welding Cast Irons has developed both a weldability test and a set of recommended practices for welding cast irons. The weldability test consists of the production of carefully controlled autogenous welds (an autogenous weld is one made without filler metal) on test castings preheated to various temperatures and the determination of a minimum temperature, called the "no-crack temperature" above which there is no cracking in the test weld. The committee has found a correlation between the no-crack temperature and the

carbon equivalent (CE_{CI}) formula used to determine the weldability of cast irons and the following formula for CE_{CI} was developed.

$$CE_{CI} = \%C + 0.31 (\%Si) + 0.33 (\%P) + 0.45 (\%S) + 0.028 (\%Mn + \%Mo + \%Cr) - 0.02 (\%Ni) - 0.01 (\%Cu) \quad (3.1)$$

Figure 3.1 shows that there is a good correlation between CE_{CI} and the no-crack temperature for gray, ductile and malleable irons. The autogenous welding method used to obtain this correlation was chosen to simplify and standardize test procedures and is not considered good welding practice for cast irons. For this reason CE_{CI} should be used only to rank weldability rather than determine either absolute weldability or specific preheating conditions. Through the use of welding practices, ductile iron castings have been joined successfully to other ductile iron castings and to steel in the fabrication of automotive and other engineering components. In addition, nonfusion joining processes such as brazing, diffusion bonding and adhesive bonding can be used to produce high quality joints between nodular cast iron and a wide variety of other materials (Harding, R.A., 1987; Voigt, R.C. & Loper, JR., C. R., 1986; Bishel, R.A. & Conaway, H.R., 1976; Kiser, S.D., 1977; Medana, R. et al., 1978).

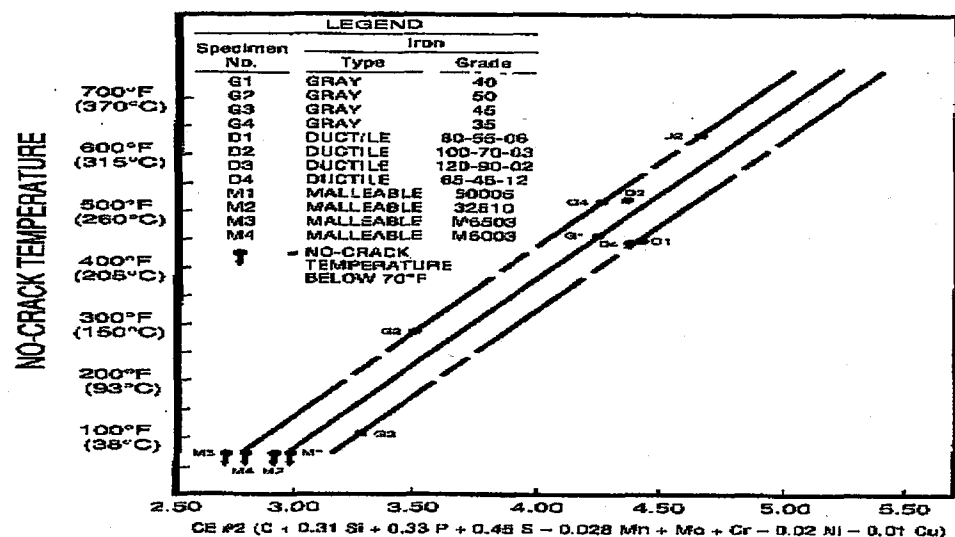


Figure 3.1. Relationship between carbon equivalent and no-crack temperature for cast irons.

Nodular cast irons have various microstructures and physical properties, resulting marked differences in weldability. Variations in thermal gradients across the weldment result in differences in microstructure and properties. The various microstructures are classified into different zones and regions, as shown in Fig. 3.2. The nature and size of these zones are determined by the thermal weld cycle, composition of base metal, and welding consumables. To develop welding procedures that minimize the deleterious effects of these zones, the influences of welding variables on mechanical properties must be considered.

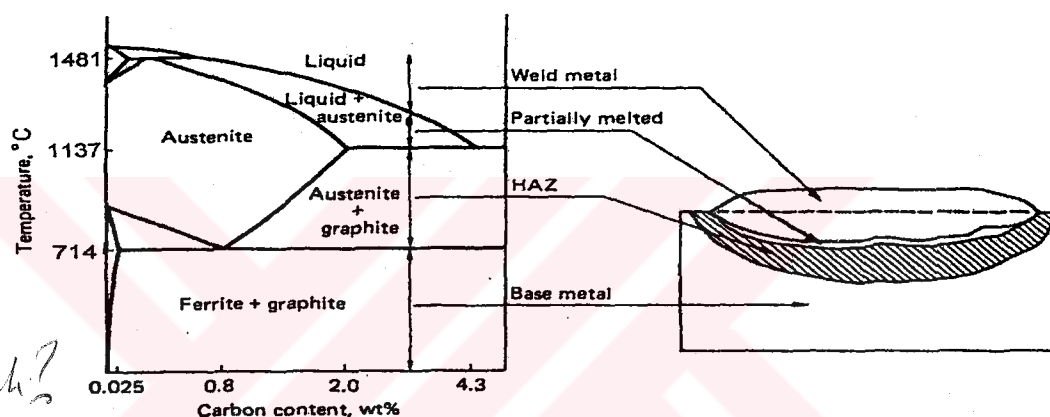


Figure 3.2 Schematic representation of the zones in a typical nodular cast iron weldment

Welding of nodular cast irons is characterized by rapid cooling as compared with cooling rates during casting. Consequently, properties of the weld and the sections of the casting exposed to elevated temperatures (heat-affected zone, or HAZ) differ from those in the remainder of the casting. Portions of the ductile iron HAZ reach temperatures during welding which cause the carbon to diffuse into the austenite. On cooling, this austenite transforms into hard eutectoid decomposition products such as martensite. The amount of martensite formed depends on the nodular cast iron composition and thermal treatment. Ferritic nodular cast irons contain most of their carbon in the form of graphite, which dissolves slowly, thus producing less martensite. The greatest percentage of carbon in pearlitic nodular cast irons is finely divided into the pearlitic structure. This carbon dissolves readily, producing a large

amount of martensite. The brittle martensite may be tempered to lower strength, more ductile structure through (1) preheating and interpass temperature control; (2) multiple-pass welding or (3) post welded heat treatments such as stress-relief annealing.

3.2. Welding

Welding involves the fusion of both a filler metal (welding consumable) and the base metal adjacent to the weld zone. The high carbon content of ductile iron can lead to the formation of carbides in the fusion zone (FZ) and martensite in both the FZ and heat affected zone (HAZ) adjacent to the FZ unless correct procedures are followed. However, with the use of appropriate materials and procedures, nodular cast iron castings can be successfully joined to other ductile iron castings and to steel by fusion welding.

3.2.1. Arc Welding

Several methods have been employed successfully to arc-weld nodular cast iron to itself and other materials with acceptable properties in both the weld and base metal. The properties of shielded metal arc welded nodular cast irons were greatly improved by the introduction over 30 years ago of the high-Ni and Ni-Fe electrodes (AWS Ni-C1 and ENi-Fe-C1). These electrodes produce high-nickel fusion zones that are relatively soft and machinable but have adequate tensile strength, ductility and fatigue strength. The short arc, or dip transfer MIG welding process, by virtue of its controlled, low heat input, reduced harmful structural changes in the base metal HAZ. Combining the benefits of Ni-base filler wire with the short-arc MIG process has resulted in welds with tensile properties that are equivalent to the base nodular cast iron (Table 3.1) and fatigue strengths that are 65% and 75% respectively of the fatigue limits of unwelded pearlitic and ferritic ductile irons (Figures 3.3 and 3.4). Although suffering from the disadvantages of high consumable costs, low deposit rate (1.8-3.2 kg/h) and a tendency toward lack-of-fusion defects, short-arc MIG welding has been used successfully for the joining of ductile iron castings for

commercial applications. Recent work at BCIRA has shown that short-arc MIG welds made with high Ni filler wire have Charpy fracture energies that are superior to those of MIG-welded joints made with Ni-Fe and Ni-Fe-Mn wires and flux-core arc welded joints produced with Ni-Fe wire (Nishio, K. et al., 1988; Davila, M.A. et al., 1977; Mukae, S. et al., 1990; Matharu, I.S. & Selby, K., 1990).

Table 3.1 Average transverse tensile properties of short-arc mig-welds between 25mm thick plates.

Matrix structure	Filler metal	0.2% offset yield strength, N/mm ²	Tensile strength, N/mm ²	Elongation, % in 50 mm
Ferritic	Unwelded	232-309	386-541	15-25
	Nickel 61		422	11.5
	Monel 60		400	8.7
	Nilo 55		412	12.7
Pearlitic	Unwelded	386-463	618-772	1-3
	Nickel 61	358	550	3.5
	Monel 60	346	495	2.5
	Nilo 55	339	425	5.7

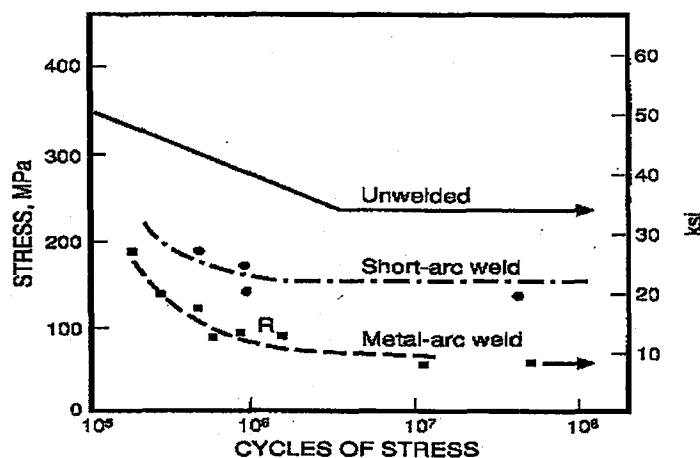


Figure 3.3. Rotating-bending fatigue strength of welded and unwelded ferritic nodular cast iron.

14/1
Karynelli?

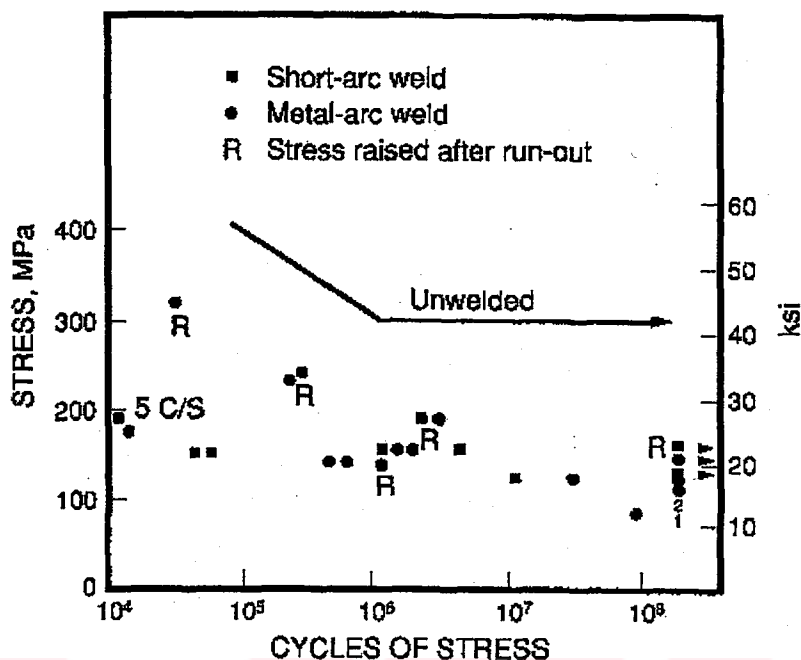


Figure 3.4. Rotating-bending fatigue strength of welded and unwelded pearlitic nodular cast iron.

3.2.2. Flux Cored Arc Welding

Flux cored arc welding (FCAW), utilizing a flux cored wire developed specially for the welding of cast irons, has improved upon the metallurgical advantages provided by the Ni-rich consumables and offers the additional advantage of much higher metal deposit rates (6-9 kg/h). The key to the success of the FCAW process is the consumable, marketed under the trade name "Ni-Rod FC55", which consists of a nickel-iron tubular wire filled with carbon, slagging ingredients, and deoxidizers. In addition to the advantages offered by the high nickel content, Ni-Rod FC55 provides the additional benefits of a high carbon content, which produce graphite precipitates during the solidification of the weld metal. It has been claimed that the expansion resulting from the formation of graphite counteracts weld-metal shrinkage, reducing stress-induced cracking of the weld. The high productivity of the FCAW method, and the good mechanical properties of welded joints (Table 3.2) have resulted in its use in the production of critical, high volume automotive components such as drive shafts, "half-shafts" and wheel spindles on off-road vehicles. This ability to

economically produce high quality welds has given foundries the added freedom to employ cast-weld techniques for the production of complex components.

Table 3.2 Mechanical properties of joints welded with flux-cored wire Ni-Rod FC55: base material ASTM grade 60/45/10 nodular cast iron.

Specimen	Shielding	0.2% offset yield strength, N/mm ²	Tensile strength, N/mm ²	Elongation %	Reduction of area %	Hardness, HRB
All-weld metal	None	310	476	15.5	14.5	81
All-weld metal	CO ₂	314	496	21	18.8	80
All-weld metal	Sub-arc flux	338	510	18.5	20.6	86
Transverse	None	300	455	-	-	-
Transverse	CO ₂	303	455	-	-	-
Transverse	Sub-arc flux	310	441	-	-	-
All-weld-metal*	CO ₂	303	468	15	16.2	80
Transverse*	CO ₂	300	467	-	-	-
*Pulsing-arc power source.						

3.2.3. Joint Design and Preparation

The design of a welded joint is dependent upon factors such as metal thickness, casting geometry, welding process and service requirements. Whenever possible, the design should ensure that the components being joined, rather than the weld, carry most of the load. With a welded assembly the designer can often position the weld in an area of low stress. Figure 3.5 provides examples of joint designs which have been improved to reduce joint stress and increase weld penetration. To ensure sound, gas-free welds, the casting skin adjacent to the joint should be removed and the joint surfaces should be freshly ground or machined and any scale, rust, dirt, grease and oil removed.

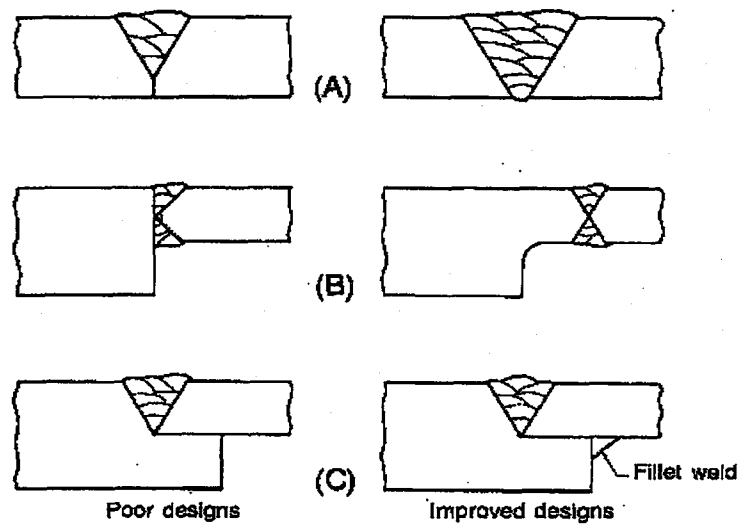


Figure 3.5 Joint design improvements.

3.2.4. Thermal Treatments

When practical, the casting should be preheated in order to prevent thermal cracking, reduce hardness in the HAZ and reduce residual stresses and distortion. It is preferable that the entire casting be preheated but when casting size or the lack of facilities makes this impractical, castings can be preheated with burners or an oxyacetylene torch. When local preheating methods are employed, extreme care is required to avoid rapid, non-uniform heating to avoid cracking and distortion in complex castings. Ferritic nodular cast irons require only a mild preheating in the range 150-200°C. Pearlitic nodular cast iron requires higher preheating temperatures, 315-340°C. Low heat input welding methods such as short-arc MIG minimize the harmful effects of the HAZ. Post-weld thermal treatments such as slow cooling and postheating may be required to reduce residual stresses. Depending upon service requirements, the welded assembly may be subjected to annealing or normalizing heat treatments to dissolve carbides and produce the desired mechanical properties.

CHAPTER FOUR

FRACTURE MECHANICS

4.1 Introduction

It is, apparently, impossible to produce a solid body, regardless of the particular material involved, so perfect in structure that it contains no flaws or microcracks of any kind. The origination of macroflaws can arise from sources such as inclusions, whereas certain models involving the concepts of dislocation theory have been used to explain how microcracks could originate. This indicates one area of study in this complex subject and the main intent is to explain in the most basic sense why and how cracks originate. Another approach to this subject falls under the heading of Linear Elastic Fracture Mechanics (LEFM), where the stress fields around cracks tips of various sizes and shapes are described. It is essentially mathematical in nature and is employed as a design tool in those situations where a traditional strength of materials approach has been found to be lacking in terms of completeness.

4.2 Linear Elastic Fracture Mechanics (LEFM)

In real structures, flaws or cracks can originate for a variety of reasons. Defect due to welding, the effects of stress corrosion or even the presence of microcracks explained by dislocation theory indicate potential sources. The existence of a crack by itself is not of true concern; it is only when service conditions cause the crack to propagate that concern may turn to dismay. Starting with the premise that structures will contain flaws or cracks, it becomes essential to consider their sizes, shape, etc. in initial design considerations; this introduces the key difference between the concept of fracture mechanics and strength of materials.

It is now generally accepted that the primary parameters involved in brittle fracture design are size, shape, and location of the worst crack, the magnitude of applied tensile stresses, and a material property called fracture toughness. Other variables such as temperature and strain rate, although of decided influence, may be viewed as secondary parameters in exactly the same vein which they influence yield strength or other material properties. Certainly much useful information related to transition from ductile to brittle behaviour as a function of temperature has been obtained from this test. However, such numerical test values have not yet found use in a direct analytical manner that would lead to *quantitative* predictions.

Linear Elastic Fracture Mechanics (LEFM) introduces, by analytical means, the equations which describe the magnitude and distribution of stresses around the type of crack as a function of the applied stresses, crack size and shape, and a parameter called the *stress intensity factor*. 49/1

The latter, denoted as K , is considered as a scale factor that accounts for the presence of a crack as it affects the stresses in the vicinity of the crack tip. The importance of K is that it describes the stress field, not simply the largest single stress, and when it reaches a critical value, K_c , is imminent.

Traditionally, three possible loading modes have been considered in regard to crack opening. They are called Mode I, II and III as shown in Figure 4.1 and the stress intensity factors for these modes are denoted as K_I , K_{II} , and K_{III} .

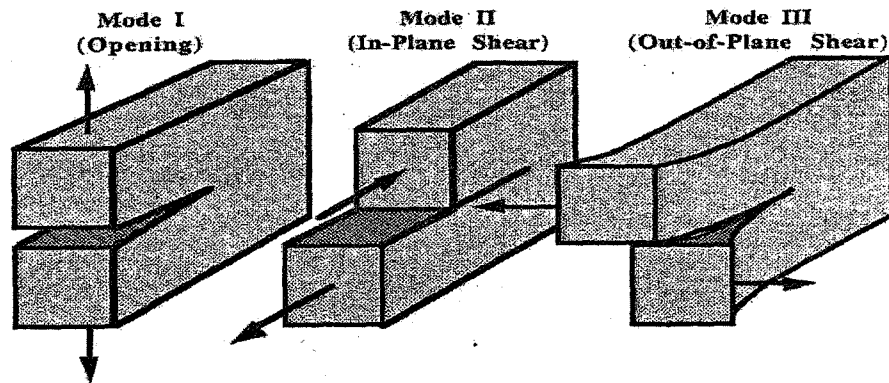


Figure 4.1 Three modes of loading used in linear elastic fracture mechanics analyses.

The critical parameter of concern is written as K_{Ic} and will receive our major attention. The equations that describe the stress field for Mode I loading come from a method attributed to Westergaard and are as follows:

$$\begin{aligned}\sigma_y &= \frac{K_I}{(2\pi r)^{1/2}} \cos \frac{\theta}{2} \left[1 + \sin \frac{\theta}{2} \sin \frac{3\theta}{2} \right] \\ \sigma_x &= \frac{K_I}{(2\pi r)^{1/2}} \cos \frac{\theta}{2} \left[1 - \sin \frac{\theta}{2} \sin \frac{3\theta}{2} \right]\end{aligned}\tag{4.1}$$

$$\tau_{xy} = \frac{K_I}{(2\pi r)^{1/2}} \sin \frac{\theta}{2} \cos \frac{\theta}{2} \cos \frac{3\theta}{2}$$

$$\sigma_z = \nu(\sigma_x + \sigma_y), \quad \tau_{xy} = \tau_{yz} = 0$$

where Figure 4.2 defines the notations of the coordinate system used.

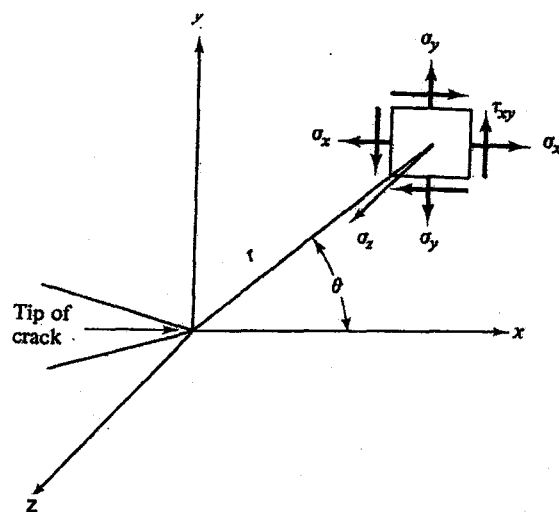


Figure 4.2 Stress state in the vicinity of a crack tip showing coordinates.

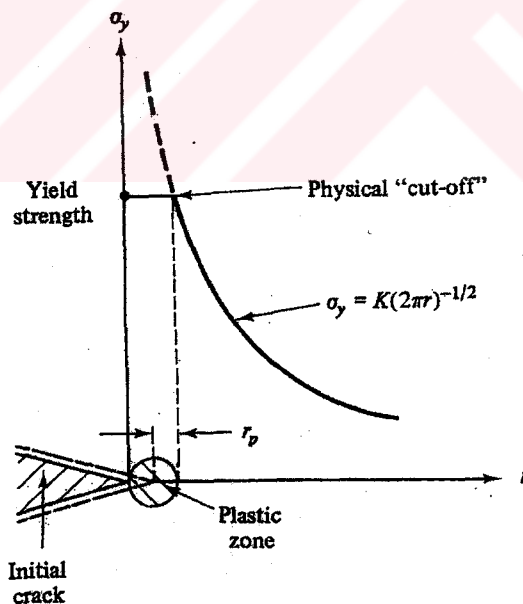


Figure 4.3 Formation of plastic zone at a crack tip when yielding occurs.

The case of plane strain will receive major attention and Eq.(4.1) expresses that physical situation where higher order terms in r have been omitted. As r approaches the edge of the crack, these equations provide good predictions of the stresses in that

region. Of course it is obvious that these predictions indicate the possibility of extremely high stresses in the vicinity of the crack and could not be expected in a real material. The limit to any actual stress magnitude would be the yield strength of the solid. That is, regardless of what values would be *predicted* by Eq. (4.1), the maximum value would *cut off* when yielding occurred.

Figure 4.3 illustrates this physical situation for σ_y at $\theta = 0$. As may be seen in Equation (4.2) K_I is related to the applied stress σ_a and the square root of some function of the crack length: , thus in a general form:

$$K_I = C\sigma(a)^{1/2} = f(\sigma, a) \quad (4.2)$$

where C is functional coefficient.

4.3 Elastic Plastic Fracture Mechanics

Linear elastic fracture mechanics breaks down when high toughness materials are used. To have quantitative predictions, elastic-plastic analysis of cracked bodies is necessary. A single parameter characterization of elastic plastic fracture, analogous to LFM, is aimed at.

Fracture analysis in the plastic regime has, however, a number of complications not present in the elastic case. Foremost are the inherent nonlinearities in the material deformation and large geometry changes together with the fact that flaws will propagate in a stable manner prior to final fracture. Hence, a plastic fracture methodology must explicitly treat crack initiation and the subsequent stable crack growth to the onset of the ultimate unstable crack propagation.

Figure 4.4 shows schematically four different regimes that a cracked body can experience depending on the toughness of the material (Soete, W., 1978; Turner, C.E., 1979). For simplicity a two-dimensional centre-crack geometry is considered. The arrows at the ends of the specimen depict the magnitude of the loading (uniform

applied stress, σ). Also a schematic stress distribution in the net section is shown using the following notation:

σ_l = local stress at a very short distance from the crack tip;

σ_n = average net section stress;

σ_y = uniaxial yield stress.

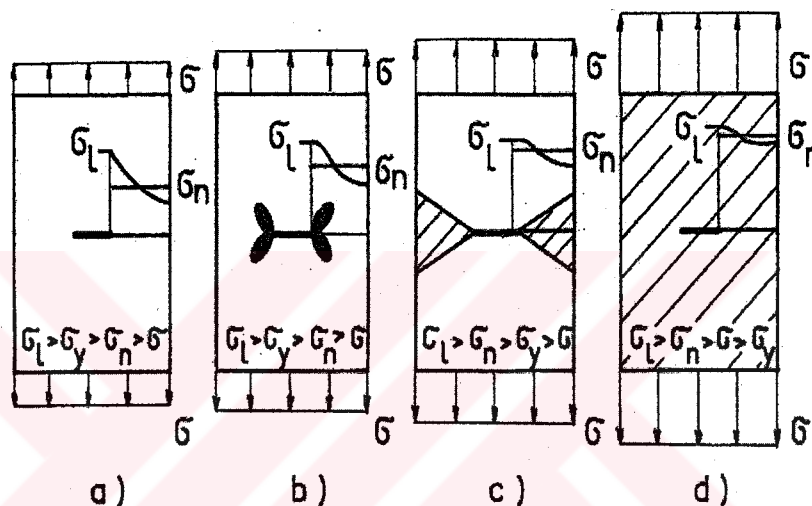


Figure 4.4 Different regimes of a cracked elasto-plastic body. (a) LEFM, (b) EPFM, (c) net section yield, (d) general yield.

The extent of plastic zones is represented by the black or shadowed areas. A brief description of the four regimes is given below.

- (a) Linear Elastic Fracture Mechanics (LEFM) regime. Yielding is limited to a very small zone in the immediate vicinity of the crack tip (small scale yielding). Failure in this regime occurs by brittle fracture, i.e., fast unstable crack propagation.
- (b) Elastic-plastic regime. A yield zone develops ahead of the crack tip but yielding remains contained, i.e., the plastic zone does not reach the lateral boundary of the structure. Failure occurs usually by fast unstable crack propagation.

- (c) Gross yield (or net section yield). Yielding spreads to the lateral boundaries and becomes uncontained. Failure may be fast unstable crack propagation, by plastic collapse of the net section, or by stable tearing followed by tearing instability.
- (d) General yield. The applied stress is larger than the yield stress: the whole structure is plasticized. Plastic collapse and tearing instability are the dominant failure modes.

It is to be noted that components likely to reach gross or general yield checked against plastic collapse by an appropriate design procedure.

4.3.1 Formulation of J-Integral

In linear elastic fracture mechanics (LEFM), the value of J_{IC} can be obtained from the value of K_{IC} by using the following formula:

$$K_{IC} = \sqrt{\frac{J_{IC} \cdot E}{1 - \nu^2}} \quad (4.3)$$

The J-Integral proposed by Rice (1968) forms the basis of fracture beyond the linear elastic range. It is an extension of LEFM, relating the crack size to applied stress, in the presence of large scale yielding and an elegant alternative to obtain K_{IC} values from sub size specimens.

The J-integral is defined as a line integral in the two dimensional strain field of a nonlinear elastic material:

$$J = \int_{\Gamma} W dx_2 - n_i \sigma_{ij} \frac{\partial u_i}{\partial x_j} ds, \quad (4.4)$$

where Γ is any contour from the bottom crack surface around the tip to the top surface. In Figure 4.5, n is the outward unit normal to the contour, W is the strain

energy density and defined as $W = \int_0^{\epsilon} \sigma_{ij} d\epsilon_{ij}$, u are the displacements and ds is an

infinitesimal element contour arc length. The integral is path independent when the crack is straight, traction free and any material interface parallel to the crack.

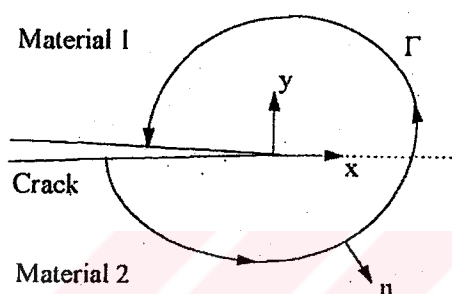


Figure 4.5 Co-ordinates and typical contour used to evaluate the J-integral

J is calculated as potential energy difference between two bodies having identical boundary traction and incrementally different crack lengths. The J integral concept is convenient for numerical evaluation using finite elements, is applicable to nonlinear behaviour and generalizable to account for elasto-plastic material behaviour. For linear elastic behaviour, the J integral is identical to the energy release rate, G .

4.4. Constraint and Triaxiality of Stresses around Crack Tip

The effects of crack tip constraint are well known, qualitatively, but still no reliable definitions exist to quantify these effects. Constraint is a structural feature that inhibits plastic flow and causes a higher triaxiality of stresses. It therefore may promote fracture because the input of external work, for example, measured by J , will to a lesser part be dissipated by plastic deformation but be available to enhance material degradation and damage. However, an engineering application of this concept requires a unique description of the quantities constraint, triaxiality, damage, and so on, allowing the quantitative evaluation of the involved parameters; for

example, by finite element analyses. Although there is no doubt that the resistance against ductile tearing depends on the constraint or triaxiality of stresses, the problem still to be solved is how to define and quantify this parameter in a significant, reliable, and reproducible manner. Different definitions and measures are in use and impede a comparison of various approaches to account for constraint.

Loss of constraint can occur if plasticity extends to a free surface. In the case of a ductile layer (weld metal) between HAZs, additional constraint of the plastic zone may occur when plasticity extends across the weld metal. This constraint also results in higher triaxial stresses ahead of crack tip. The increasing constraint limits the crack tip blunting (Kruzic et al, 2004).

A physically significant definition of the triaxiality of the stress state resulting from crack tip constraint is given by the ratio, h , of the hydrostatic stress, σ_h , or first invariant of the stress tensor, which does not cause any plastic deformation, over the von Mises effective stress, σ_e , (which is the square root of the second invariant of the deviatoric stresses) being responsible for plastic flow (Eq. 4.5).

$$h = \frac{\sigma_h}{\sigma_e} = \frac{\sqrt{2}\sigma_{kk}}{3\sqrt{3}\sqrt{\sigma'_{ij}\sigma'_{ij}}} \quad (i, j, k=1, 2, 3) \quad (4.5)$$

where σ'_{ij} is deviatoric stress. This idea dates back to Hencky's diagram (Hencky, H., 1943) of effective shear stress, $\tau_e = \sigma_e / \sqrt{3}$, versus hydrostatic stress. The physical meaning of this ratio was substantiated by the investigations of McClintock (McClintock, F.A., 1968), Rice and Tracey (Rice, J.R. & Tracey, D.M., 1969), who found that the growth rate of cavities in perfectly plastic materials is proportional to $\exp(3\sigma^\infty / 2\sigma_0)$, where σ^∞ and σ_0 are the remote mean or hydrostatic stress and the yield stress, respectively. For a hardening material the yield stress equals the actual von Mises effective stress, σ_e , under fully plastic conditions.

CHAPTER FIVE

MISMATCHING

As generally known that the different parts of most weldments (Weld metal, base metal, and HAZ) exhibit significantly different strength levels and this weld is called as strength mismatch. Exhibiting the different yield strength levels of the different main parts of welded joint such as base metal (BM), weld metal (WM) and Heat-Affected Zone (HAZ) is called mismatch. The results of various studies on this subject show that; strength mismatch can significantly affect structural performance, deformation and fracture behaviour of the welded joints (Fu, J.Q. & Shi Y.W., 1996).

If the weld metal is considered as a potential location for defects or cracks to be present or develop, the higher yield strength of the weld metal (defective region) compared to the base metal may in fact provide an optimum weld joint performance by shielding a crack from imposed strains. However, nominally identical applied stress/strain levels cause different amounts of strain concentrations at the respective parts of the weld joints. The structural integrity of the cracked mismatched weld joint therefore mainly depends on the fracture toughness of the cracked zone and complex stress/strain condition of the crack tip due to the heterogeneous interface at the finite vicinity of the crack tip. The strength levels of the neighbouring zones will certainly influence the failure behaviour of the structure associated with this crack. In other words, the straining capacity of a weldment not only depends on local toughness, but equally on the difference between the weld metal, base metal and HAZ (Heat-Affected Zone) yield strengths, weld size, the yield to tensile ratio and defect size (Kocak, M. et.al., 1989; Tang, W. & Shi, Y.W., 1995).

M, the mismatch factor, is identified as the ratio of the yield strength of the weld metal to the yield strength of the base metal. If the ratio is higher than one, the weld is called, over-matched; if the ratio is lower than one, it is under-matched (Fu, J.Q. & Shi Y.W, 1996).

$$M = \frac{\sigma_y^{WM}}{\sigma_y^{BM}} \quad (5.1)$$

Thus, σ_y^{WM} is the yield strength of the weld metal and σ_y^{BM} is the yield strength of the base metal. It is still difficult to define the optimum combination of weld metal strength and toughness for a given defect size, location and application, since toughness decreases with increasing yield strength. It is now known that a complete fracture characterization of mismatched weld joints should not only be based on the mismatch factor (M). This will lead to an oversimplification, since the effect of work hardening of weld and base metals is found to be even more important. Therefore, careful consideration should be given to various parameters such as; mismatch factor (M), strain hardening exponents of the base metal (n_b) and weld metal (n_w) as well as to the applied stress/strain range, weld metal width (2H) and relative crack size, $2H/(W-a)$ for the fracture behaviour analysis of under-matched and over-matched weld joints.

The effect of the relative difference (mismatching) of the yield strengths of the base metal, weld metal and HAZ parts on defect assessment procedures and on toughness values (Crack Tip Opening Displacement, CTOD and J-integral) of the material displaying a defect must be determined. Present defect assessment procedures are based on homogeneous materials and generally assume that defects occur in material of uniform mechanical and microstructural properties. In reality through the mechanical heterogeneity of welded joints have an effect on structural behaviour. This effect, however, is not considered in these procedures. Therefore, there is still a need to establish a relationship between applied strain, toughness and defect size for mismatched welds.

CHAPTER SIX

FINITE ELEMENT METHOD

6.1 Introduction

In the finite element method, the body is replaced by a system of finite elements and the nodes connecting them. The next step in this method of analysis is to determine the "element stiffness matrix" of the individual elements representing the body. These will then be assembled to form the "overall stiffness matrix" for the entire "discretized" body by requiring that the continuity of displacements and equilibrium of forces prevail at all nodes in the finite element model of the body. This will lead to the matrix equation

$$[K] \cdot \{\delta\} = \{P\} \quad (6.1)$$

in which $[K]$ denotes the overall stiffness matrix of the body. The overall force vector $\{P\}$ lists the externally applied forces at all the nodes, while $\{\delta\}$ lists the displacements of all nodes.

To summarize the finite solution of a given problem the execution of the following operations is required in this order:

1. "Discretization" (subdivision) of the body into a system of finite elements.
2. Derivation of the element stiffness matrix and other properties for each individual element representing the body.
3. Assembly of the "overall stiffness matrix" $[K]$ and the "overall force vector" $\{P\}$.

4. Solution of Equation (6.1) with prescribed boundary conditions to determine $\{\delta\}$, and
5. Calculations of stresses and strains within the elements from the computed nodal displacements, $\{\delta\}$.

6.2 Interpolation Concepts In Three Dimension

In the finite element literature, the function used to represent the behavior of a field variable within an element are called interpolation functions, shape functions or approximating functions. One type of useful interpolation function is the Lagrange polynomial. Interpolation functions for this family of elements may be written as the product of the Lagrange polynomials in all of orthogonal coordinate directions r, s, t (origin at the centroid of the element). Hence for each node k , interpolation functions can be written as.

$$N_k(r, s, t) = L_k(r)L_k(s)L_k(t) \quad (6.2)$$

where each function L_k is properly formed to account for the number of subdivisions (nodes) in the particular coordinate directions.

6.3 Strain - Displacement Transformation Matrix

$\partial u / \partial x, \partial u / \partial y, \partial u / \partial z, \dots, \partial w / \partial z$ can be evaluated, therefore, the strain displacement transformation matrix B can be constructed in the following equation

$$\{\varepsilon\} = [B]\{\delta\} \quad (6.3)$$

where $\{\delta\}$ is a vector listing the element nodal point displacement, that is

$$\{\delta\}^T = \{u_1 \ v_1 \ w_1 \ \dots \ u_8 \ v_8 \ w_8\} \quad (6.4)$$

B,

$$[B(x,y,z)] = \begin{bmatrix} \frac{\partial N_1}{\partial x} & \frac{\partial N_2}{\partial x} & \dots & \frac{\partial N_8}{\partial x} \\ \frac{\partial N_1}{\partial y} & \frac{\partial N_2}{\partial y} & \dots & \frac{\partial N_8}{\partial y} \\ \frac{\partial N_1}{\partial z} & \frac{\partial N_2}{\partial z} & \dots & \frac{\partial N_8}{\partial z} \end{bmatrix} \quad (6.5)$$

And also ε is a strain vector and can be expressed in the following form;

$$\{\varepsilon\} = \left\{ \frac{\partial u}{\partial x}, \frac{\partial v}{\partial y}, \frac{\partial w}{\partial z}, \left(\frac{\partial u}{\partial y} + \frac{\partial v}{\partial x} \right), \left(\frac{\partial v}{\partial z} + \frac{\partial w}{\partial y} \right), \left(\frac{\partial u}{\partial z} + \frac{\partial w}{\partial x} \right) \right\}^T \quad (6.6)$$

or

$$[\varepsilon] = \begin{bmatrix} \varepsilon_x \\ \varepsilon_y \\ \varepsilon_z \\ \gamma_{xy} \\ \gamma_{yz} \\ \gamma_{xz} \end{bmatrix} \quad (6.7)$$

6.4 Evaluation of Stresses

In contrast to Young's modulus E in the one dimensional case, elasticity matrix D is used to in the three dimensional version of Hooke's law. The expression giving the stresses at each node is as below :

$$[\sigma] = [D][\varepsilon] \quad (6.8)$$

Where $\{\sigma\}$ is the stress vector and its elements are given in the following form:

$$\sigma = \begin{bmatrix} \sigma_x \\ \sigma_y \\ \sigma_z \\ \tau_{xy} \\ \tau_{yz} \\ \tau_{xz} \end{bmatrix} \quad (6.9)$$

The matrix D as 6 x 6 components assign in Equation 6.10 and contains in the isotropic body only two independent constants which are Young's modulus E , and Poisson's ratio ν . The matrix D can be written as below :

$$D = \frac{E}{(1+\nu)(1-2\nu)} \begin{bmatrix} 1-\nu & \nu & \nu & 0 & 0 & 0 \\ \nu & 1-\nu & \nu & 0 & 0 & 0 \\ \nu & \nu & 1-\nu & 0 & 0 & 0 \\ 0 & 0 & 0 & 0.5-\nu & 0 & 0 \\ 0 & 0 & 0 & 0 & 0.5-\nu & 0 \\ 0 & 0 & 0 & 0 & 0 & 0.5-\nu \end{bmatrix} \quad (6.10)$$

6.5 Material Nonlinearity in ANSYS Software

Structural nonlinearities are due to the nonlinear relationship between stress and strain, that is, the stress is a nonlinear function of the strain. The relationship is also path dependent (except for the case of nonlinear elasticity and hyperelasticity), so that the stress depends on the strain history as well as the strain itself. The program can account for rate-independent plasticity characterized by the irreversible instantaneous straining that occurs in a material.

6.5.1 Rate – Independent Plasticity

Rate - independent plasticity is characterized by the irreversible straining that occurs in a material once a certain level of stress is reached. The plastic strains are assumed to develop instantaneously, that is, independent of time. The ANSYS program provides Multilinear Isotropic Hardening option to characterize material

behavior. Plasticity theory provides a mathematical relationship that characterizes the elasto – plastic response of materials. There are three ingredients in the rate – independent plasticity theory: the yield criterion, flow rule and the hardening rule.

6.5.1.1 Yield Criterion

The yield criterion determines the stress level at which yielding is initiated. For multi-component stresses, this is represented as a function of the individual components, $f(\{\sigma\})$, which can be interpreted as an equivalent stress σ_e . When the equivalent stress is equal to a material yield stress σ_y ,

$$f(\{\sigma\}) = \sigma_y \quad (6.11)$$

where:

$$\{\sigma\} = \text{stress vector}$$

6.5.1.2 Flow Rule

The flow determines the direction of plastic straining and is given as:

$$\{d\varepsilon^{pl}\} = \lambda \left\{ \frac{\partial Q}{\partial \sigma} \right\} \quad (6.12)$$

where:

λ = plastic multiplier (which determines the amount of plastic straining)

Q = function of stress termed the plastic potential (which determines the direction of plastic straining)

If the stress exceeds the material yield, the plastic multiplier λ is determined by a local Newton – Raphson iteration procedure.

6.5.1.3 Hardening Rule

The hardening rule describes the changing of the yield surface with progressive yielding, so that the conditions (i.e. stress states) for subsequent yielding can be established. Work (isotropic) hardening rule is available. The yield surface remains centered about its initial centerline and expands in size as the plastic strains develop.

6.5.2 Plastic Strain Increment

The hardening rule states that the yield criterion changes with work hardening. Incorporating these dependencies into Equation 6.11, and recasting it into the following form:

$$F(\{\sigma\}, \kappa, \{\alpha\}) = 0 \quad (6.13)$$

where:

κ = plastic work

α = translation of yield surface

κ and $\{\alpha\}$ are termed internal or state variables.

6.5.3 Specialization for Hardening

These options use the von Mises yield criterion with the associated flow rule and isotropic (work) hardening. The equivalent stress is:

$$\sigma_e = \left[\frac{3}{2} \{s\}^T [M] \{s\} \right]^{\frac{1}{2}} \quad (6.14)$$

where:

$$[M] = \begin{bmatrix} 1 & 0 & 0 & 0 & 0 & 0 \\ 0 & 1 & 0 & 0 & 0 & 0 \\ 0 & 0 & 1 & 0 & 0 & 0 \\ 0 & 0 & 0 & 2 & 0 & 0 \\ 0 & 0 & 0 & 0 & 2 & 0 \\ 0 & 0 & 0 & 0 & 0 & 2 \end{bmatrix}$$

and $\{s\}$ is the deviatoric stress (Equation 6.15).

$$\{s\} = \{\sigma\} - \{\sigma_m\} [1 \ 1 \ 1 \ 0 \ 0 \ 0]^T \quad (6.15)$$

$$\sigma_m = \text{mean or hydrostatic stress} = \frac{1}{3} \sigma_x + \sigma_y + \sigma_z$$

When σ_e is equal to the current yield stress σ_k the material is assumed to yield. The yield criterion is:

$$F = \left[\frac{3}{2} \{s\}^T [M] \{s\} \right]^{\frac{1}{2}} - \sigma_k = 0 \quad (6.16)$$

For the case of isotropic plasticity assumed here, σ_k can be determined directly from the equivalent plastic strain ($\hat{\epsilon}^{pl}$) of the stress – strain curve (Figure 6.1). σ_k is output as the equivalent stress parameter.

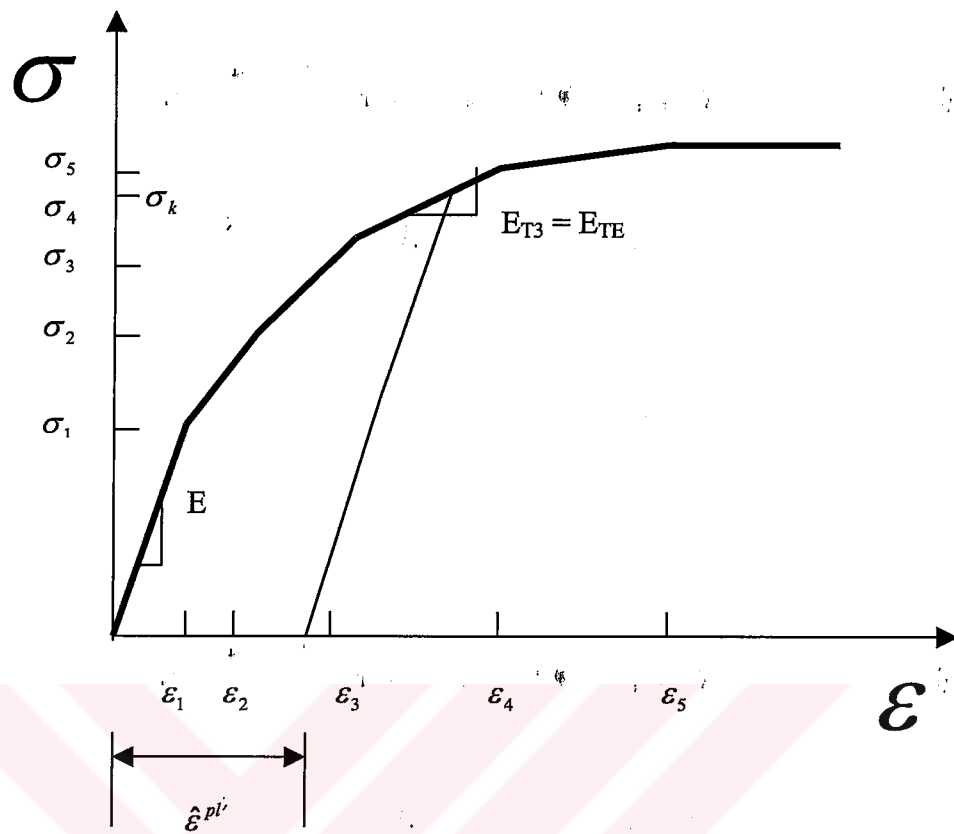


Figure 6.1 Uniaxial behavior for multilinear isotropic hardening and σ_k determination.

CHAPTER SEVEN

EXPERIMENTAL STUDY

7.1 Material

The nodular iron was used as the base material for all welding processes. The chemical composition of the nodular iron is given in the table 7.1, and the table 7.2 shows the mechanical properties of the nodular iron.

Table 7.1. Chemical composition of test material (mass percent).

Element	C	Si	Mn	P	S
Percentage	3.58	2.8	0.08	0.015	0.004

Table 7.2. Mechanical properties of the nodular iron.

$\sigma_{p0.2}$ (MPa)	σ_m (MPa)	E (MPa)	K (MPa)	n	ν	ϵ (%)
367	518	168000	650	0.43	0.31	11

7.2 Specimen Configurations

A standard double V groove was machined to all nodular iron plates having 60 mm length and 12 mm x 50 mm cross section. The configuration of the groove joint is given in Figure 7.1. Prior to welding, these plates were ground to remove the oxide scale and the surface was cleaned with alcohol. Afterwards, the test plates were welded with the cold arc welding method by using the DIN 8573-E Ni BG 22 electrodes in order to obtain under-matched joint. The welding parameters are given in Table 7.3.

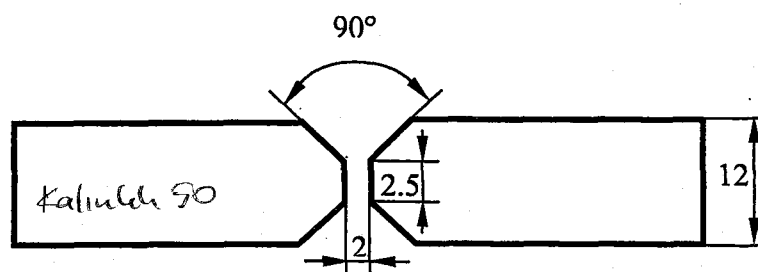


Figure 7.1. Configuration of the groove joint.

Table 7.3. Welding parameters

Welding Process	Cold arc welding
Joint Design	Double V groove
Electrodes	DIN 8573 - E Ni BG 22
Electrode diameter	3.25 mm
Welding Arc current	100 A
Arc voltage	20 V
Number of pass	8

After welding process, nodular iron plates (approximately in 12 mm thickness, 122 mm length and 50 mm width) were obtained.

7.3 Tensile Testing

In order to determine the mechanical properties of the weld metal, two tensile test specimens will be extracted from the double V-groove weld joints. One of these tensile test specimens was taken from the root region and the other one was extracted from the cap region of the weld metal. Tensile test was conducted at room temperature on an Instron model 1114 tester. A crosshead speed of $1 \text{ mm} \cdot \text{min}^{-1}$ was used in the tests. The test specimens were loaded to failure. The stress - strain curves were plotted by a recorder. The 0.2 offset yield strength ($\sigma_{P0.2}$), ultimate tensile stress (σ_m), and elongation were determined from these curves.

σ_{P0.2}

7.4. Micro-Hardness Testing

The test specimens were extracted from welded plates. The micro-hardness values at the weld metal, base metal and HAZ were measured on the root and cap regions along the longitudinal direction of the specimens, as shown in Figure 7.2. The micro-hardness values were measured by Vickers micro-hardness tester with 80 g load.

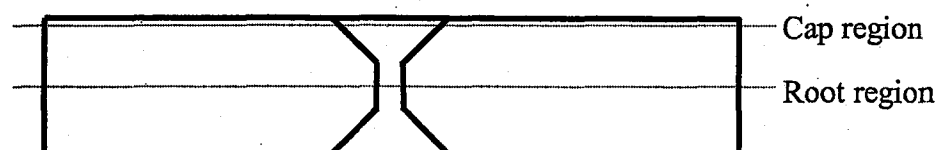


Figure 7.2. Two different locations where the measurements were made.

7.5. Microstructural Examination

Cylindrical shaped specimens of 8 mm diameter and 5 mm height were cut from the weld metal for chemical analysis and microstructural investigations. The specimens were prepared by standard techniques for microstructural and metallurgical examinations. The specimens were grinded by using emery paper and polished by diamond paste. Then, the polished specimens were etched with 2 % Nital solution and were examined using an optical light microscope. In weld region, the variations of the nickel and iron amounts were obtained by scanning electron microscope (JEOL super probe 733) on two different locations (root and cap region) along the longitudinal direction of the specimen, as shown in Figure 7.2.

On the other hand, Electron Back-Scatter Diffraction (EBSD) provides information on the crystal phase and orientation in bulk samples which would normally require transmission electron microscopy of thin foils (Humphreys, F.J. & Brough, I., 1999). Electron Back-Scatter Diffraction maps were obtained using FEG-SEM. The Channel4+ (HKL Technology) software was used to control data collection and analysis. Data was collected at 5 μm intervals over an area of

800x1000 μm . Light etching 2% Nital combined with OPS polishing was used to obtain a suitable surface for good quality channelling patterns.

7.6. J Fracture Toughness Tests

In order to examine the fracture behaviour of the weld metal, base metal and HAZ in weld joint, the preparation of the standard bend specimens for J fracture toughness test was conducted in two steps.

In the first step, the specimens were extracted from welded plates and machined as rectangular bars (10 x 10 x 100 mm) according to the ASTM Standard E 813-89.

After the first step, the single edge-notches were cut at four different locations of the different specimens. The four different locations in the bend specimen are shown in Figure 7.3.

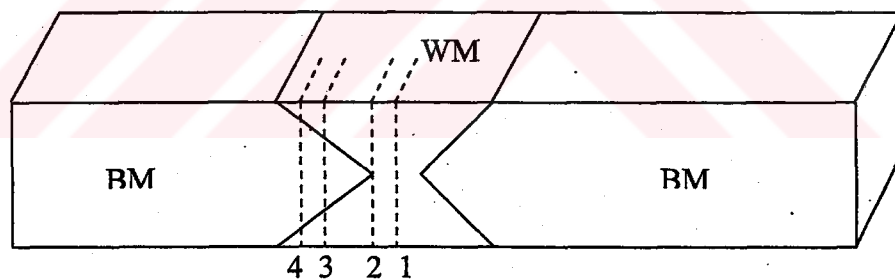


Figure 7.3. The four different crack locations.

Initially; the bend specimens were precracked in fatigue using three-point bend loading until the initial crack length being 0.5 times of the bend specimen width. The principle of the three-point bend test fixture is shown in Figure 7.4.

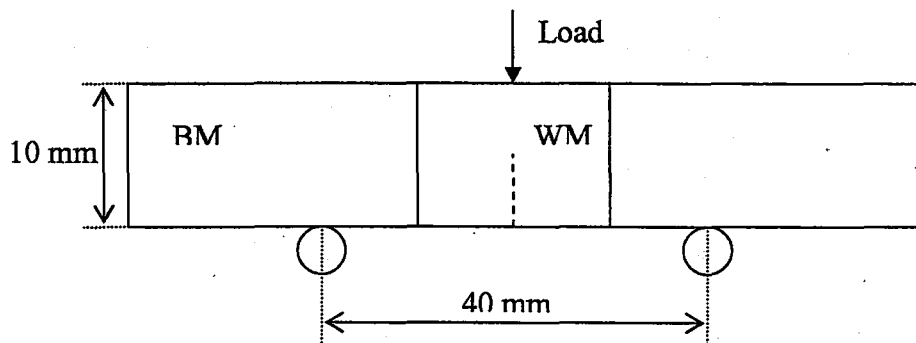


Figure 7.4. Principle of the three-point bend test fixture.

Afterwards, the single specimen technique was used with standard unloading compliance method in order to determine fracture mechanics parameter J .

In the single specimen technique, by using the standard J fracture toughness test fixture, the tests were conducted at room temperature on SHIMADZU AG-50 kNG universal testing machine.

The test technique involves unload/reload sequences steps and in the each step, the specimen was loaded up to a crack mouth opening displacement level reaches 0,05 mm more than previous level. In each step, after a duration of 20 seconds at maximum load point, the applied load was reduced until CMOD level approximately 0,03 mm less than actual level. During the tests, CMOD values were obtained by using a SHIMADZU type SG25-50 displacement gage. By repeating these unload/reload sequences until failure, the load-crack mouth opening displacement (CMOD) curves were recorded by computer.

Sumpter suggested to relate the crack driving force J with the load - CMOD curve for homogeneous single edge notched bending (SENB) specimens (Sumpter, J.D.G., 1987). Based on finite element calculations, Wang and Gordon (Wang, Y.Y. & Gordon, J.R., 1992; Gordon, J.R. & Wang, Y.Y., 1992) proposed the following expression for the inhomogeneous materials:

$$J = J_{el} + \eta_{plCMOD} \frac{U_{Cpl}}{B(W-a)} \quad (7.1.)$$

J_{el} is derived from K values:

$$J_{el} = \frac{(K_i)^2(1-\nu)^2}{E} \quad (7.2)$$

$$K_i = \frac{P_i S}{BW^{3/2}} \cdot f(a_o/W) \quad (7.3)$$

with :

$$f(a_o/W) = \frac{3(a_o/W)^{1/2} [1.99 - (a_o/W)(1-a_o/W)(2.15 - 3.93(a_o/W) + 2.7(a_o/W)^2)]}{2(1+2a_o/W)(1-a_o/W)^{3/2}} \quad (7.4)$$

U_{Cpl} is the area under the load – CMOD curve as defined in Figure 7.5. B is the specimen thickness, W is the specimen width and a_0 initial crack length. Gordon and Wang et al. (Gordon, J.R & Wang, Y.Y., 1992) showed that the J integral can be evaluated from Equation 7.1 with an η_{plCMOD} corrected to include mis-match effect as follow:

$$\eta_{plCMOD} = 3.5 - 1.4167(a_o/W) \left[\frac{\sigma_y^{BM}}{\sigma_y^{WM}} + \frac{1 - (\sigma_y^{BM} / \sigma_y^{WM})}{2} \right] \quad (7.5)$$

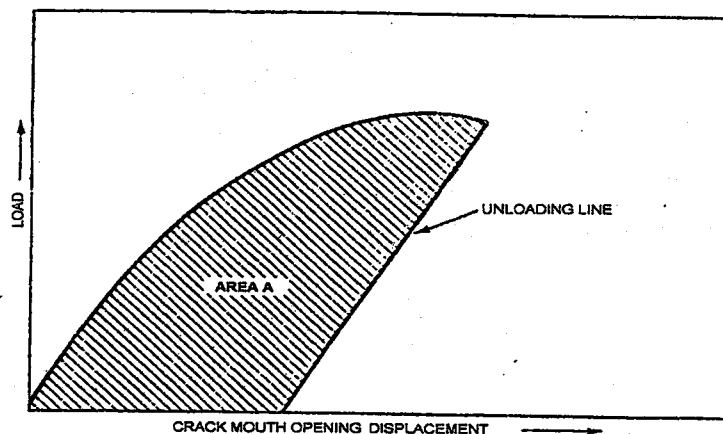


Figure 7.5. Definition of area for J integral.

CHAPTER EIGHT

THEORETICAL STUDY

8.1. FE Model

Three-dimensional finite element (FE) models of three-point bend (3PB) specimens with various regions (BM, WM and HAZ) were fixed by using ANSYS software. Different 3-D models were prepared for various crack locations and crack lengths. Because of symmetry, only half of the thicknesses of the specimens were modeled (Fig. 8.1a). Fig. 8.1b shows the FEM mesh in a global scale. Figure 8.2a depicts the details of the core mesh and the crack tip arrangement. Crack tip and three Heat Affected Zones (HAZs) were more refined. The HAZ thickness is approximately 2 mm. There are 10 singular element rings in the core mesh (Fig. 8.2b). The each 3-D model consists of about 19,621 nodes 20-node 6,076 tetrahedral elements (ANSYS, Solid 95). Fig. 8.1b also shows the paths where stress triaxiality (ST) and equivalent plastic strain (EPS) were determined. Paths were chosen along the longitudinal direction and along the crack front on the models.

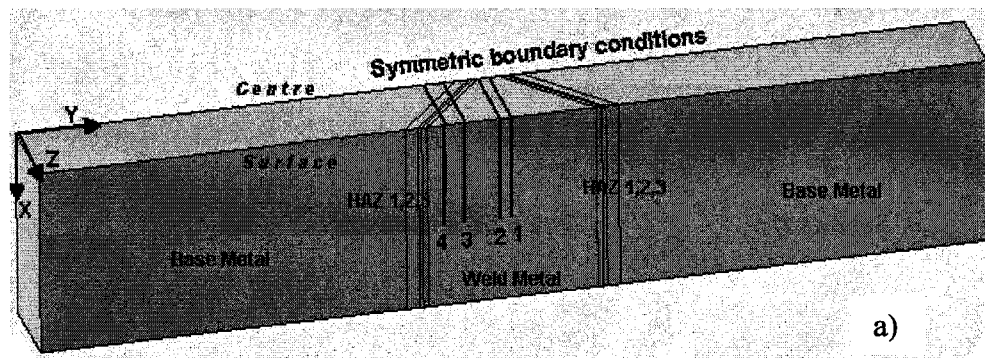


Figure 8.1a Crack locations and half thickness of the specimen with symmetric cross-section.

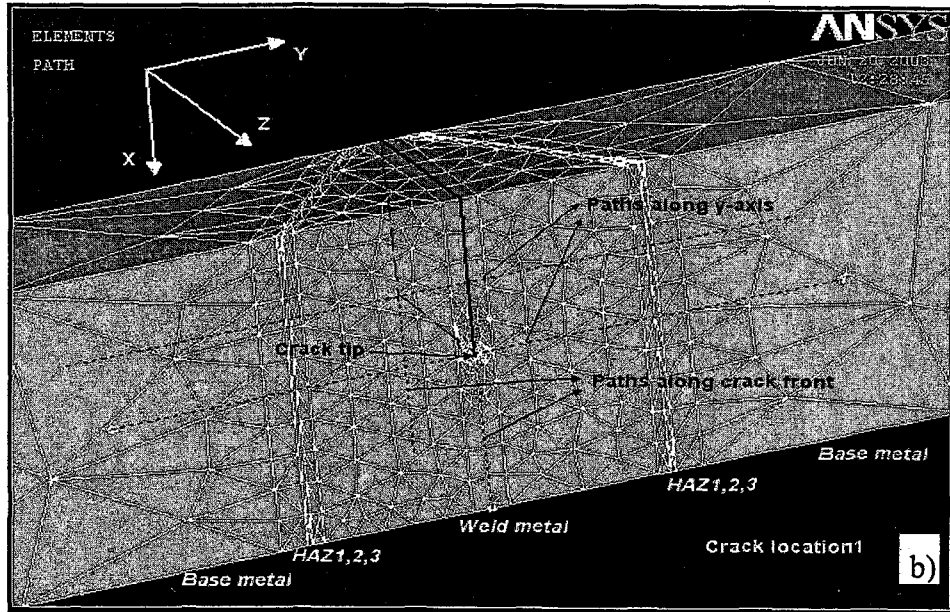


Figure 8.1b FEM mesh in a global scale for the crack location 1.

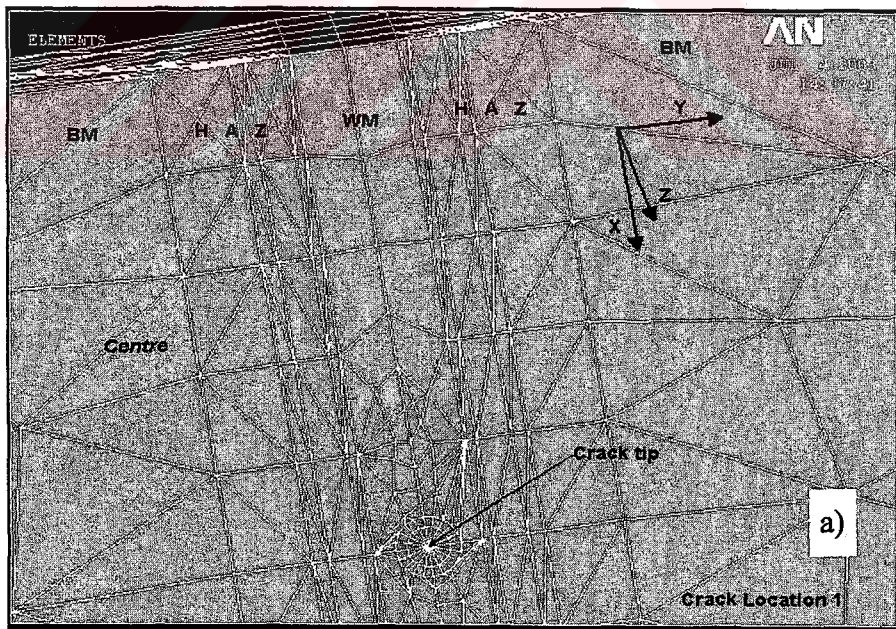


Figure 8.2a Details of mesh core for the crack location 1.

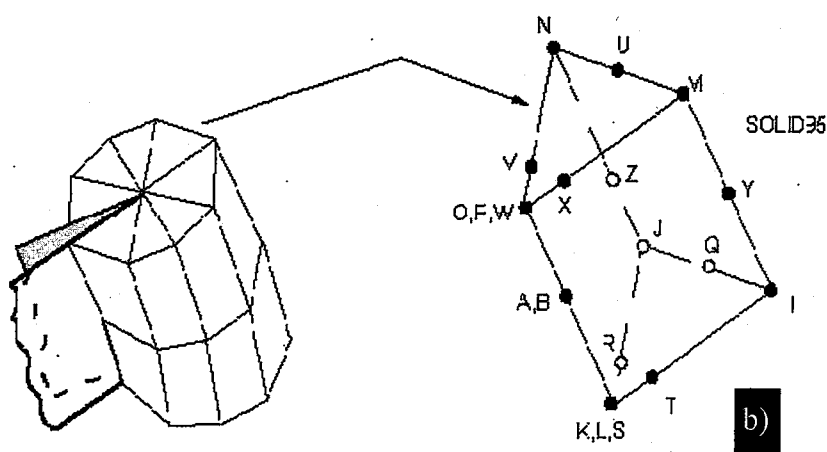


Figure 8.2b singular elements around crack tip.

8.2 Input Data

8.2.1. Linear and Nonlinear Material Properties

True stress - true strain values of WM and BM calculated from tensile test results and modulus of elasticity (E) and poisson ratio (ν) values were entered the program for elastic region and calculated true stress-true strain values starting from yield stress were entered for plastic region instead of Ludwig equation with work hardening exponent. In ANSYS software, true stress-true strain values can be entered step by step so there is no need to calculate work hardening exponent. HAZ was presented as three different regions with different mechanical properties considering micro hardness values (Fig. 9.1). In order to determine yield strength and true stress-true strain values of HAZs, a relationship was investigated between yield stress and micro-hardness values. Thus, quenching and annealing processes were conducted for nodular iron samples. Some nodular iron specimens were heated to 830 °C and was waited 1 hour in the furnace then was quenched in oil. The other ones were heated to 830 °C and were waited for 3 hours at this temperature then were left in the furnace for cooling. Micro-hardness values of quenched and annealed specimens were measured from these specimens then both specimens were prepared for standard tensile testing. Their yield strength values were obtained from tensile tests. Figure

8.3 depicts the average yield strength value vs. Vickers micro-hardness values. A linear line was drawn in order to find yield strength values of HAZ region by using their Vickers micro-hardness values determined from Fig. 8.4.

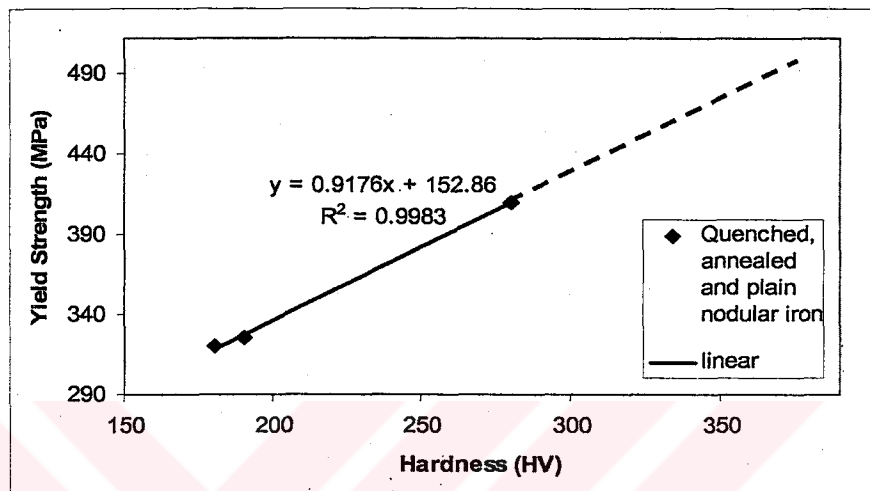


Figure 8.3. Yield strength - micro-hardness relationship

By using stress-micro-hardness relationship of plain, annealed and quenched materials an equation was determined as follows:

$$\sigma_y = 0.92 HV + 153 \quad (8.1)$$

where, HV is Vickers micro-hardness value (HV) and σ_y is yield strength (MPa). HAZ was expressed as three different regions paying attention micro-hardness values.

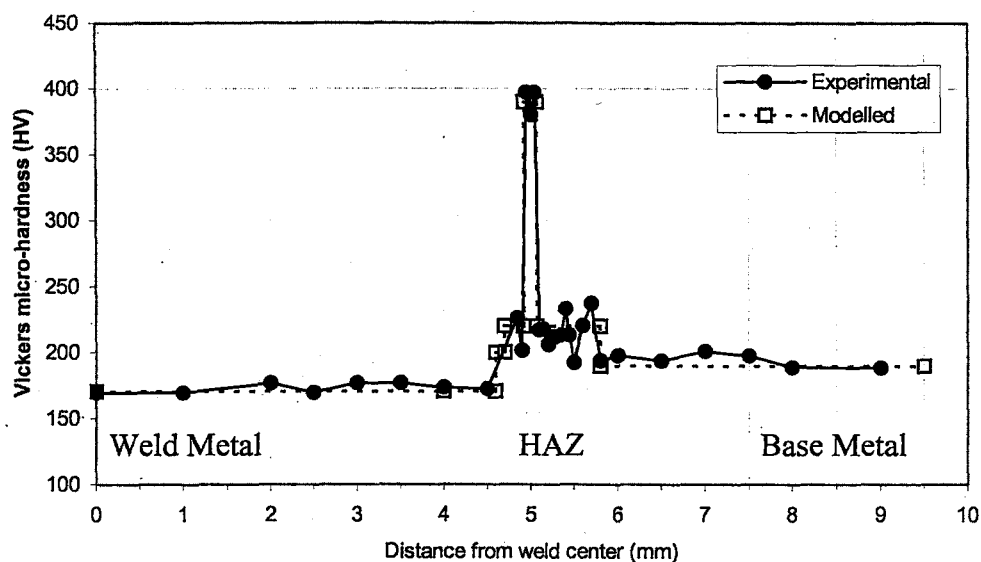


Figure 8.4. Vickers micro-hardness values in different regions.

Table 8.1. shows the micro-hardness values and entered data of WM, BM and HAZ for elastic region. The ratio of the yield strength of the weld metal to the yield strength of the base metal, namely the mismatch factor, is 0.67.

Table 8.1. Micro-hardness values and entered data of WM, BM and HAZ.

	WM	BM	HAZ1	HAZ2	HAZ3
Hardness (HV)	170	190	220	390	210
σ_y (MPa)	218	325	355	512	347
E (MPa)	218,000	168,000	168,000	168,000	168,000
ν	0.31	0.31	0.31	0.31	0.31

In order to enter true stress-true strain curves of plastic region of the three HAZ locations, curves starting from yield strengths of HAZ regions were drawn parallel to quenched material's curve. There is a rapid cooling in the HAZs, so the same work hardening rates were accepted for these regions like quenched material.

Figure 8.5. shows the true stress-true strain curves including weld material as a combination of experimental and calculated results.

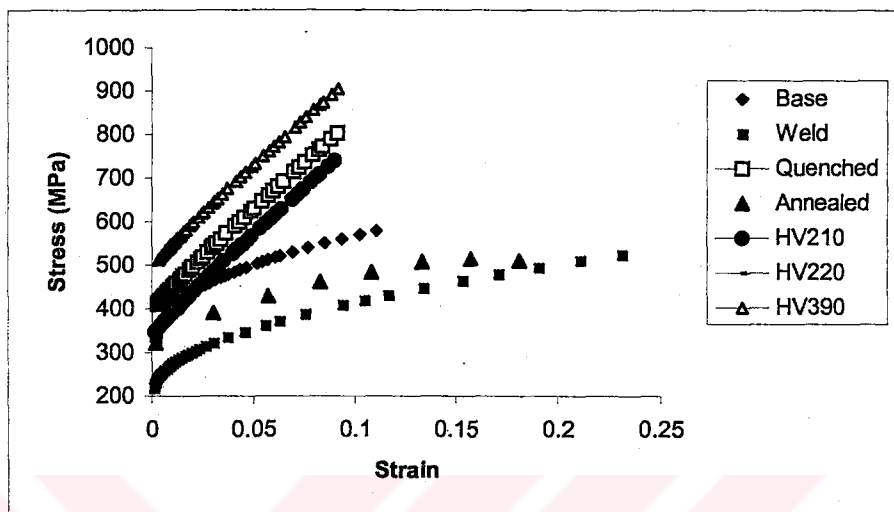


Figure 8.5. True stress-true strain values of the different regions.

8.2.2 Loads

Cheung and Luxmoore (Cheung, S. & Luxmoore, A.R., 2002) performed computations proceeded by dividing the debond process into several trials. They selected crack extensions in order to match load vs. CMOD curves of the numerical and experimental results.

For numerical analysis, certain crack lengths (5, 5.05, 5.1, 5.2, 5.6 and 5.85 mm) were chosen from considering and Load vs. crack propagation and J resistance vs. crack propagation curves (Figures 9.15, 9.16, 9.17, 9.18 and 9.19) for each crack locations. Crack Mouth Opening Displacement (CMOD) values for these chosen crack lengths were determined from load-CMOD curves by using load values in certain crack lengths (Figures 9.11, 9.12, 9.13 and 9.14). In FE analyses, a trial and error method was used to obtain the same CMOD values with experimental ones for the each crack lengths. The free variables were load and crack lengths. The load values were changed for different crack lengths mentioned above until obtaining the

values were changed for different crack lengths mentioned above until obtaining the same CMOD values of experimental ones (Figure 8.6). Stress triaxiality (ST) and equivalent plastic strain (EPS) values were determined after obtaining the same CMOD values from experimental results.

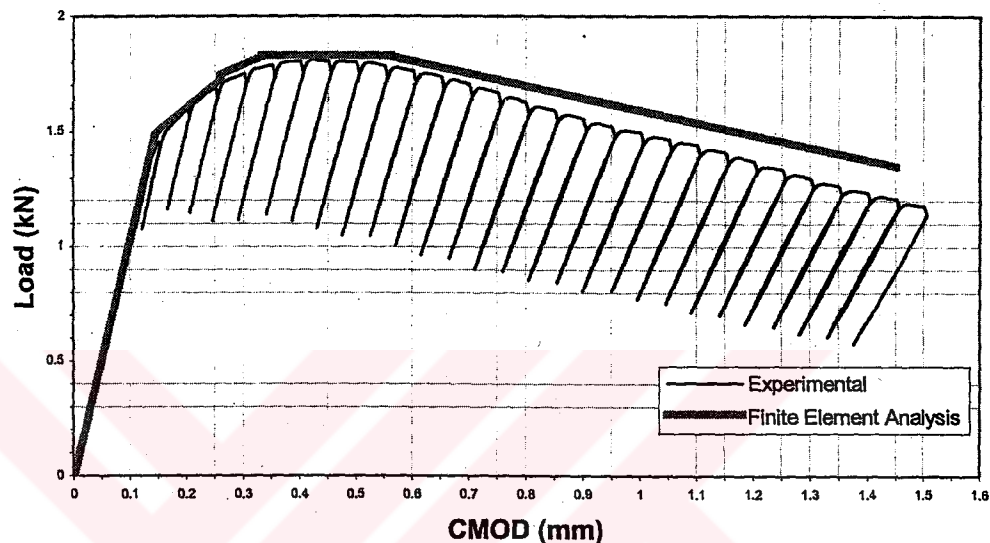


Figure 8.6. Load vs. crack mouth opening displacement curves obtained from FE analyses and experimental results for crack location 1.

8.2.3 Annealed Models

Annealing treatment was considered to decrease yield strength dissimilarities of the base metal, HAZ and the weld metal. The aim is to increase toughness of the HAZ by decreasing its strength. In order to determine the effect of annealing on the stress triaxiality and equivalent plastic strain of welded specimens, true – stress strain values were determined to enter the software. Welded specimens were heated to 600 °C and hold for 3 hours at this temperature then left in the furnace for slow cooling. Microhardness values were obtained along the longitudinal direction of the specimens (Figure 7.2). By using determined microhardness values yield strength values of different regions of annealed specimens were calculated from Equation 8.1. (Table 8.2.).

Table 8.2. Microhardness and calculated yield strengths of different regions on the annealed model.

	Weld Metal	Base Metal	HAZ1	HAZ2	HAZ3
Microhardness (80g) (HV)	81	120	130	220	130
Yield Strength (MPa)	104	263	273	355	273

Plastic parts of true stress – strain curves of different regions on the annealed model were determined by using the same method, which was used to obtain true stress – strain curves of the under-matched models. Figure 8.7. depicts the true stress – strain curves of weld metal, base metal and HAZs of the annealed models. The same modulus of elasticity and Poisson's ratio values were entered the program with the undermatched models.

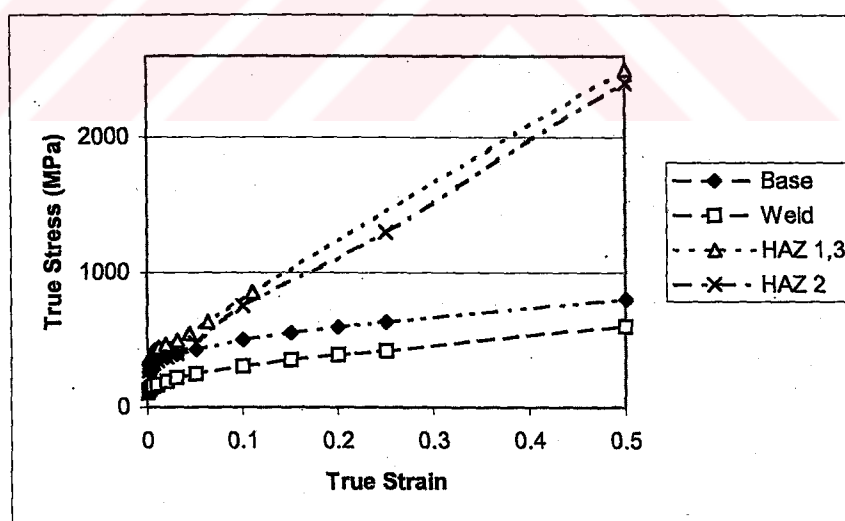


Figure 8.7. True stress – strain curves of different regions on the annealed models.

In FE analyses, applied loads were determined by the same trial and error method used in the calculation of under-matched models. Loads were changed until reaching the same CMOD values of experimental and undermatched models.

CHAPTER NINE

RESULTS AND DISCUSSION IN TERMS OF

EXPERIMENTAL STUDY

9.1. Tensile Properties

The values of 0.2 offset yield strength ($\sigma_{0.2}$), ultimate tensile stress (σ_m), and elongation of the root and cap region of the weld metal were obtained with tensile tests. The mechanical properties of the root and cap region of the weld metal are given in Table 9.1.

Table 9.1. Mechanical properties of the weld metal.

Location	$\sigma_{0.2}$ (MPa)	σ_m (MPa)	ϵ (%)
Root region	247	419	15
Cap region	218	393	22

9.2. Micro-Hardness Values

The hardness values of the weld metal, base metal and HAZ were obtained on two different locations (root and cap region) along the longitudinal direction of the specimen. The hardness values of the weld metal, base metal and HAZ on the root and cap regions are shown in Figures 9.1a and 9.1b respectively.

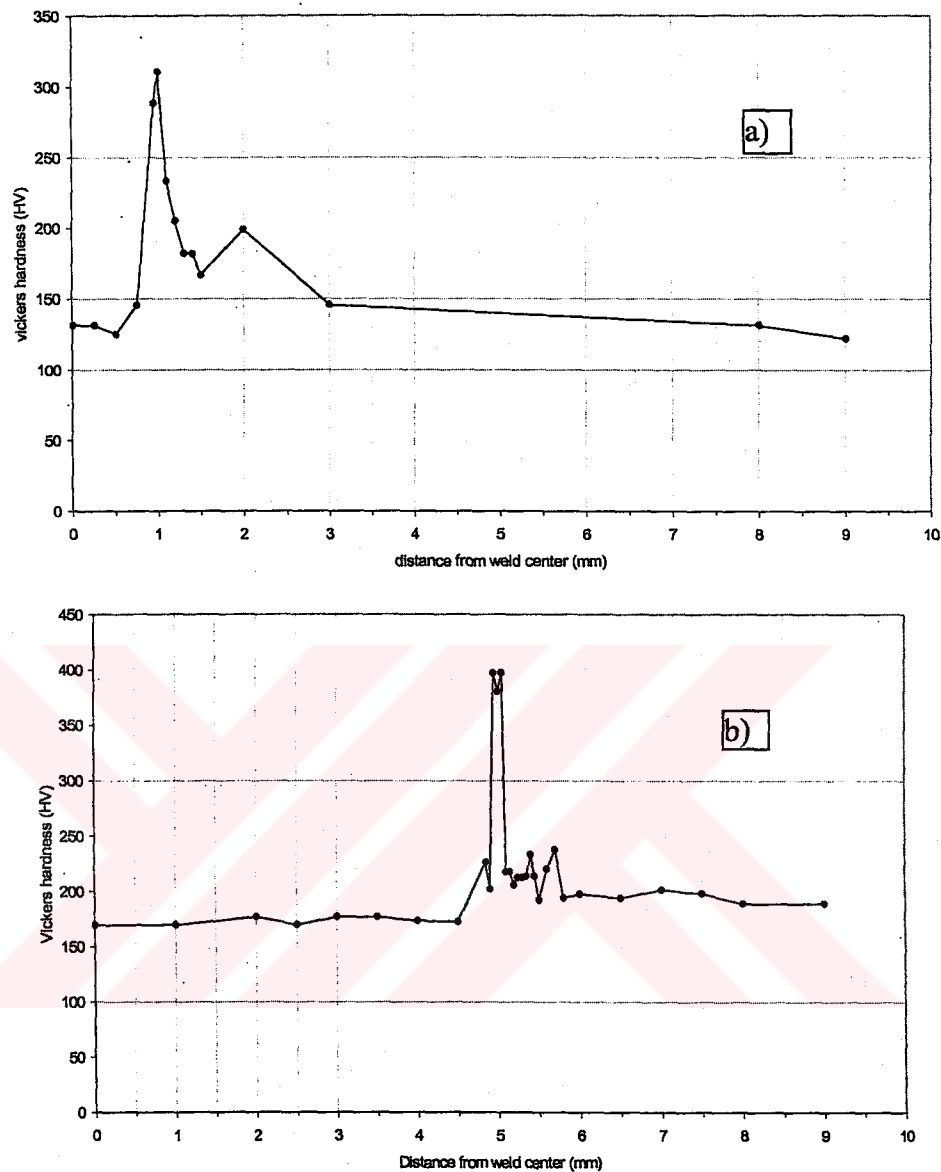
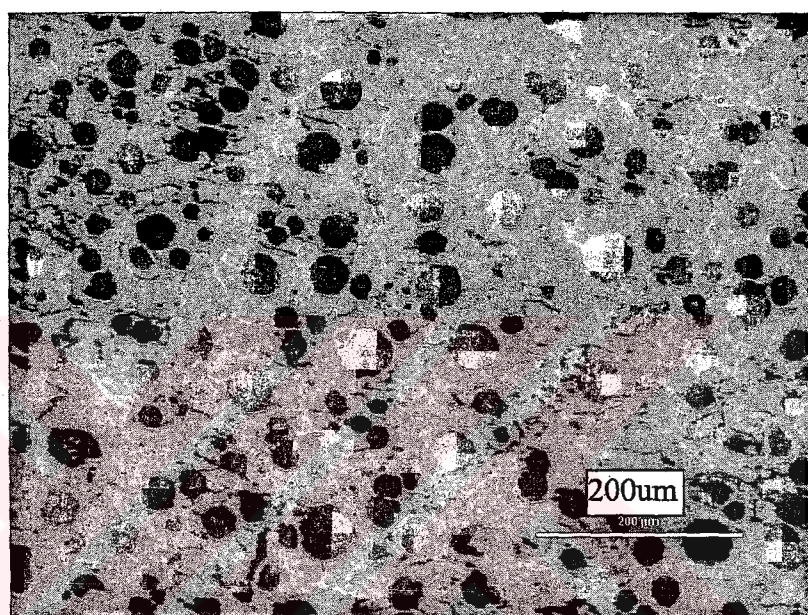


Figure 9.1. The hardness values (a) on the root and (b) on the cap regions.

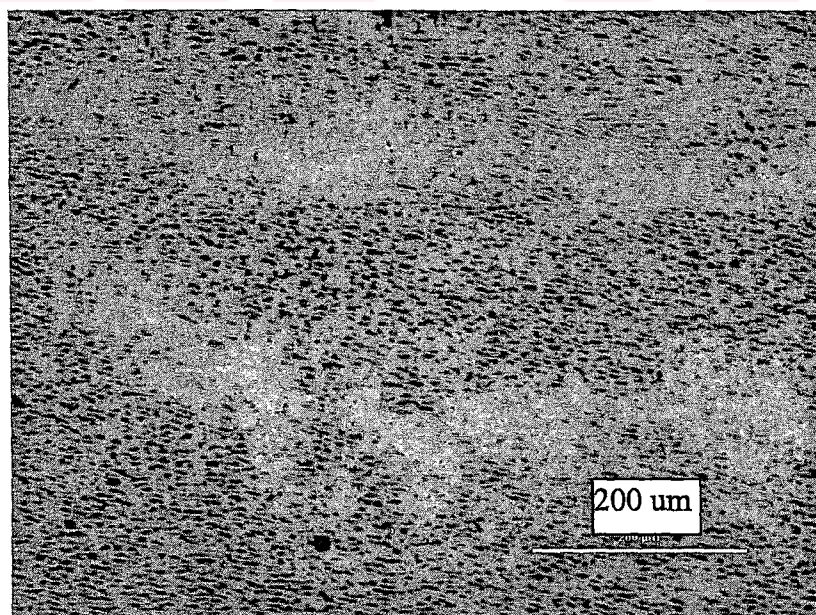
9.3. Microstructures

As seen Figures 9.2a and 9.2b, the mean graphite diameters in weld and base metal were determined as $8 \mu\text{m}$ and $48 \mu\text{m}$, respectively by using LUCIA 4.21 software in image analyser. In deformation process, distribution and size of graphites play important roles. Cast irons behave essentially as porous materials, graphite nodules being considered as voids in an elastic-plastic matrix. On the other hand, Marrow and Çetinel showed that short fatigue cracks initiate graphite-matrix

interface in austempered ductile iron (Marrow, T.J. & Çetinel, H., 2000). Additionally, Hafiz indicated that the overall fracture path is controlled by initial nodule decohesion and microcracking at the graphite/matrix interface. The graphite nodule distribution dictates the least energy propagation path and requires the growing crack to travel through the ferrite phase (Hafiz, M., 2001).



(a)



(b)

Figure 9.2 Graphite size and distribution of the graphite nodules in the (a) base metal and (b) the weld metal.

Chemical analysis of the under-matched weld metal was carried out and the composition of the weld metal was obtained as given in Table 9.2. Figure 9.3 show the EDAX result of the electrodes used in welding process.

Table 9.2. Chemical composition of the weld metal

Element	Ni	Fe	Cu	C	Mn	Si	P	S
Percentage	92	4	2	0.5	0.7	0.7	0.012	0.02

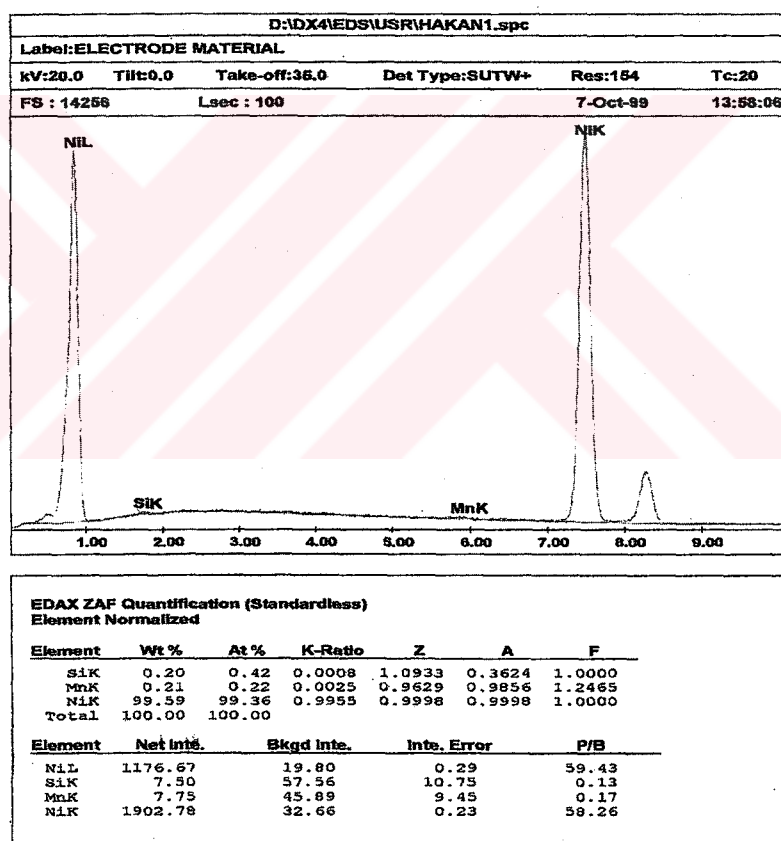


Figure 9.3 EDAX result of electrodes used in welding process.

The variations of nickel and iron amounts were investigated on two different locations (root and cap region) along the longitudinal direction of the specimens. The results are shown in Figures 9.4 and 9.5.

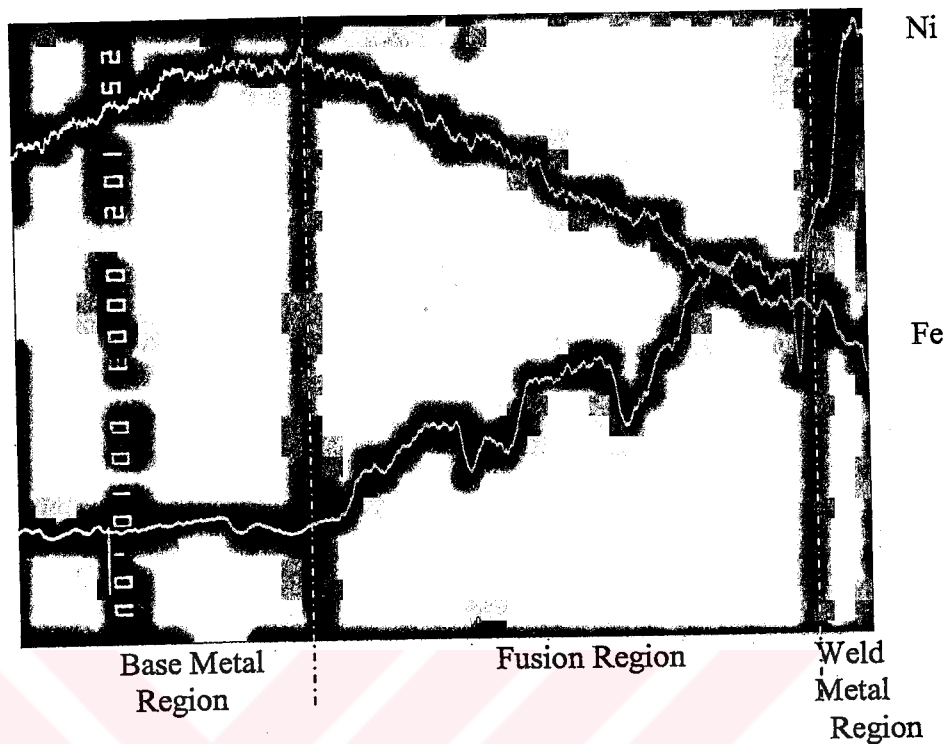


Figure 9.4. The variations of the nickel and iron amounts on the root region

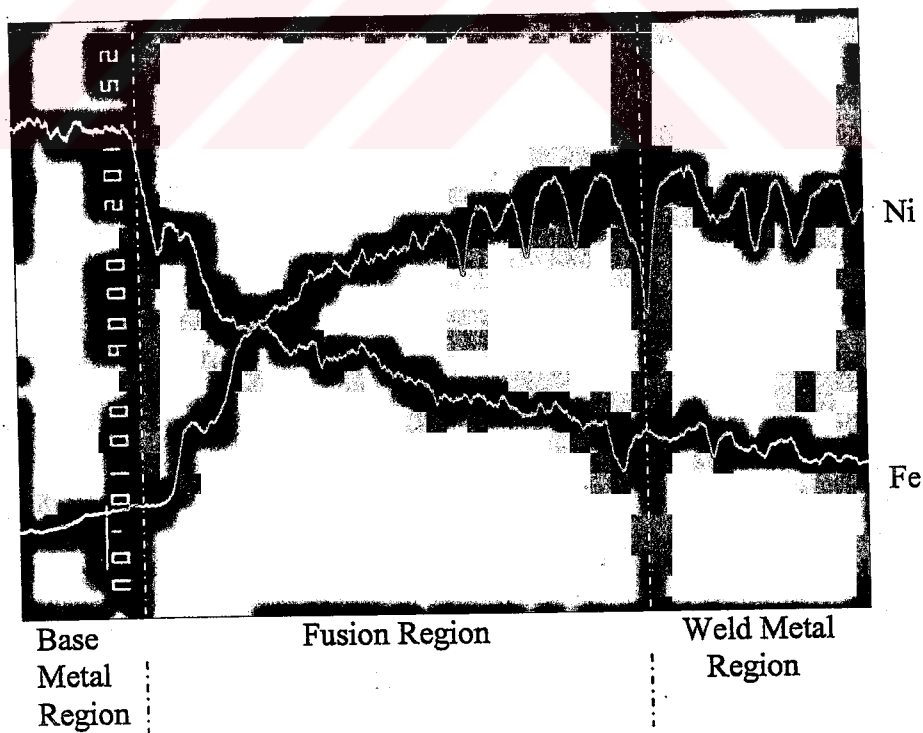


Figure 9.5. The variations of the nickel and iron amounts on the cap region

Figure 9.6 shows the microphotograph of HAZ with coarse grains. The other SEM micrograph depicts the area where Electron Back-Scatter Diffraction (EBSD) maps were obtained (Figure 9.7). In this figure, small graphite particles can be seen in weld metal region. Figures 9.8 and 9.9 show the EBSD maps obtained using a field-emission scanning electron microscope. Face-centered cubic (FCC) phase distribution in weld metal region can be seen in Figure 9.8. Figure 9.9 indicates phase distribution of the body-centered cubic ferrite in the base metal.

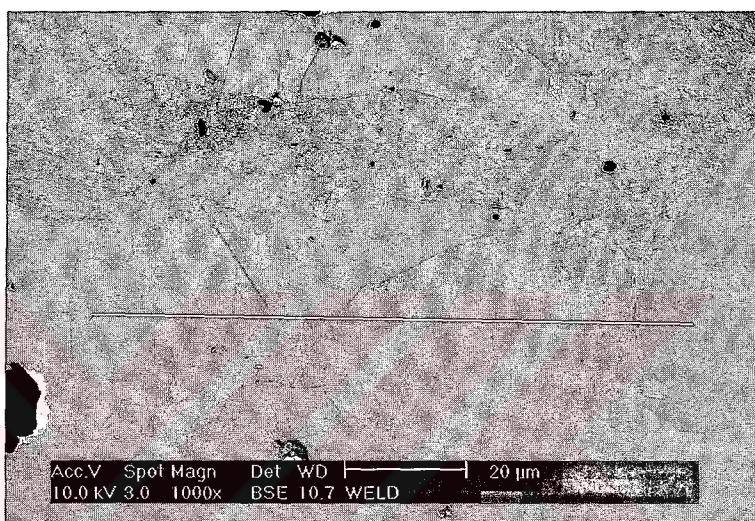


Figure 9.6. HAZ with coarse grains

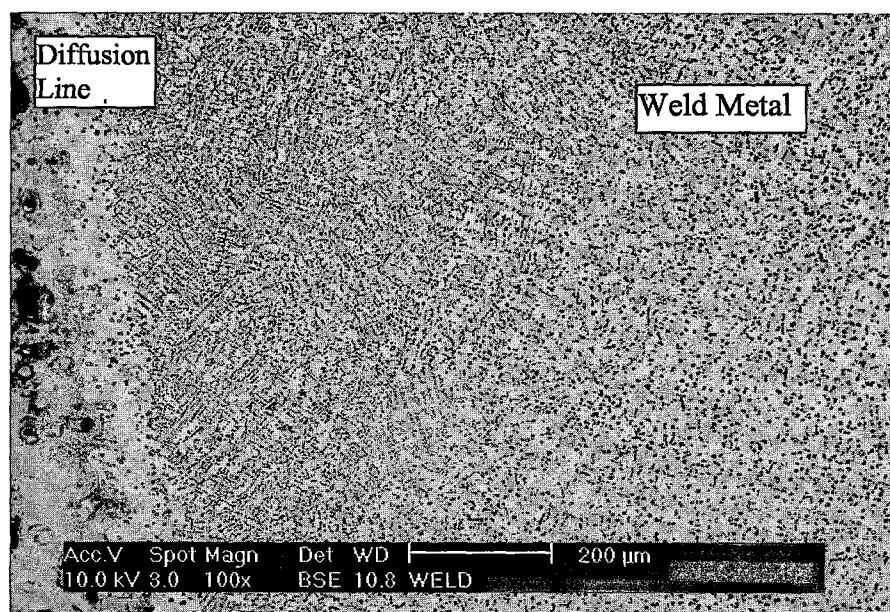


Figure 9.7 SEM micrograph of diffusion region.

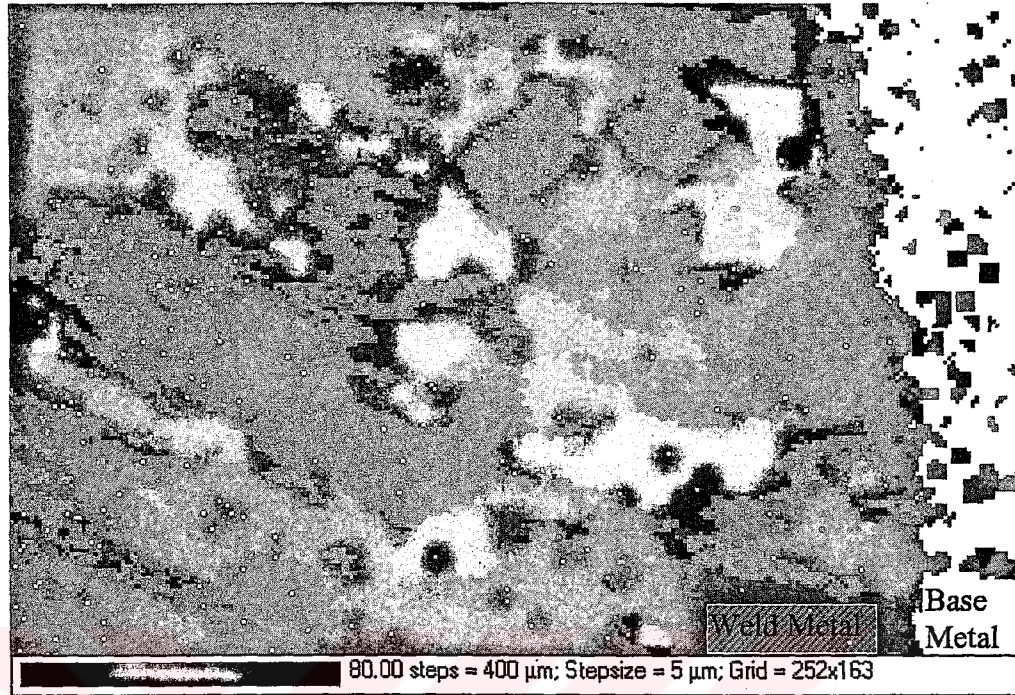


Figure 9.8 EBSD image of diffusion region (for FCC).

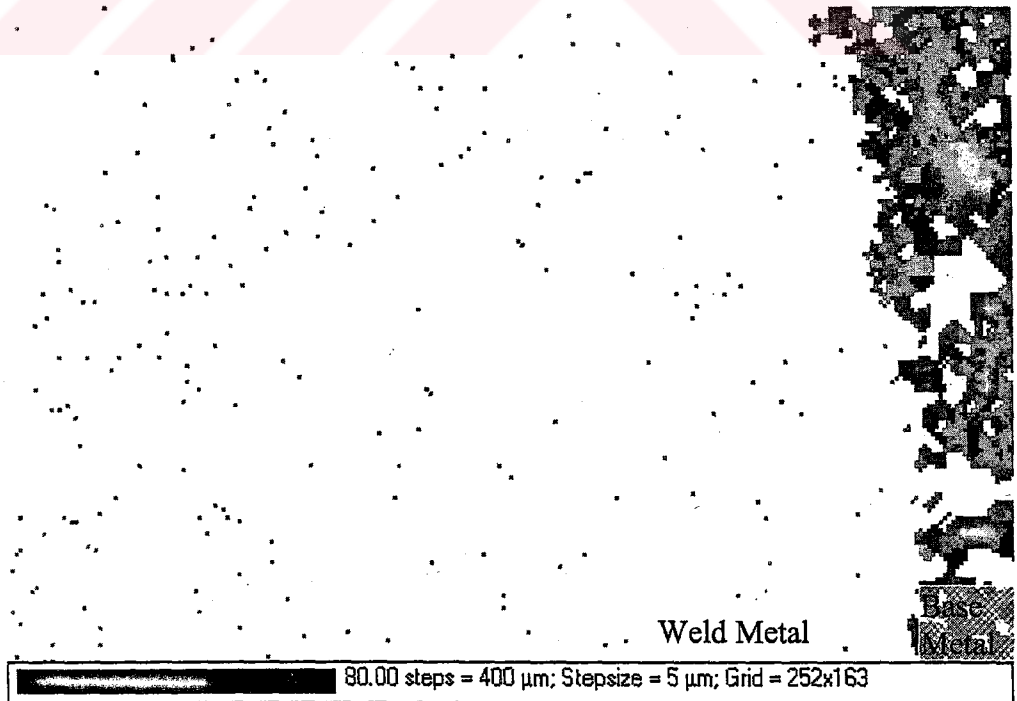


Figure 9.9 EBSD image of diffusion region (for BCC).

9.4. Fracture Toughness Properties

Load versus load line displacement and load versus crack mouth opening displacement curves were obtained by three point bending tests for four locations. Figure 9.10 depicts the load versus load line displacement curve for crack location 1. Figures 9.11 9.12, 9.13 and 9.14 show the load versus crack mouth opening displacement (CMOD) curves obtained by using extansometer for all crack locations. In these figures, curves show different character. Apart from crack location 1, loads decrease dramatically after maximum value. This kind of diagrams are called pagoda roof type load vs. CMOD diagrams (Turner, C.E. & Braga, L., 1993). Increase in compliance can be recognised for higher CMOD values.

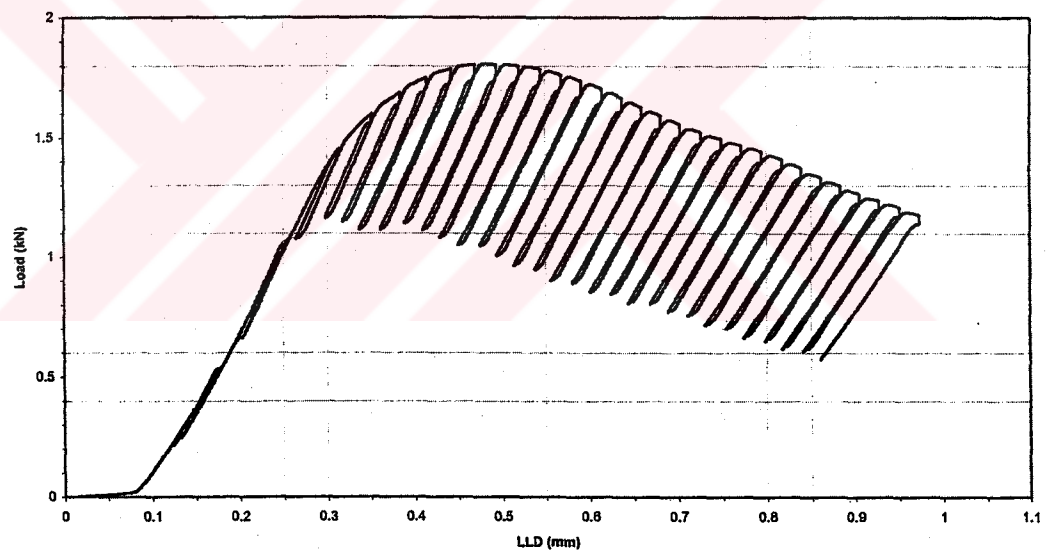


Figure 9.10. Load vs. load line displacement curve of pre-cracked three point bend specimen for location 1.

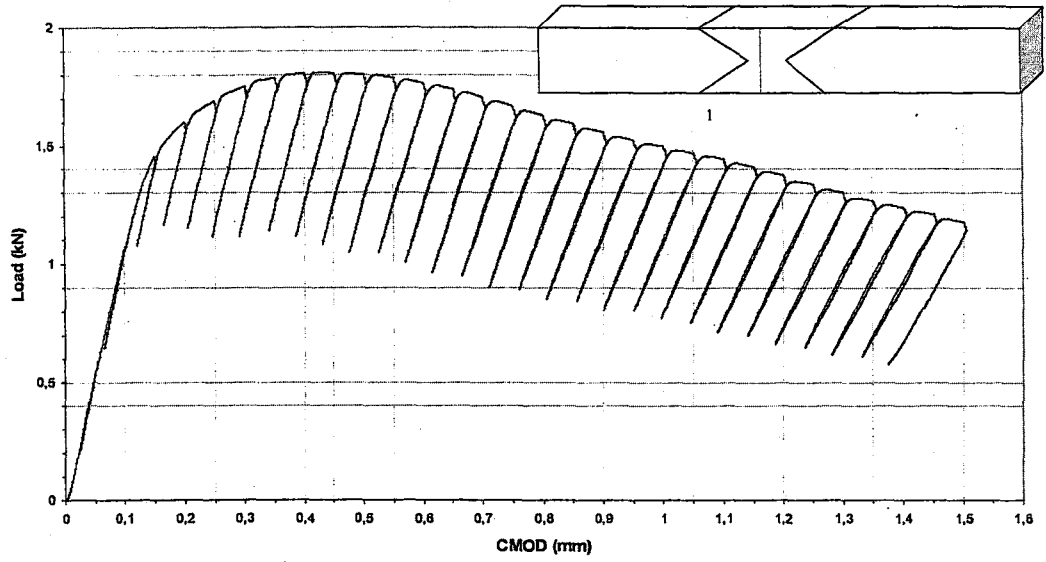


Figure 9.11. Load vs. crack mouth opening displacement curve of pre-cracked three point bend specimen for location 1.

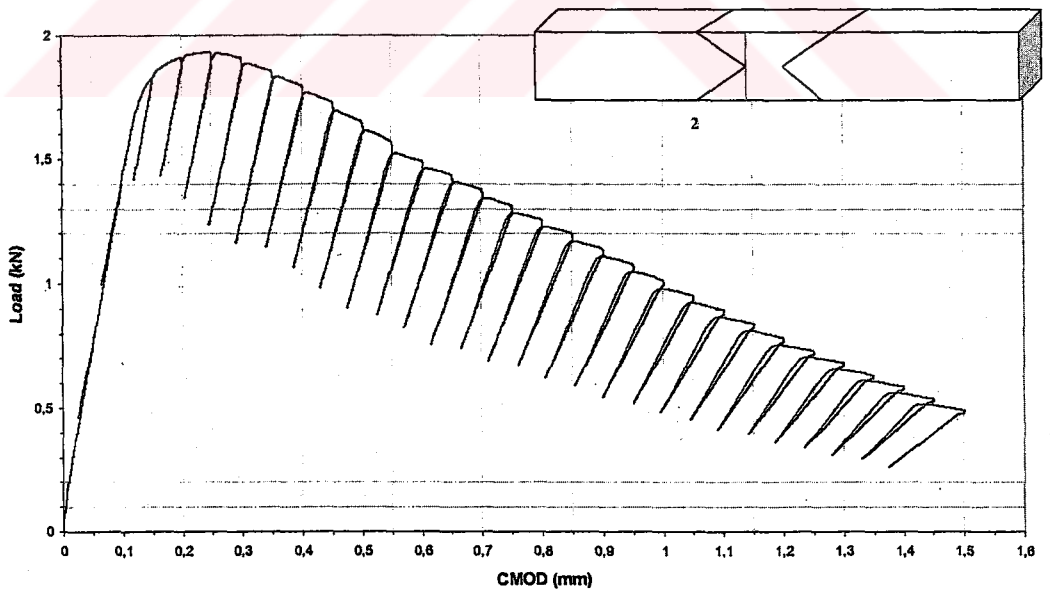


Figure 9.12. Load vs. crack mouth opening displacement curve of pre-cracked three point bend specimen for location 2.

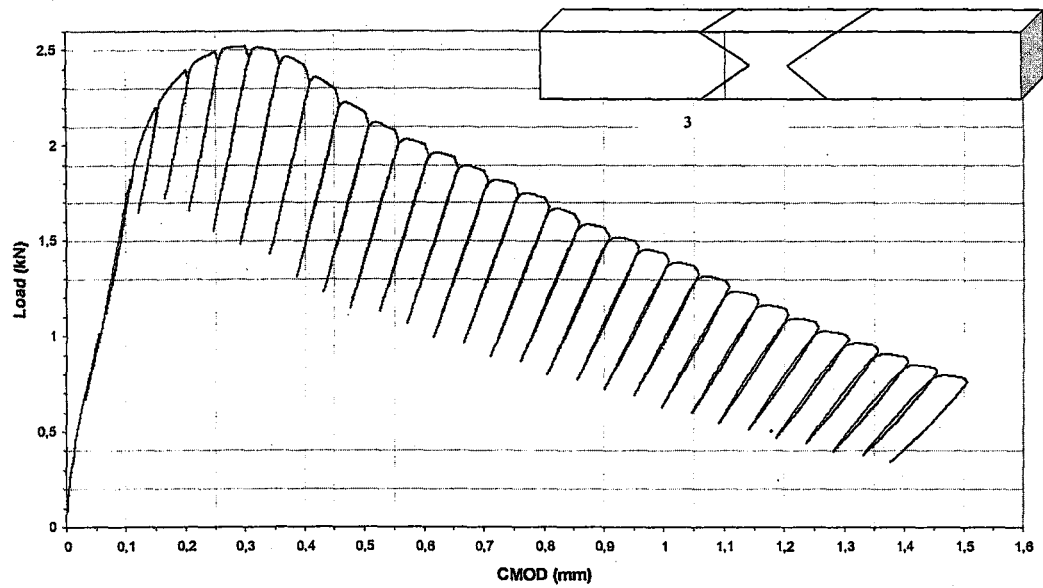


Figure 9.13. Load vs. crack mouth opening displacement curve of pre-cracked three point bend specimen for location 3.

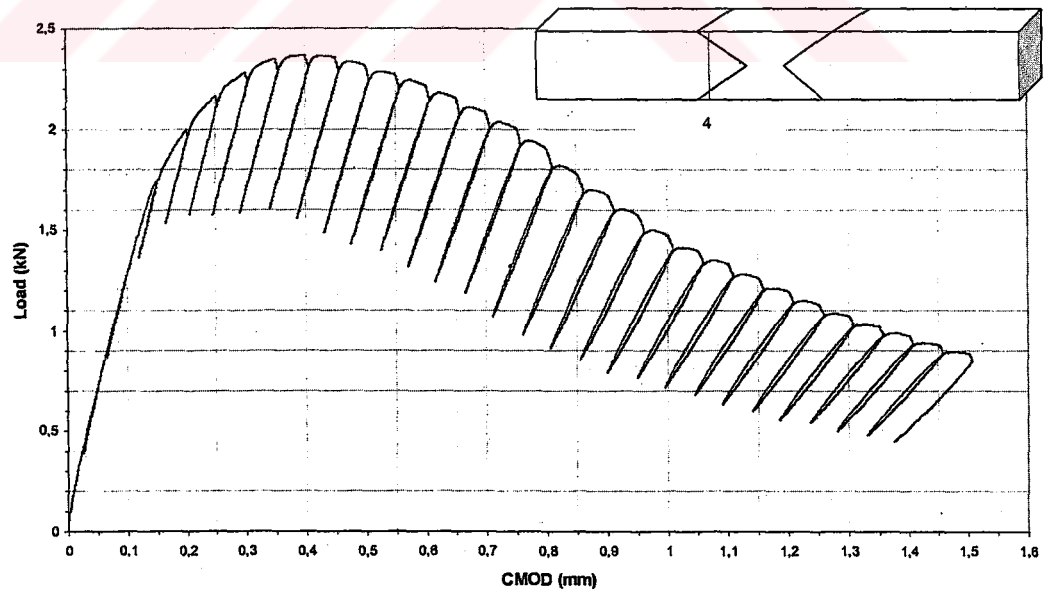


Figure 9.14. Load vs. crack mouth opening displacement curve of pre-cracked three point bend specimen for location 4.

After unload - reload sequences the each data point on the load vs. crack mouth opening displacement curves were obtained, then J-integral and crack extension values were calculated using the Equations 7.1 - 7.5. given in Chapter 7. In these equations, A is the plastic part of the area under the load - CMOD curve, which was determined by using image analyser from load-CMOD curves of four crack locations. Figures 9.15, 9.16, 9.17 and 9.18 show the load versus crack propagation curves of pre-cracked three point bending specimens for all crack locations. In crack locations 3 and 4, crack growth starts at higher values of loads. Figure 9.19 depicts the J resistance versus crack propagation curves of the materials pre-cracked on four different crack locations. As seen in this figure, base metal has the lowest resistance to crack propagation. On the other hand, weld metal (crack location 1) has the maximum resistance to crack propagation. The other locations where cracks cross over the base metal, HAZ and weld metal, have the average crack propagation resistance if it is compared with base and weld metal.

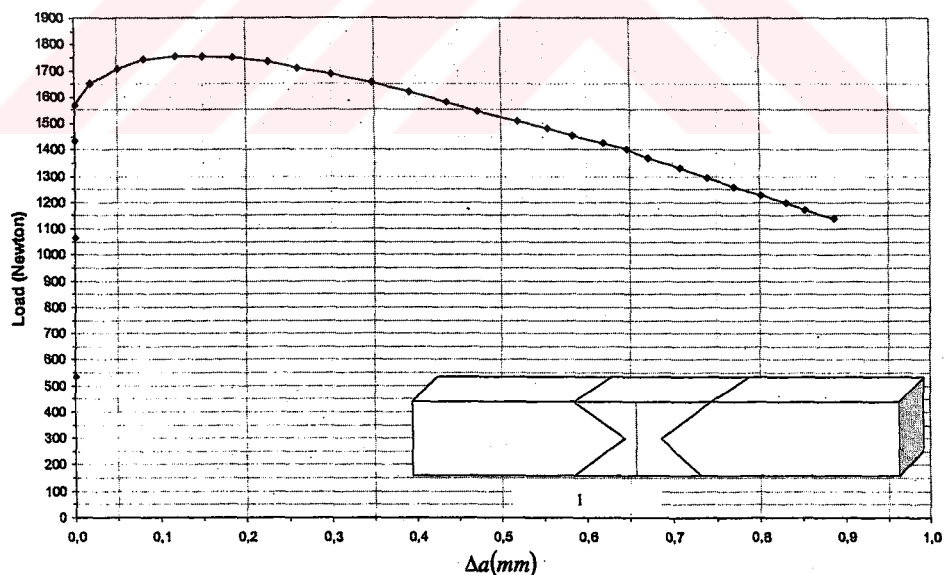


Figure 9.15. Load versus crack propagation curve of the crack on location 1.

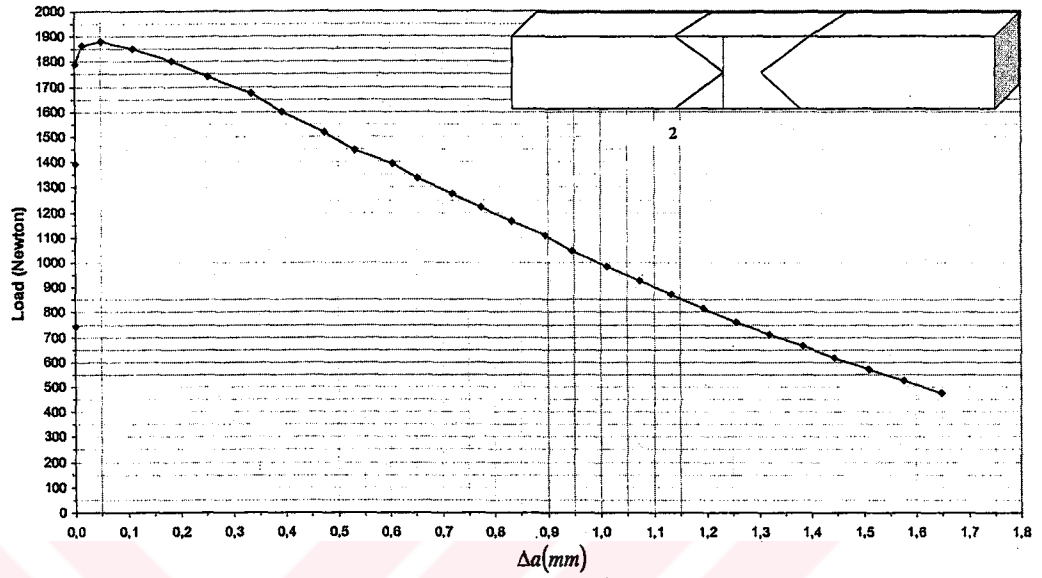


Figure 9.16. Load versus crack propagation curve of the crack on location 2.

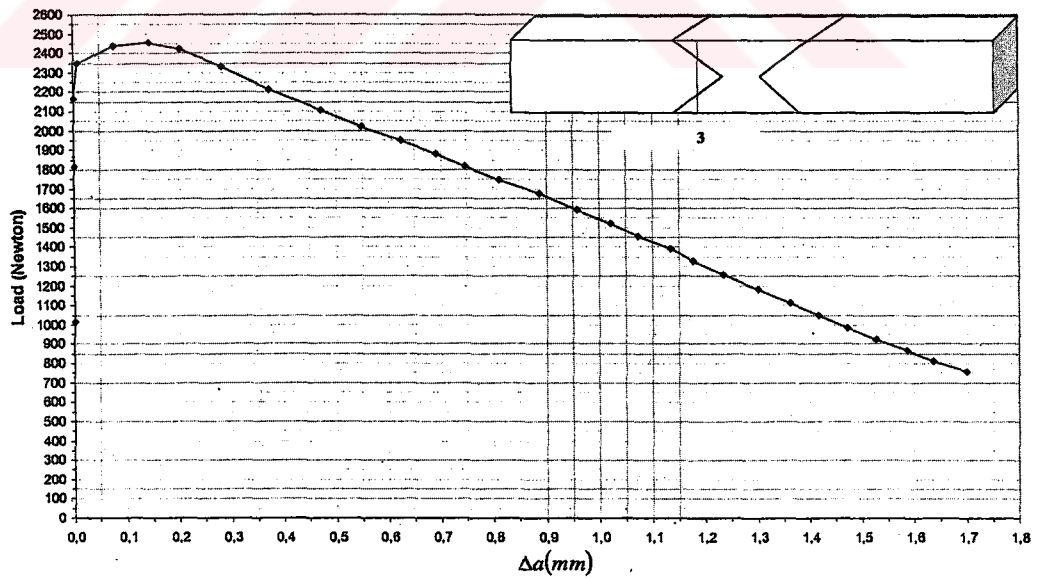


Figure 9.17. Load versus crack propagation curve of the crack on location 3.

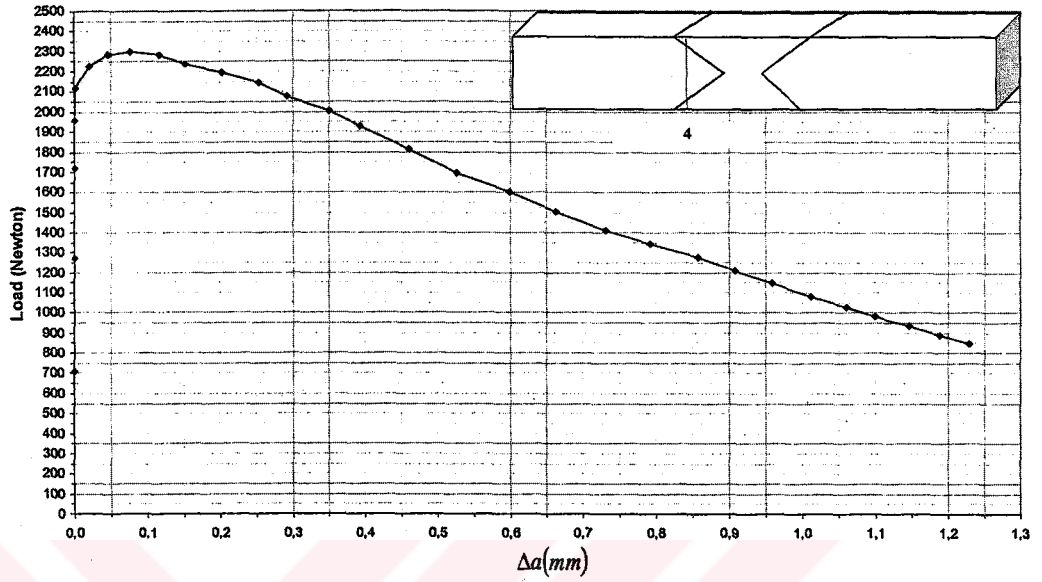


Figure 9.18. Load versus crack propagation curve of the crack on location 4.

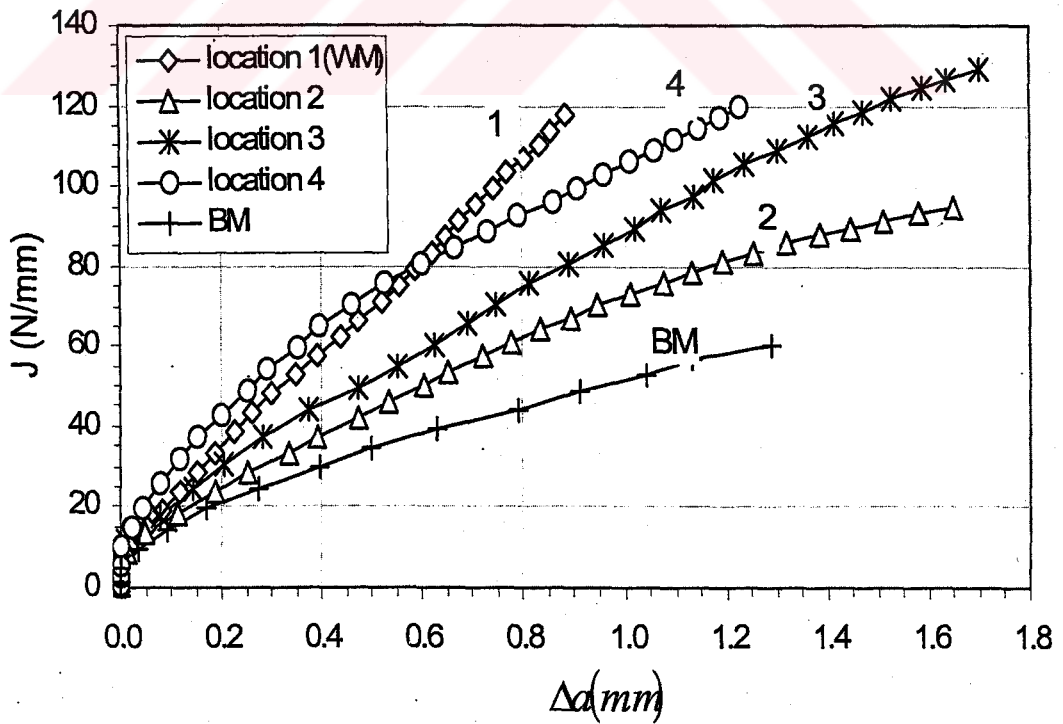


Figure 9.19. J resistance curves for all locations.

CHAPTER TEN

**RESULTS AND DISCUSSION IN TERMS OF
THEORETICAL STUDY**

10.1. Stress Triaxiality and Equivalent Plastic Strain Values around Crack Tip

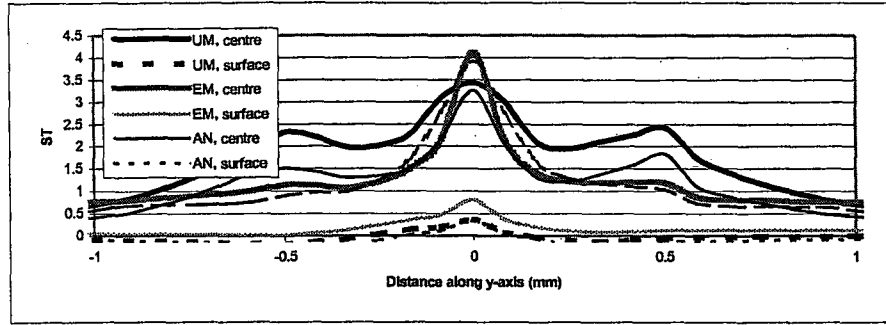
Figures from 10.1 to 10.40 show the stress triaxiality (ST) and equivalent plastic strain (EPS) values around crack tip along y-axis and crack front in the center and on the surface of the under-matched (UM), annealed weldment and even-matched (EM) models for all crack lengths on the all crack locations. Number 0 indicates the crack tip.

Figures 10.1a and 10.1b depict the stress triaxiality and equivalent plastic strain values respectively along y-axis around crack tip in the center and on the surface of the under-matched, annealed weldment and even-matched models for 5 mm crack length on the crack location 1. Number 0 indicates the crack tip. Crack location is in the weld metal for under-matched and annealed models. Thus, the center and the surface sides of the crack are in the weld metal. The variations of stress triaxiality and equivalent plastic strain appear symmetrically according to crack tip. As seen Figure 10.1a, maximum stress triaxiality occurs at the crack tip in the center of the all models. Even-matched model has the higher stress triaxiality values although under-matched and annealed models have the relatively lower values at the same point. In Figure 10.1b, the variation of equivalent plastic strain values show different character in the center and on the surface of the models. Higher equivalent plastic strain values appear in both side of the crack tip for all models. Annealed model has the higher equivalent plastic strain values as a result of its low strength value. Plastic strain extends into the weld metal and decreases the constraint around crack tip. This

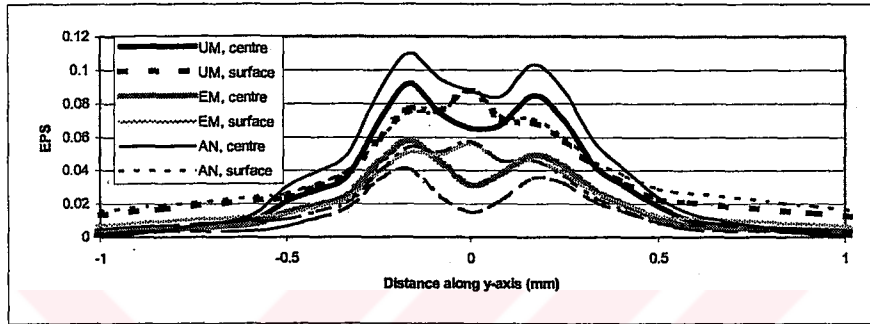
situation appears more effective in annealed model than under-matched and especially even-matched models.

Figures 10.2a and 10.2b indicate the stress triaxiality and equivalent plastic strain values respectively along crack front in the center and on the surface of the under-matched, annealed weldment and even-matched models for 5 mm crack length on the crack location 1. As seen these figures, stress triaxiality and equivalent plastic strain values reach the maximum value at crack tip and decrease along crack front for all models. The lower stress triaxiality but higher equivalent plastic strain values appear in under-matched and annealed models than that of the even-matched model. Higher plastic strain values decrease the constraint around crack tip, so lower stress triaxiality values occur.

Figures 10.3, 10.4, 10.5, 10.6, 10.7, 10.8 10.9 and 10.10 also show the stress triaxiality and equivalent plastic strain values around crack tip along y-axis and crack front in the center and on the surface of the under-matched, annealed weldment and even-matched models for crack lengths 5.05, 5.1, 5.2 and 5.85 mm on the crack location 1. In Figures 10.3a,b, 10.5a,b, 10.7a,b and 10.9a,b, the same symmetry according to crack tip can be seen in stress triaxiality and equivalent plastic strain values for other crack lengths but these values increase with growing crack lengths. As seen in Figures 10.4a,b, 10.6a,b, 10.8a,b and 10.10a,b, for all models, maximum stress triaxiality values occur at the crack tip but equivalent plastic strain values reach the maximum value away from the crack tip in the center for under-matched and annealed models, and these values become higher for longer crack lengths for all models. The maximum equivalent plastic strain values occurred away from the crack tip give a clue about void formation in the material

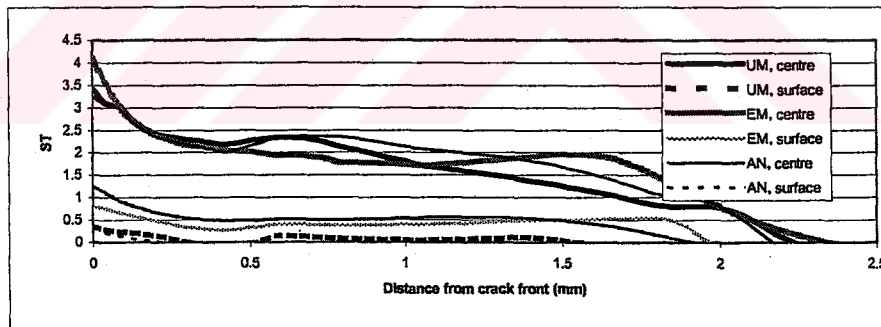


(a)

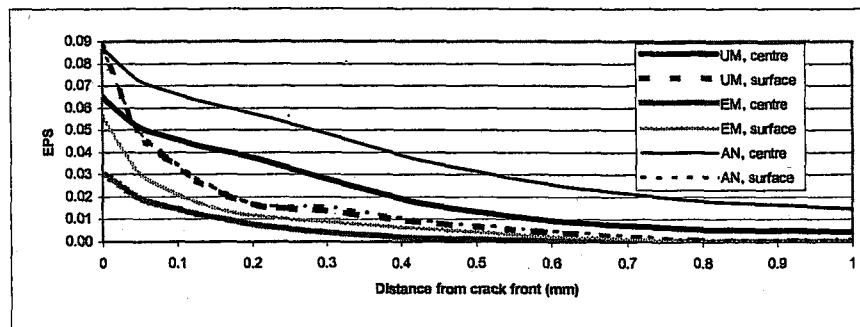


(b)

Figure 10.1. (a) Stress triaxiality, (b) equivalent plastic strain values along y axis around crack tip in the centre and on the surface of the under-matched, annealed and even-matched models for 5 mm crack length on the location 1.

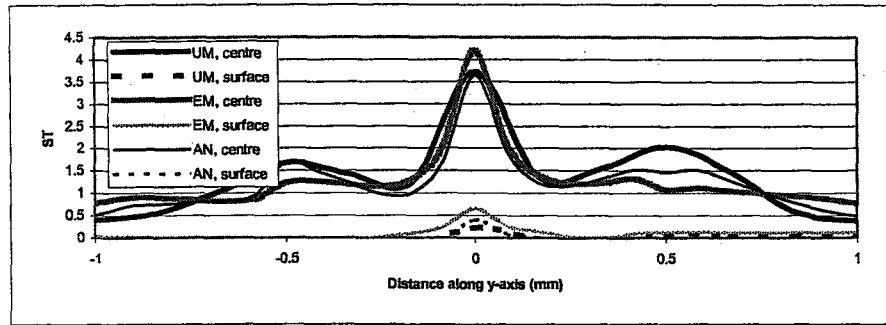


(a)

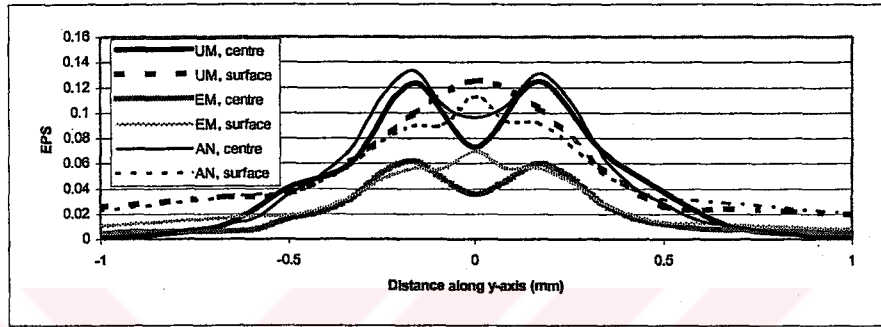


(b)

Figure 10.2. (a) Stress triaxiality, (b) equivalent plastic strain values along crack front in the centre and on the surface of the under-matched, annealed and even-matched models for 5 mm crack length on the location 1.

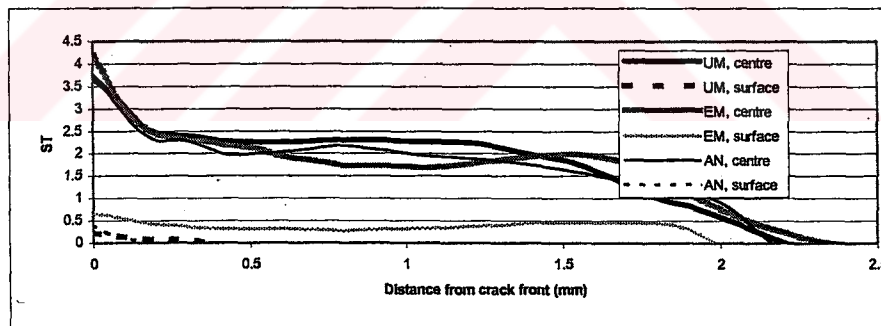


(a)

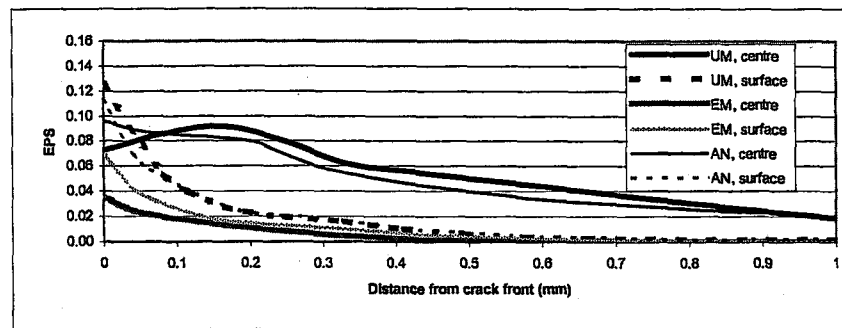


(b)

Figure 10.3. (a) Stress triaxiality, (b) equivalent plastic strain values along y axis around crack tip in the centre and on the surface of the under-matched, annealed and even-matched models for 5.05 mm crack length on the location 1.



(a)



(b)

Figure 10.4. (a) Stress triaxiality, (b) equivalent plastic strain values along crack front in the centre and on the surface of the under-matched, annealed and even-matched models for 5.05 mm crack length on the location 1.

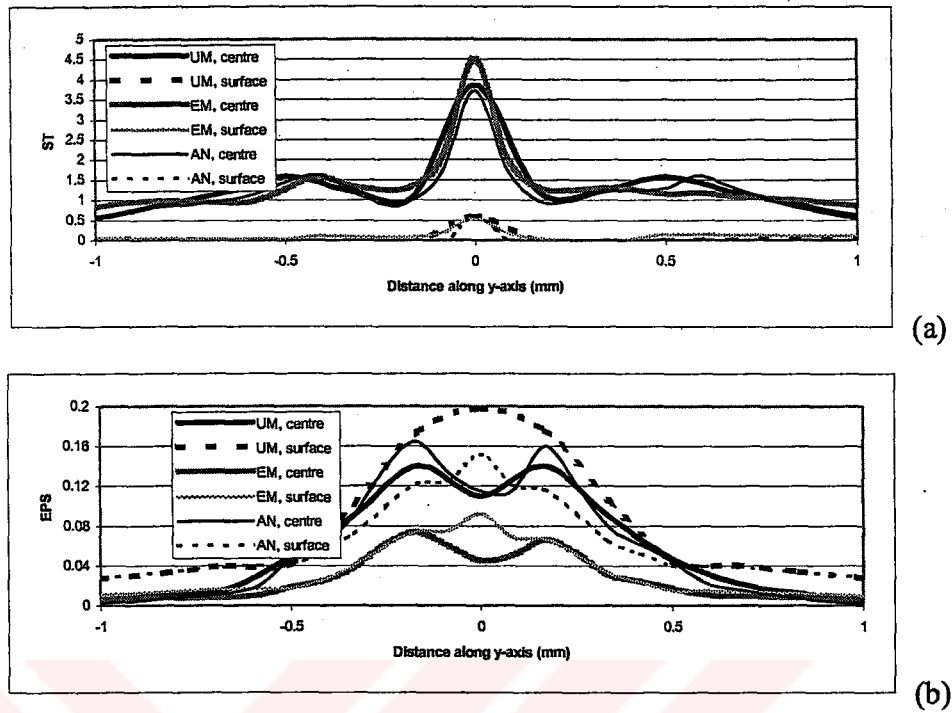


Figure 10.5. (a) Stress triaxiality, (b) equivalent plastic strain values along y axis around crack tip in the centre and on the surface of the under-matched, annealed and even-matched models for 5.1 mm crack length on the location 1.

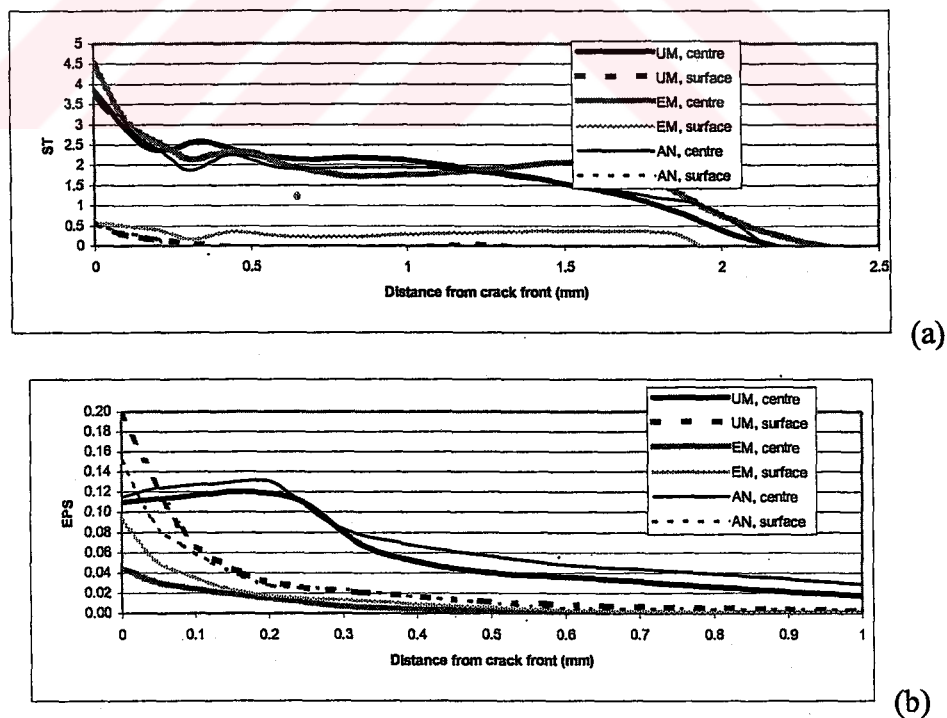


Figure 10.6. (a) Stress triaxiality, (b) equivalent plastic strain values along crack front in the centre and on the surface of the under-matched, annealed and even-matched models for 5.1 mm crack length on the location 1.

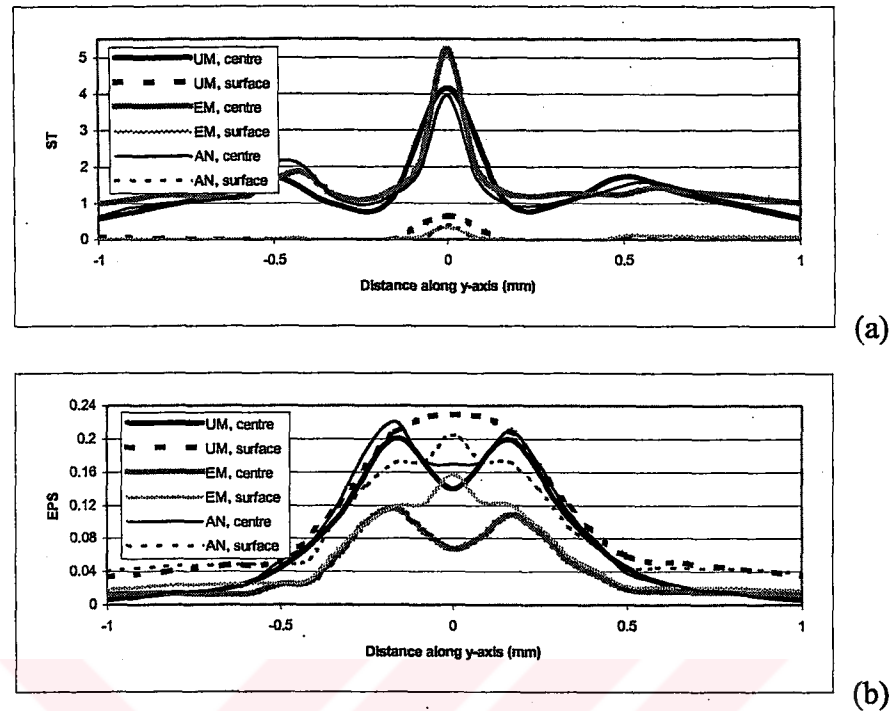


Figure 10.7. (a) Stress triaxiality, (b) equivalent plastic strain values along y axis around crack tip in the centre and on the surface of the under-matched, annealed and even-matched models for 5.2 mm crack length on the location 1.

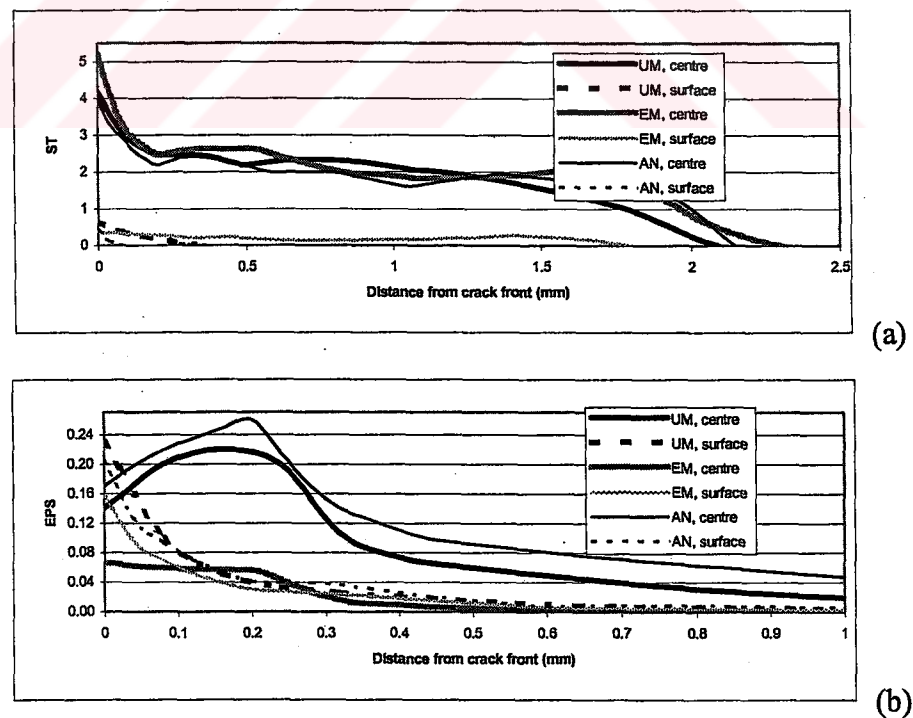
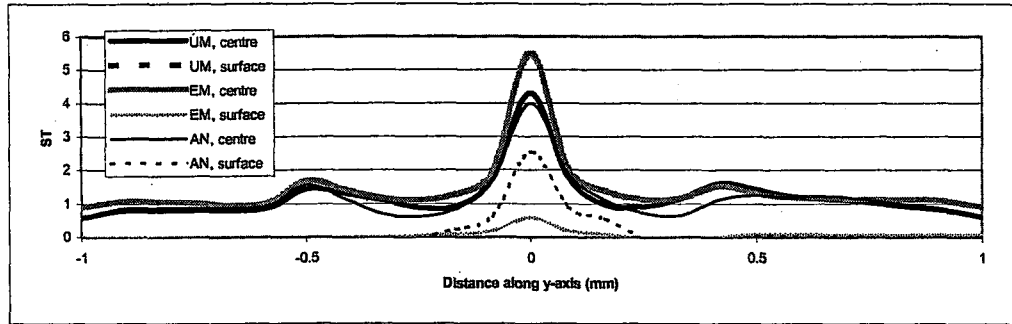
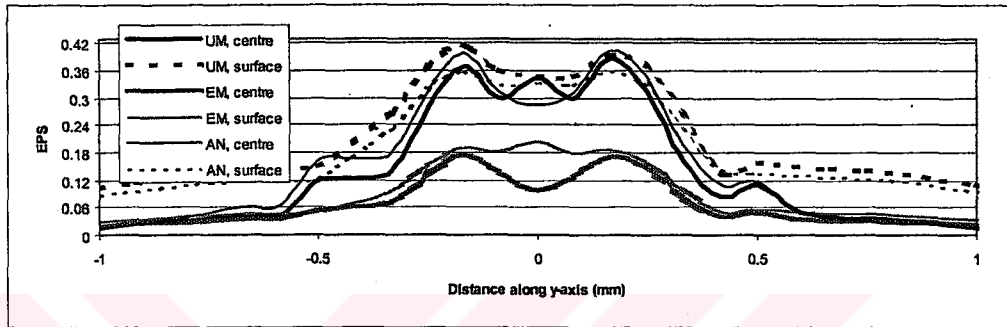


Figure 10.8. (a) Stress triaxiality, (b) equivalent plastic strain values along crack front in the centre and on the surface of the under-matched, annealed and even-matched models for 5.2 mm crack length on the location 1.

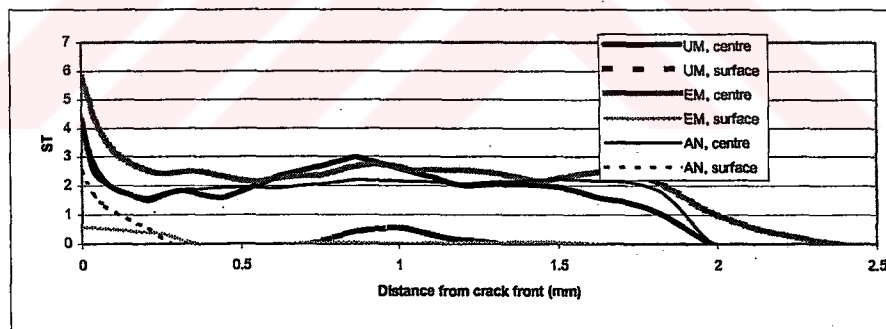


(a)

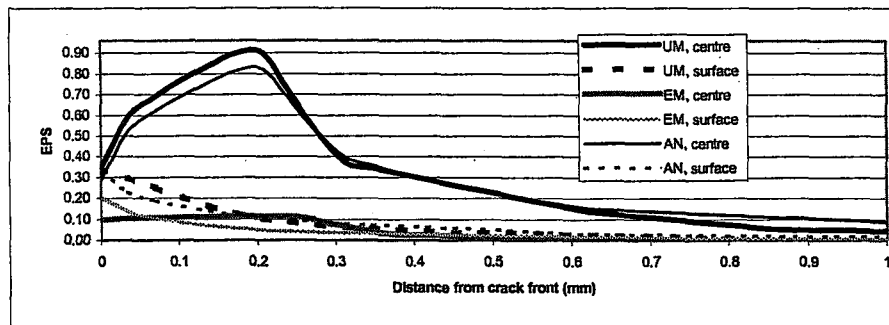


(b)

Figure 10.9. (a) Stress triaxiality, (b) equivalent plastic strain values along y axis around crack tip in the centre and on the surface of the under-matched, annealed and even-matched models for 5.85 mm crack length on the location 1.



(a)



(b)

Figure 10.10. (a) Stress triaxiality, (b) equivalent plastic strain values along crack front in the centre and on the surface of the under-matched, annealed and even-matched models for 5.85 mm crack length on the location 1.

Figures from 10.11 to 10.20 depict the stress triaxiality (ST) and equivalent plastic strain values along y-axis and along crack front in the center and on the surface of the under-matched (UM), annealed weldment and even-matched (EM) models for all crack lengths on the location 2. Number 0 indicates the crack tip. Crack location 2 is located between the base metal and the weld metal in the center of the model but both sides of the crack front are in the weld metal on the surface of the under-matched and the annealed models.

In Figures 10.11a, 10.13a, 10.15a, 10.17a and 10.19a, maximum stress triaxiality (MST) occurs in the weld metal region in the center of the UM and annealed models for all crack locations. MST values are lower on the surface than that of in the center but there is symmetry, so maximum ST occurs at the crack tip. In Figures 10.11b, 10.13b, 10.15b, 10.17b and 10.19b, maximum EPS (MEPS) values appear in the weld metal region of UM and annealed weldment models. In EM models, equivalent plastic strain reaches the maximum value on the surface for all crack lengths because constraint in the center limits the crack tip blunting. This means that material becomes more brittle and J-integral toughness values decrease for EM models.

Figures 10.12a, 10.14a, 10.16a, 10.18a and 10.20a depict the variation of ST along the crack front in the center and on the surface of UM, annealed weldments and EM models for all crack lengths on the crack location 2. In these figures, ST values in the center of the UM, annealed weldments and EM models reach the maximum values at the crack tip in all models for all crack lengths. ST values at crack tip in the center of the EM models become higher than that of UM and annealed models for all crack locations. ST values on the surface are considerably lower than that of in the center. In Figures 10.12b, 10.14b, 10.16b, 10.18b, 10.20b, EPS values at crack tip are higher on the surface than that of in the center for all models and decrease along crack front in lower crack lengths but in the longest crack length, EPS values become higher in the center than that of on the surface of the models. On the surfaces of the annealed models, EPS values become higher than that of under-matched and even-matched models.

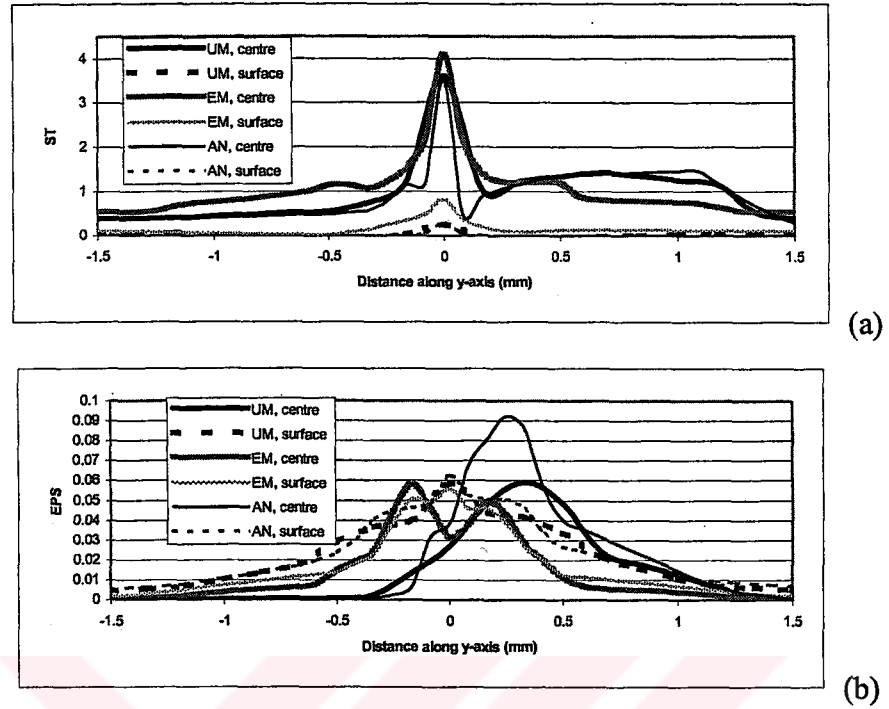


Figure 10.11. (a) Stress triaxiality, (b) equivalent plastic strain values along y axis around crack tip in the centre and on the surface of the under-matched, annealed and even-matched models for 5 mm crack length on the location 2.

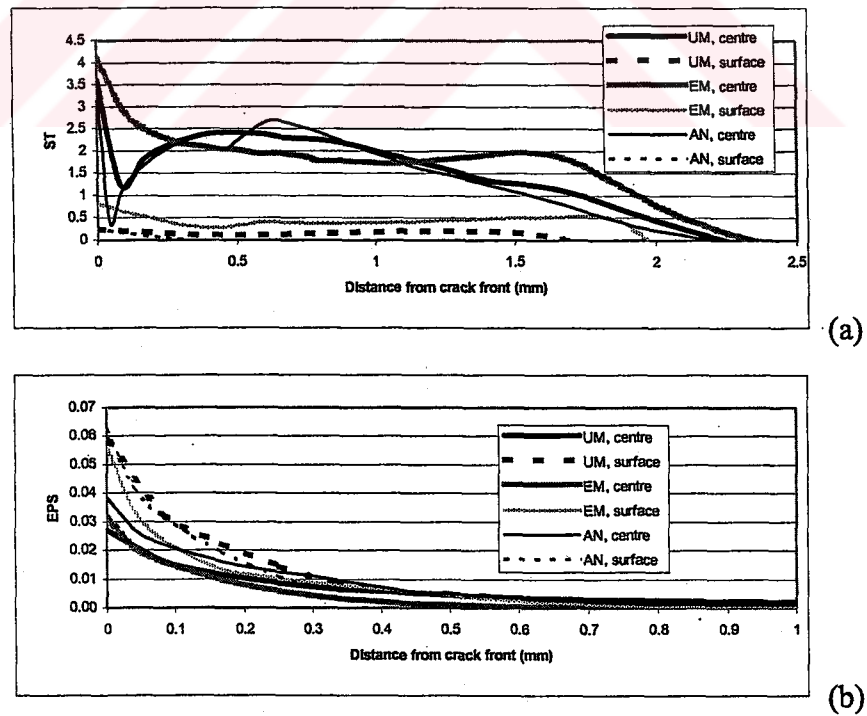


Figure 10.12. (a) Stress triaxiality, (b) equivalent plastic strain values along crack front in the centre and on the surface of the under-matched, annealed and even-matched models for 5 mm crack length on the location 2.

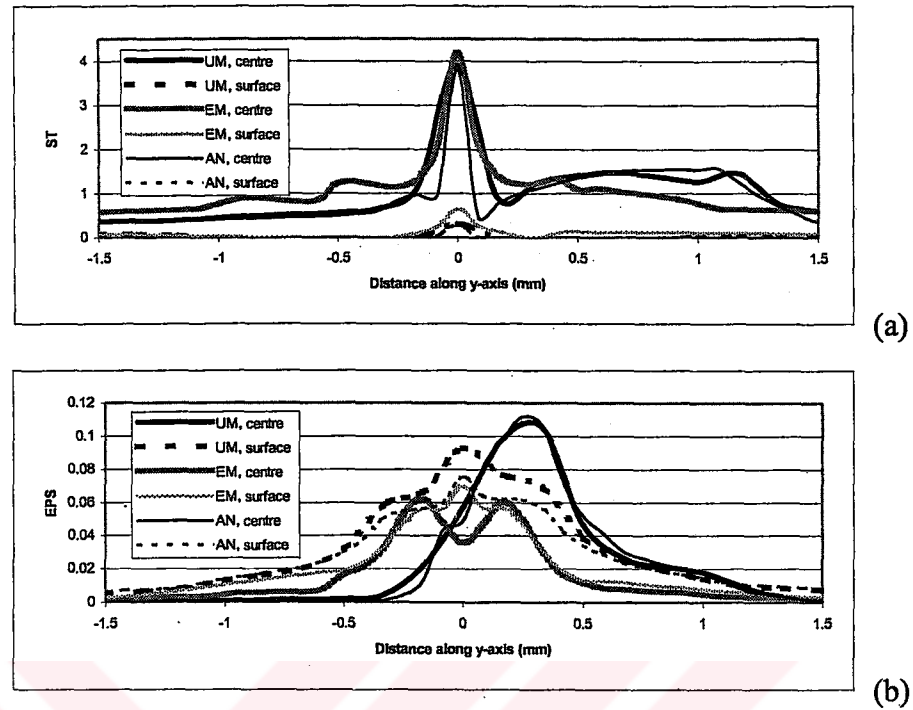


Figure 10.13. (a) Stress triaxiality, (b) equivalent plastic strain values along y axis around crack tip in the centre and on the surface of the under-matched, annealed and even-matched models for 5.05 mm crack length on the location 2.

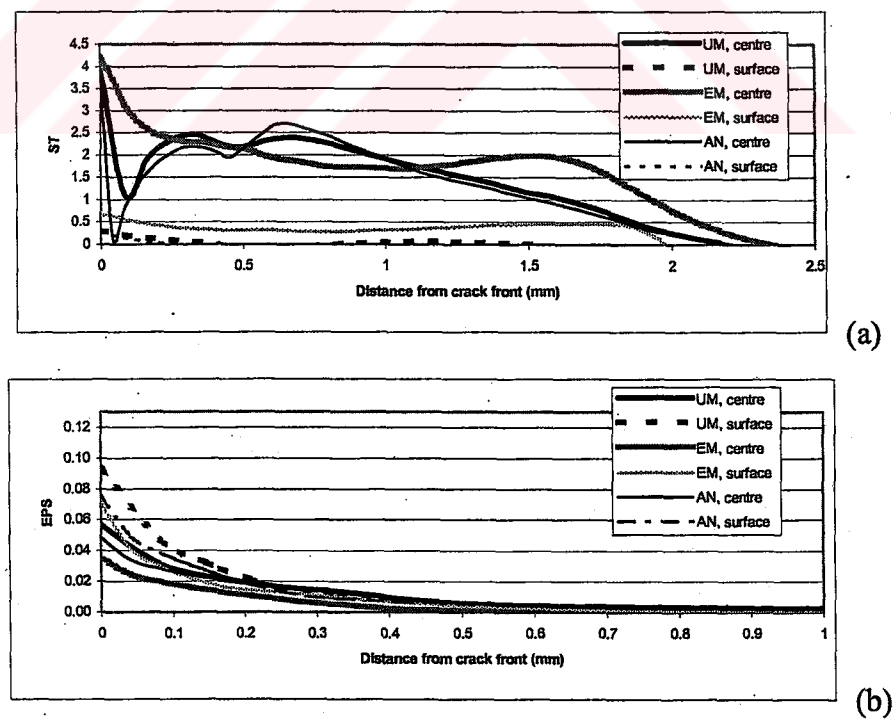


Figure 10.14. (a) Stress triaxiality, (b) equivalent plastic strain values along crack front in the centre and on the surface of the under-matched, annealed and even-matched models for 5.05 mm crack length on the location 2.

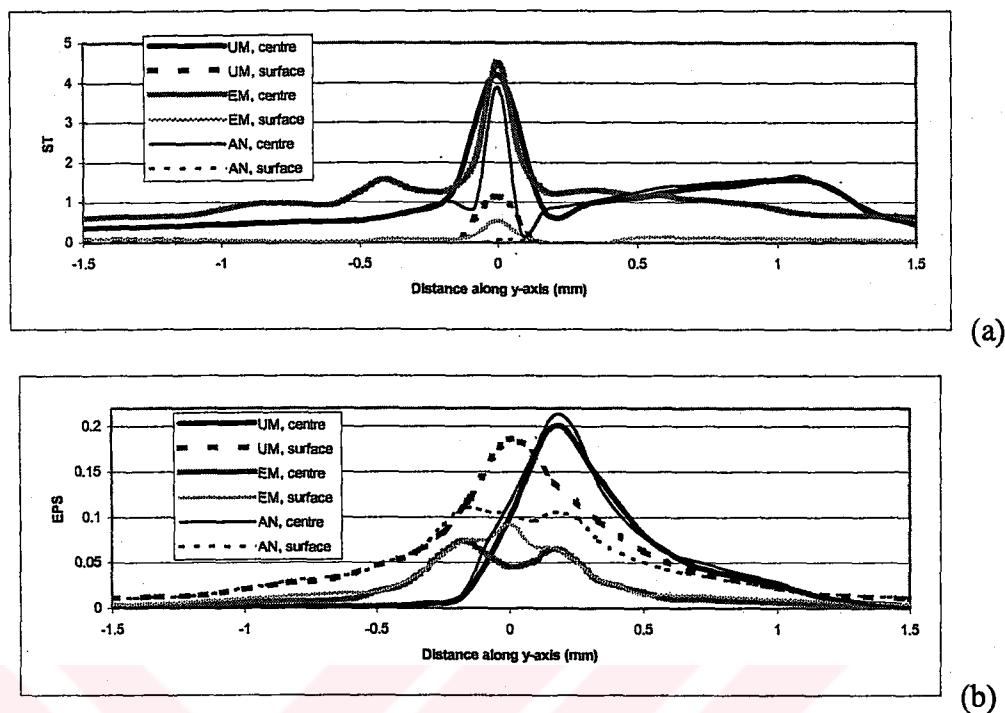


Figure 10.15. (a) Stress triaxiality, (b) equivalent plastic strain values along y axis around crack tip in the centre and on the surface of the under-matched, annealed and even-matched models for 5.1 mm crack length on the location 2.

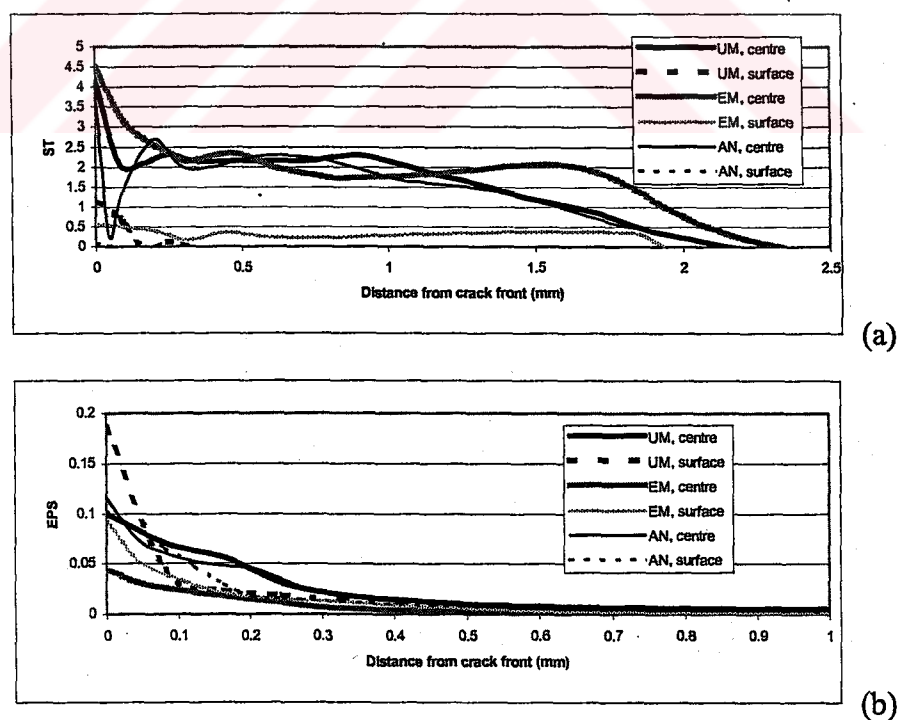


Figure 10.16. (a) Stress triaxiality, (b) equivalent plastic strain values along crack front in the centre and on the surface of the under-matched, annealed and even-matched models for 5.1 mm crack length on the location 2.

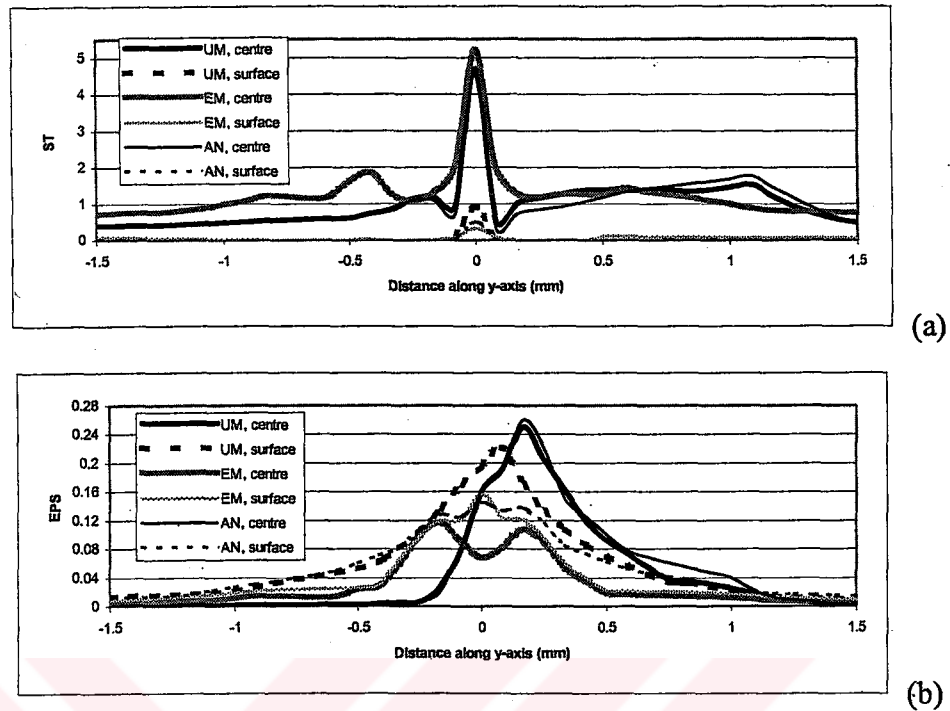


Figure 10.17. (a) Stress triaxiality, (b) equivalent plastic strain values along y axis around crack tip in the centre and on the surface of the under-matched, annealed and even-matched models for 5.2 mm crack length on the location 2.

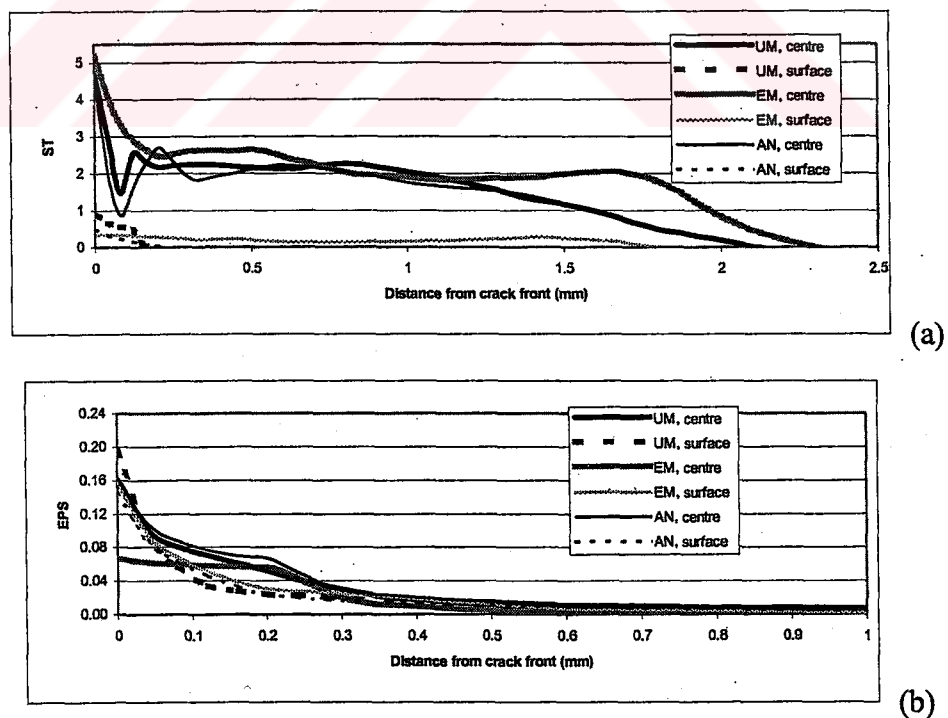
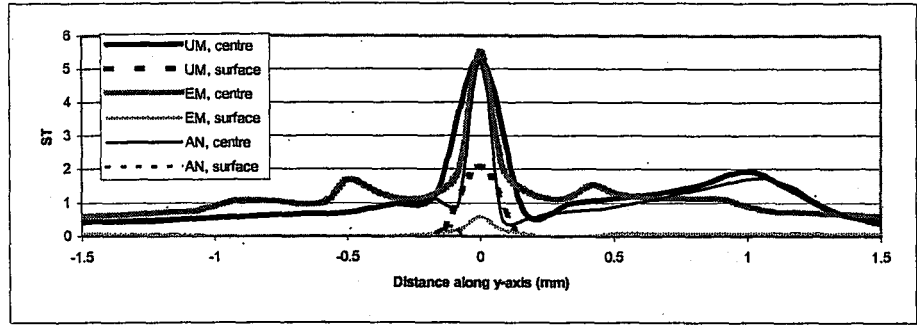
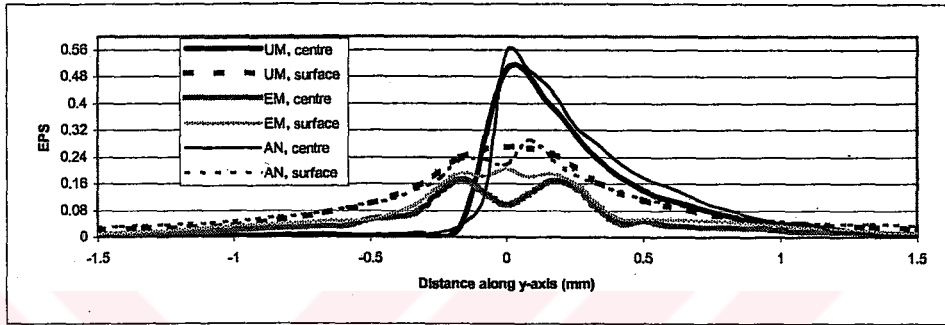


Figure 10.18. (a) Stress triaxiality, (b) equivalent plastic strain values along crack front in the centre and on the surface of the under-matched, annealed and even-matched models for 5.2 mm crack length on the location 2.

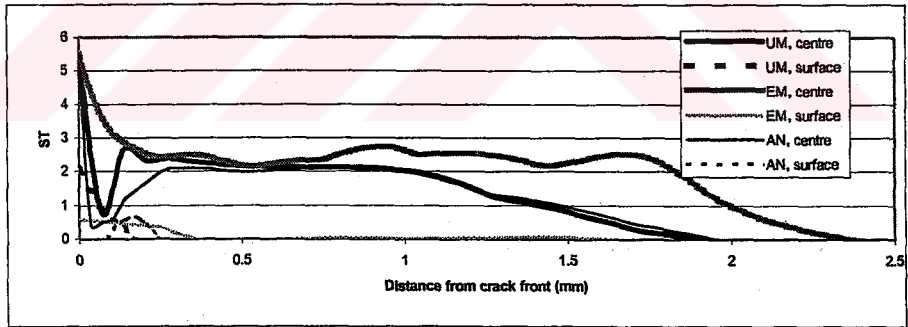


(a)

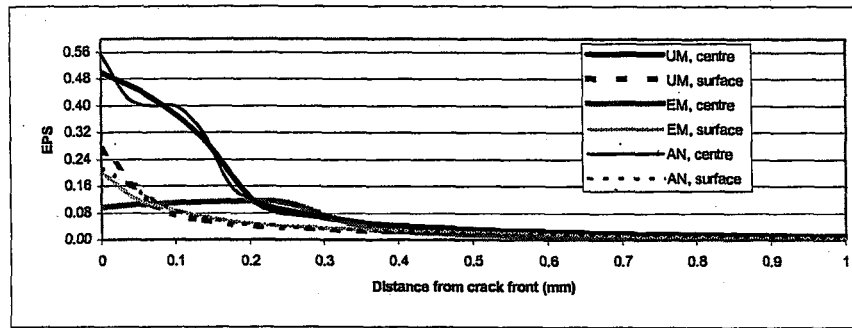


(b)

Figure 10.19. (a) Stress triaxiality, (b) equivalent plastic strain values along y axis around crack tip in the centre and on the surface of the under-matched, annealed and even-matched models for 5.85 mm crack length on the location 2.



(a)



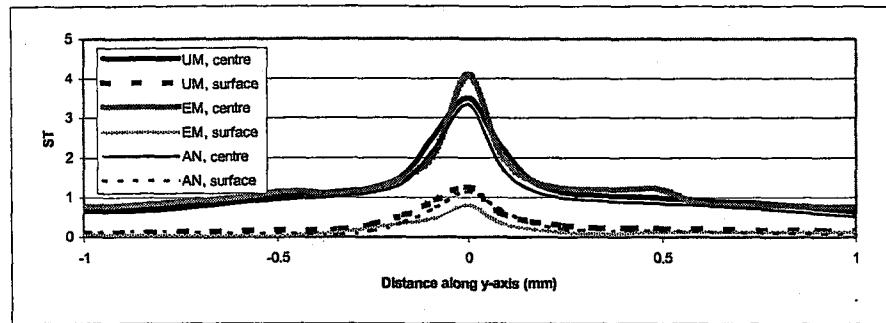
(b)

Figure 10.20. (a) Stress triaxiality, (b) equivalent plastic strain values along crack front in the centre and on the surface of the under-matched weld, annealed and even-matched models for 5.85 mm crack length on the location 2.

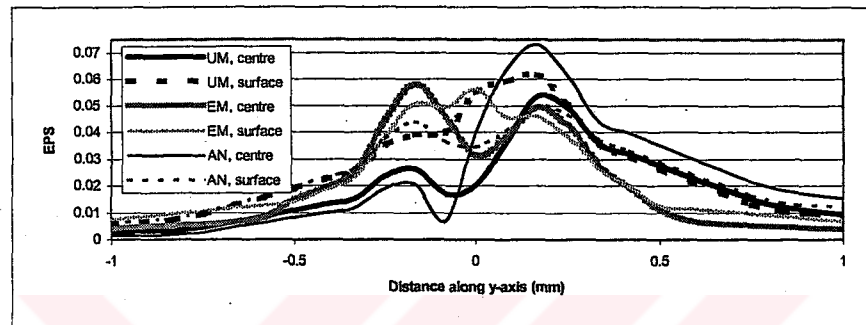
Figures from 10.21 to 10.30 depict the stress triaxiality and equivalent plastic strain values along y-axis and along crack front in the center and on the surface of the under-matched, annealed and even-matched models for all crack lengths on the crack location 3. Number 0 indicates the crack tip. On this location, center part of the crack is in the base metal but surface part of the crack is in the weld metal.

In Figures 10.21a, 10.23a, 10.25a, 10.27a and 10.29a, the variation of stress triaxiality along y-axis around crack tip in the center and on the surface of the under-matched, annealed and even-matched models for all crack lengths can be seen. Maximum stress triaxiality occurs at crack tip. Even-matched models have the higher stress triaxiality values at crack tip in the center of the models than that of under-matched and annealed models because plastic deformation extends free surfaces in UM and annealed models. Figures 10.21b, 10.23b, 10.25b, 10.27b and 10.29b indicate the variations of equivalent plastic strain values along crack front in the center and on the surface of the under-matched, annealed weld and even-matched models for all crack lengths. In the under-matched models, equivalent plastic strain on the surface reaches higher values than that of in the center, because surface part of the crack is in the weld metal which has lower strength value. Thus, loss of constraint occurs because plasticity extends to a free surface. EPS values alternate significantly around crack tip on the surface and in the center parts of the cracks.

Figures 10.22a, 10.24a, 10.26a, 10.28a and 10.30a show the ST values along crack front in the center and on the surface of the UM, annealed weld and EM models for all crack lengths. There is no significant difference between ST values at crack tip for UM, EM and annealed models but even-matched models have slightly higher ST values at crack tip than that of UM and annealed models. Figures 10.22b, 10.24b, 10.26b, 10.28b and 10.30b depict the EPS values along crack front in the center and on the surface of the UM, annealed weld and EM models for all crack lengths. In UM and annealed models, maximum EPS values occur at the crack tip on the surfaces of the models because surface parts of the cracks are in the weld metal which has lower strength value. This situation causes the loss of constraint in the center due to extension of the plastic deformation to the free surface.

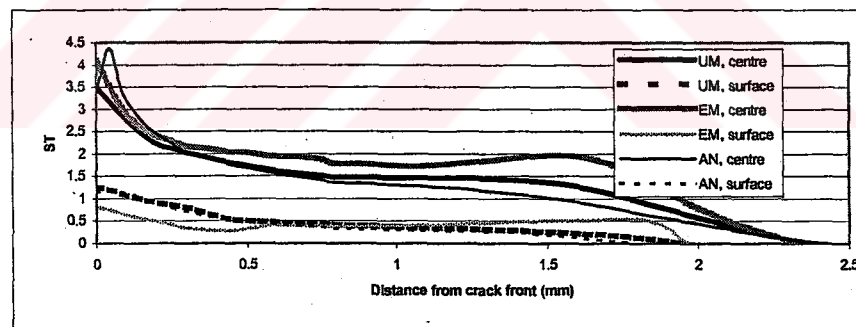


(a)

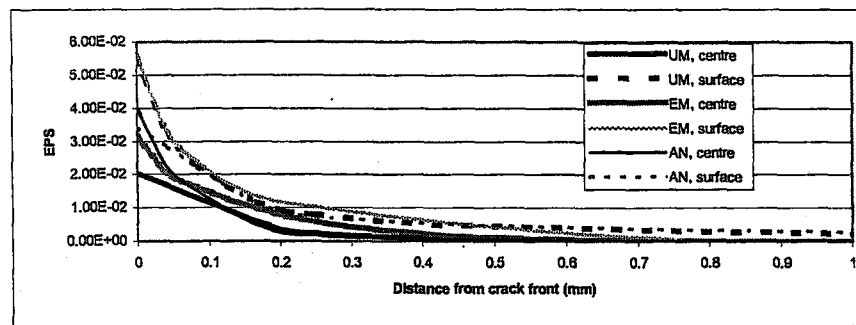


(b)

Figure 10.21. (a) Stress triaxiality, (b) equivalent plastic strain values along y axis around crack tip in the centre and on the surface of the under-matched, annealed and even-matched models for 5 mm crack length on the location 3.



(a)



(b)

Figure 10.22. (a) Stress triaxiality, (b) equivalent plastic strain values along crack front in the centre and on the surface of the under-matched, annealed weld and even-matched models for 5 mm crack length on the location 3.

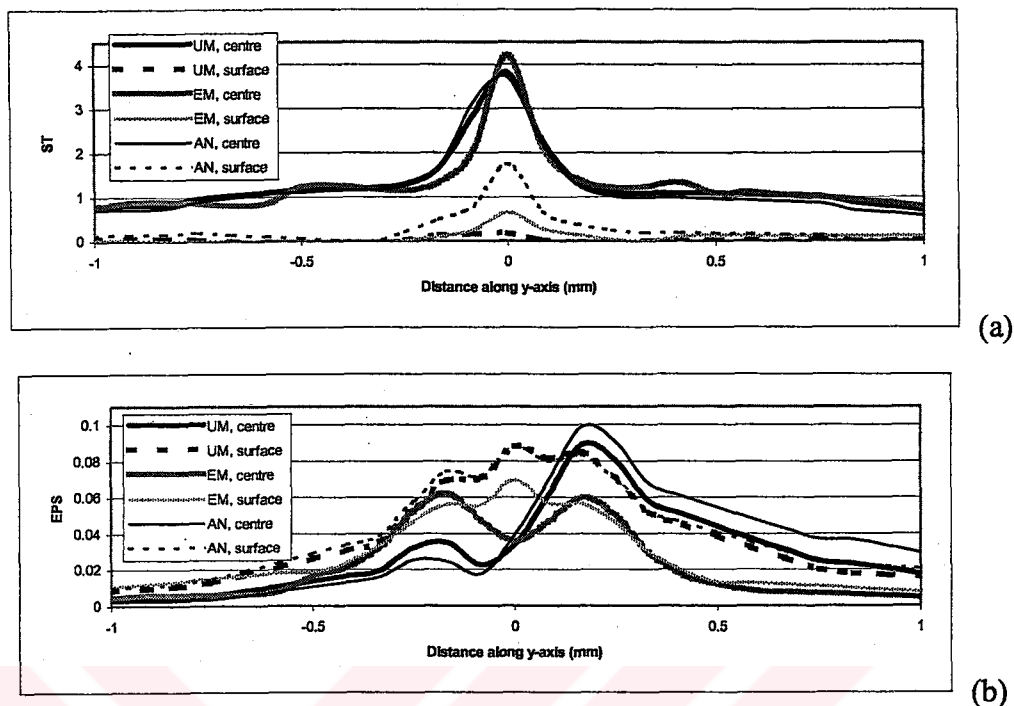


Figure 10.23. (a) Stress triaxiality, (b) equivalent plastic strain values along y axis around crack tip in the centre and on the surface of the under-matched, annealed and even-matched models for 5.05 mm crack length on the location 3.

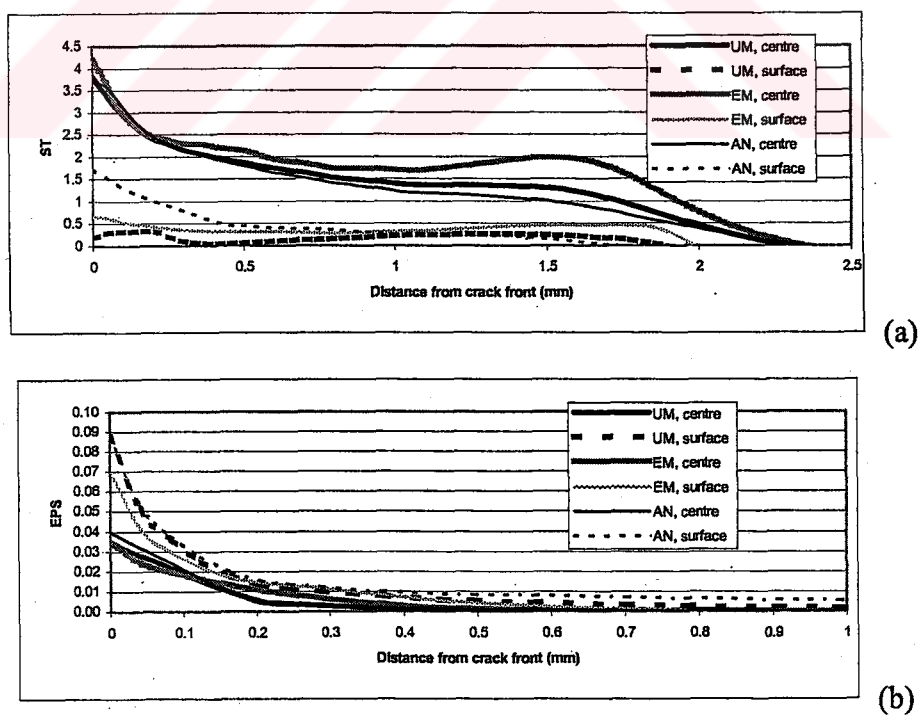


Figure 10.24. (a) Stress triaxiality, (b) equivalent plastic strain values along crack front in the centre and on the surface of the under-matched, annealed and even-matched models for 5.05 mm crack length on the location 3.

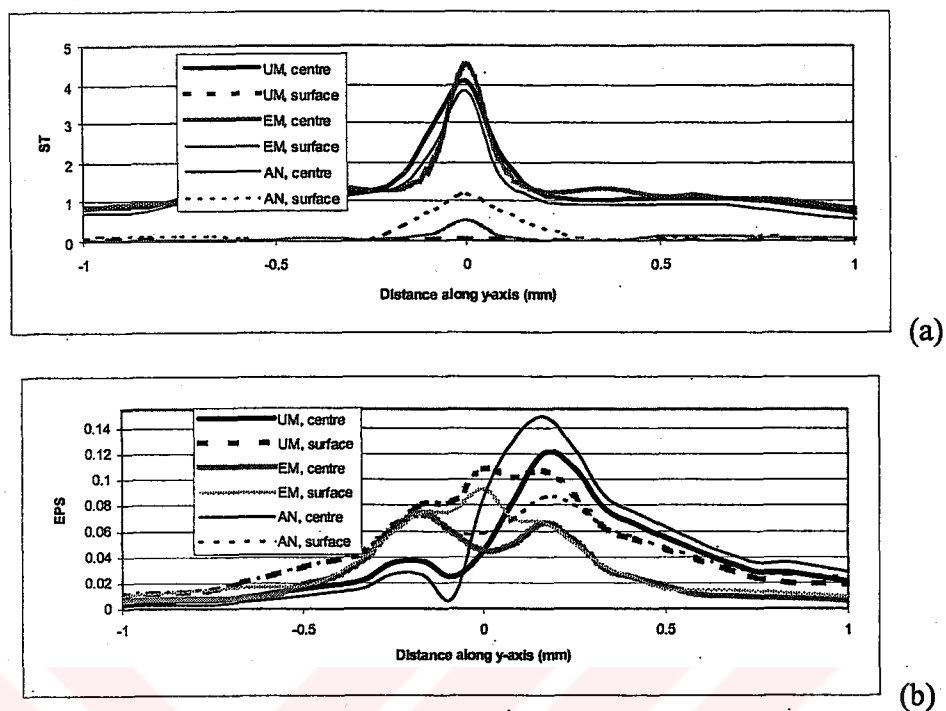


Figure 10.25. (a) Stress triaxiality, (b) equivalent plastic strain values along y axis around crack tip in the centre and on the surface of the under-matched, annealed and even-matched models for 5.1 mm crack length on the location 3.

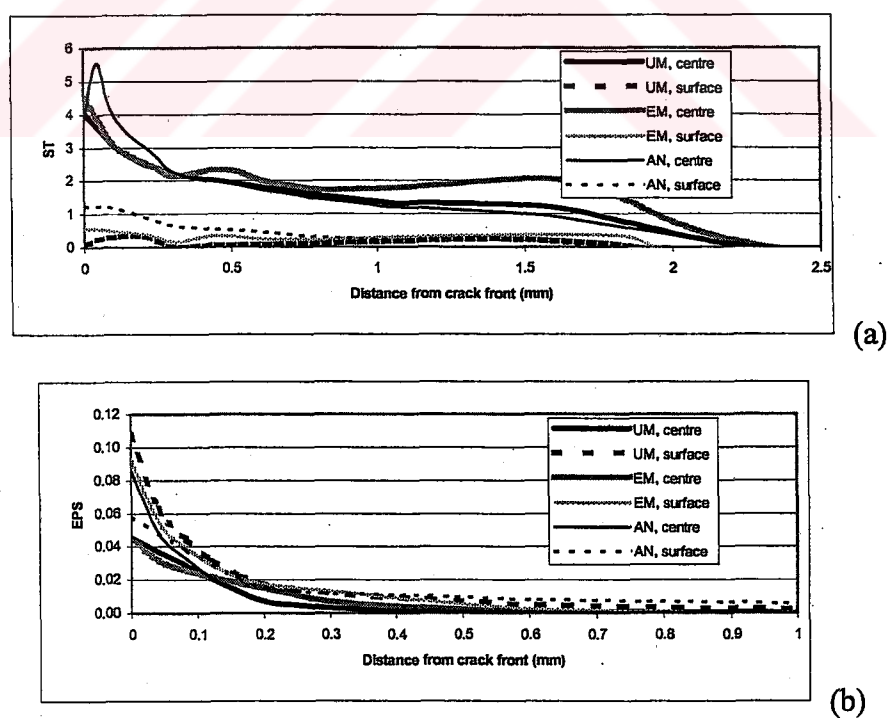


Figure 10.26. (a) Stress triaxiality, (b) equivalent plastic strain values along crack front in the centre and on the surface of the under-matched, annealed and even-matched models for 5.1 mm crack length on the location 3.

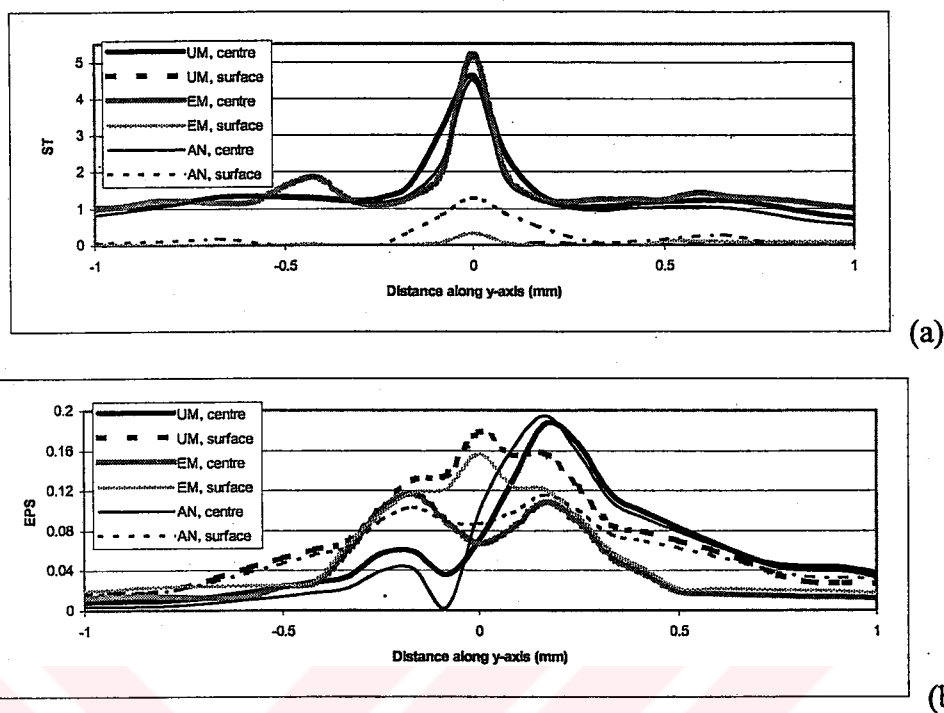


Figure 10.27. (a) Stress triaxiality, (b) equivalent plastic strain values along y axis around crack tip in the centre and on the surface of the under-matched, annealed and even-matched models for 5.2 mm crack length on the location 3.

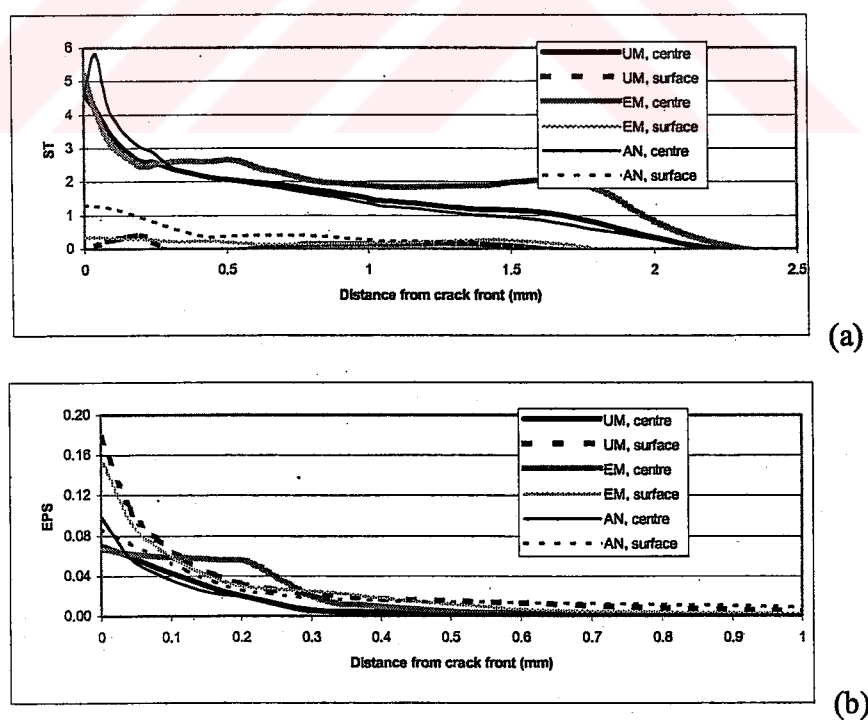


Figure 10.28. (a) Stress triaxiality, (b) equivalent plastic strain values along crack front in the centre and on the surface of the under-matched, annealed and even-matched models for 5.2 mm crack length on the location 3.

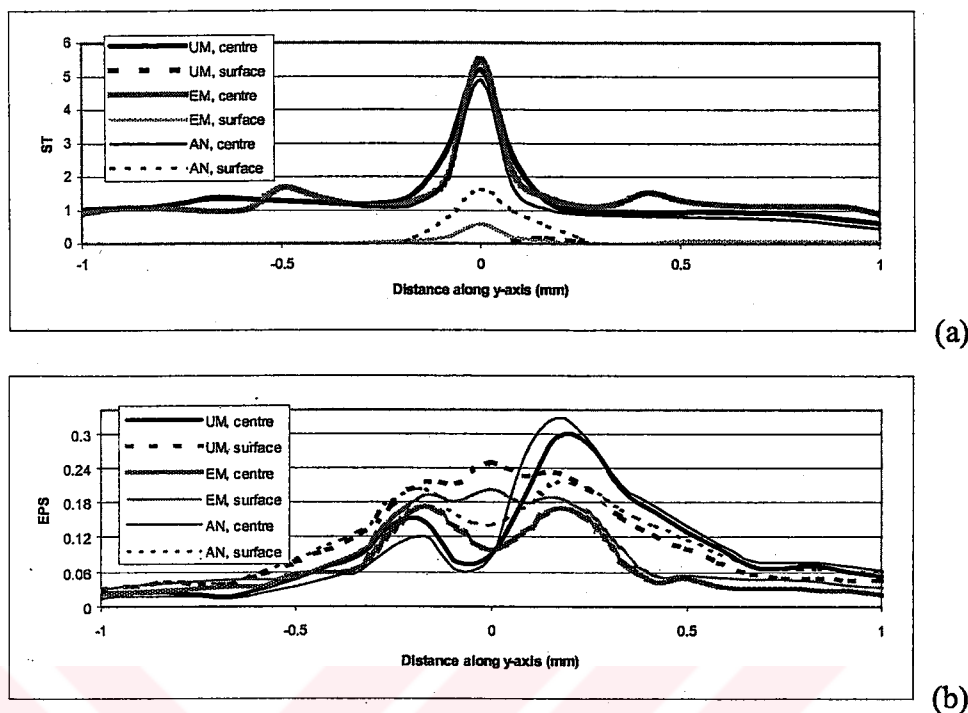


Figure 10.29. (a) Stress triaxiality, (b) equivalent plastic strain values along y axis around crack tip in the centre and on the surface of the under-matched, annealed and even-matched models for 5.85 mm crack length on the location 3.

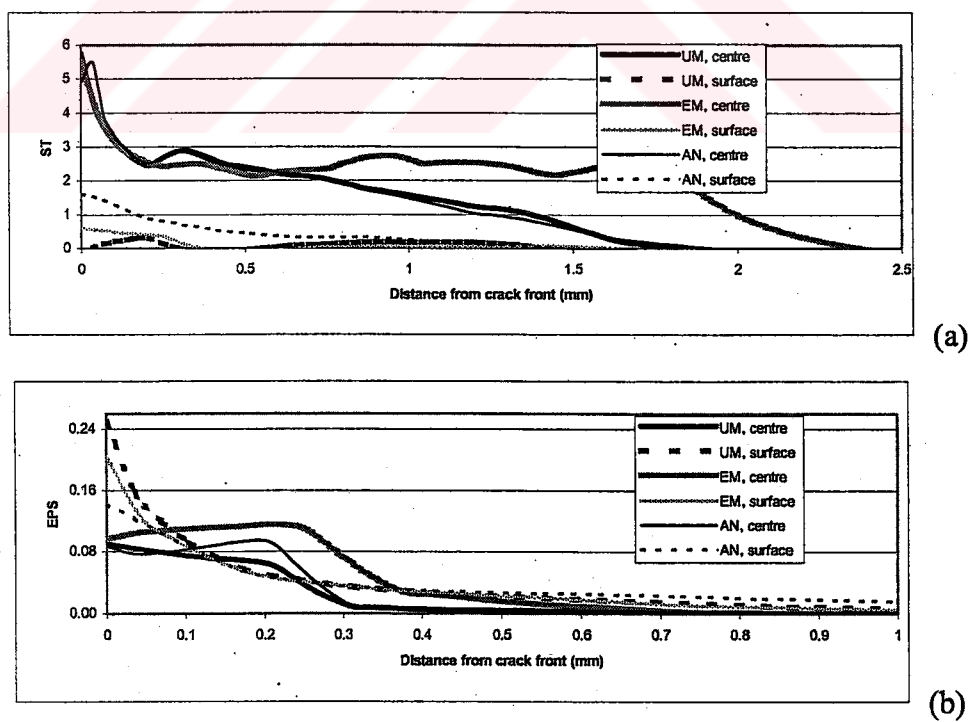


Figure 10.30. (a) Stress triaxiality, (b) equivalent plastic strain values along crack front in the centre and on the surface of the under-matched, annealed and even-matched models for 5.85 mm crack length on the location 3.

Figures from 10.31 to 10.40 represent the stress triaxiality and equivalent plastic strain values along y-axis and along crack front in the center and on the surface of the under-matched, annealed weldment and even-matched models for all crack lengths on the crack location 4. Number 0 indicates the crack tip. On this location, center part of the crack is in the base metal but surface part of the crack is in the weld metal for under-matched and annealed models. Crack location 4 is the nearest place to the base metal comparing with the other crack locations.

As seen from Figures 10.31a, 10.33a, 10.35a, 10.37a and 10.39a, maximum stress triaxiality occurs in the centers of the models for both under-matched and even-matched models. Stress triaxiality values on the surface (weld metal for under-matched and annealed models) are lower than that of in the center. Additionally, stress triaxiality values in the center and on the surface arise to the maximum level at the crack tip. As distinguished from Figures 10.31b, 10.33b, 10.35b, 10.37b and 10.39b, equivalent plastic strain values in the under-matched model are higher than that of in the even-matched model. For the under-matched model, the maximum equivalent plastic strain value occurs at crack tip on the surface part of crack. However, they reach the maximum level near the weld metal in the center part of the crack tip. This means that there is an extensive plastic deformation in a very small volume. On the contrary, there is a symmetric plastic deformation around crack tip in even-matched model.

Figures 10.32a, 10.34a, 10.36a, 10.38a and 10.40a depict the stress triaxiality values along crack front in the center and on the surface of the under-matched, annealed weld and even-matched models for all crack lengths. Maximum stress triaxiality occurs around crack tip for all models but stress triaxiality values on the surface are lower than that of in the center. As seen from Figures 10.32b, 10.34b, 10.36b, 10.38b and 10.40b, equivalent plastic strain values reach the maximum value at crack tip on the surface of the under-matched and annealed models. In the center, equivalent plastic strain values are lower than that of on the surface. These situations show that there is a hindrance to plastic deformation in the center because of the constraint at the crack tip.

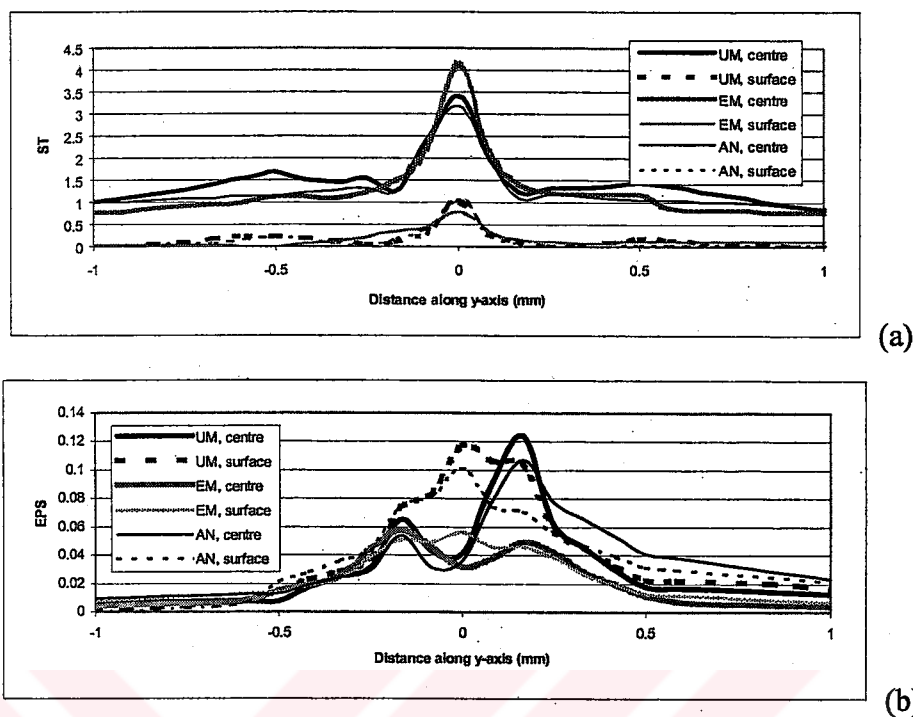


Figure 10.31. (a) Stress triaxiality, (b) equivalent plastic strain values along y axis around crack tip in the centre and on the surface of the under-matched, annealed and even-matched models for 5 mm crack length on the location 4.

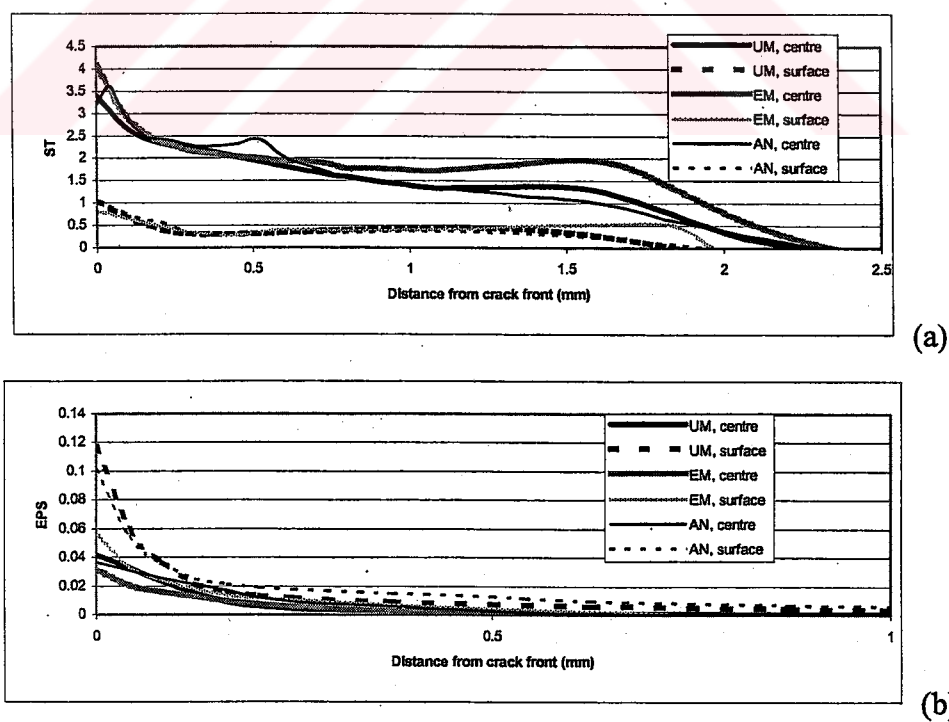


Figure 10.32. (a) Stress triaxiality, (b) equivalent plastic strain values along crack front in the centre and on the surface of the under-matched, annealed and even-matched models for 5 mm crack length on the location 4.

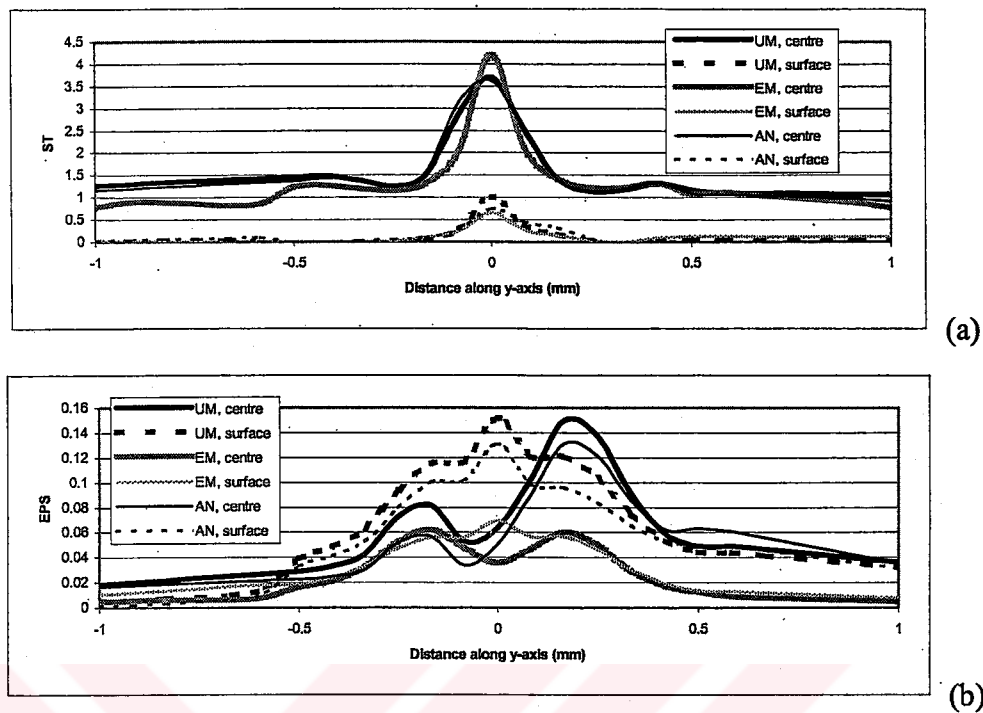


Figure 10.33. (a) Stress triaxiality, (b) equivalent plastic strain values along y axis around crack tip in the centre and on the surface of the under-matched, annealed and even-matched models for 5.05 mm crack length on the location 4.

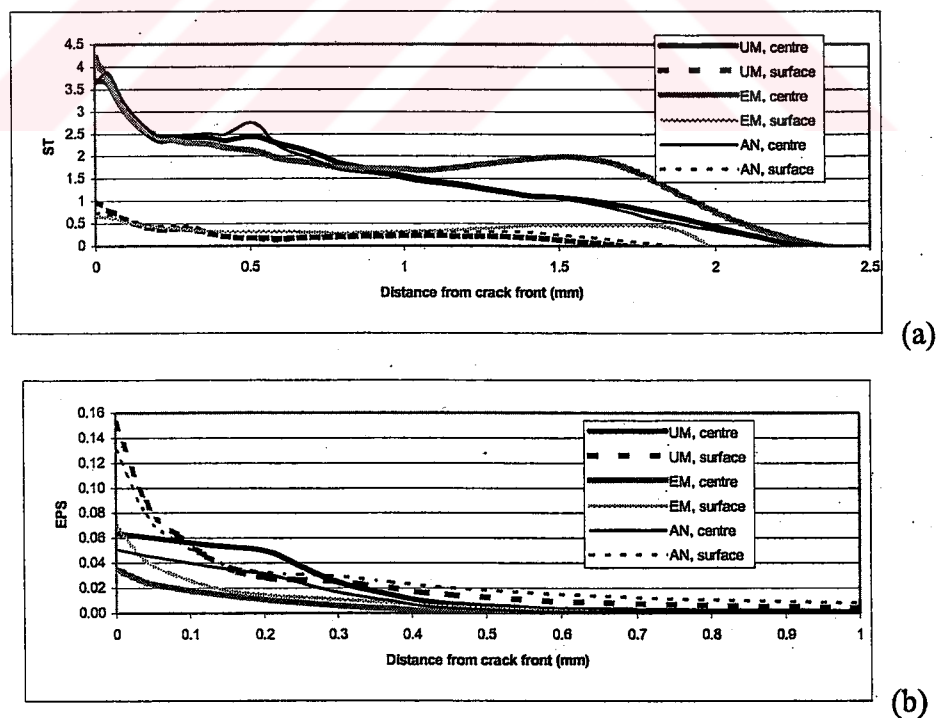


Figure 10.34. (a) Stress triaxiality, (b) equivalent plastic strain values along crack front in the centre and on the surface of the under-matched, annealed and even-matched models for 5.05 mm crack length on the location 4.

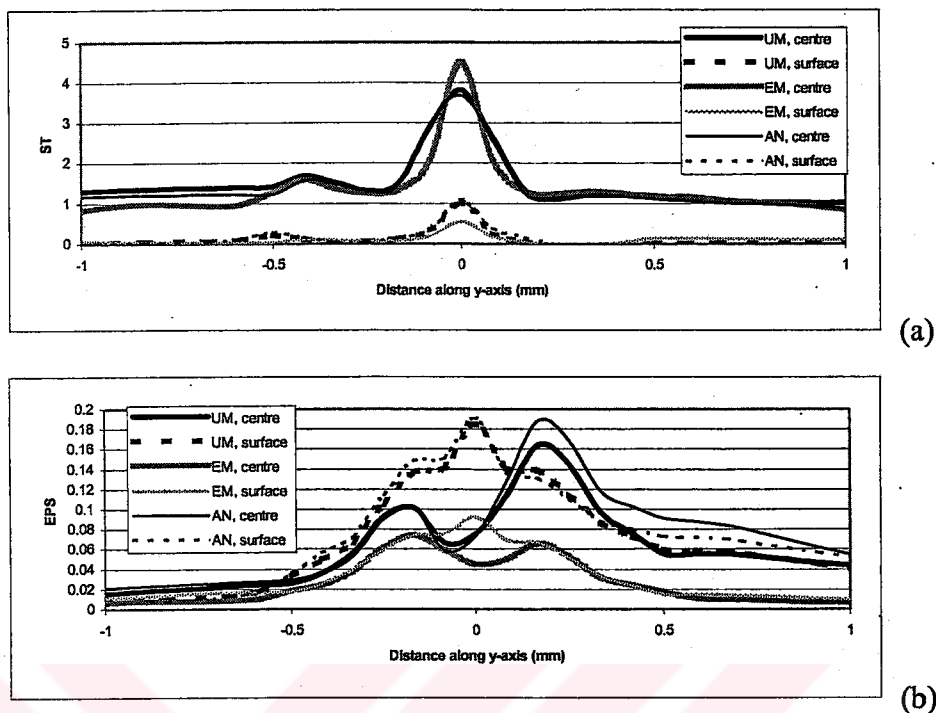


Figure 10.35. (a) Stress triaxiality, (b) equivalent plastic strain values along y axis around crack tip in the centre and on the surface of the under-matched, annealed and even-matched models for 5.1 mm crack length on the location 4.

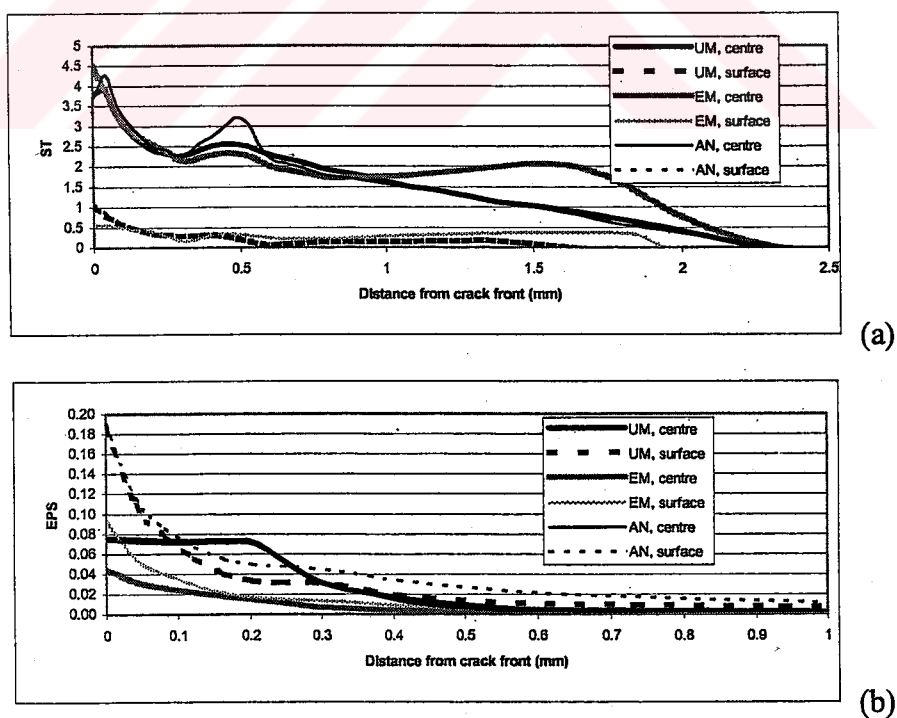
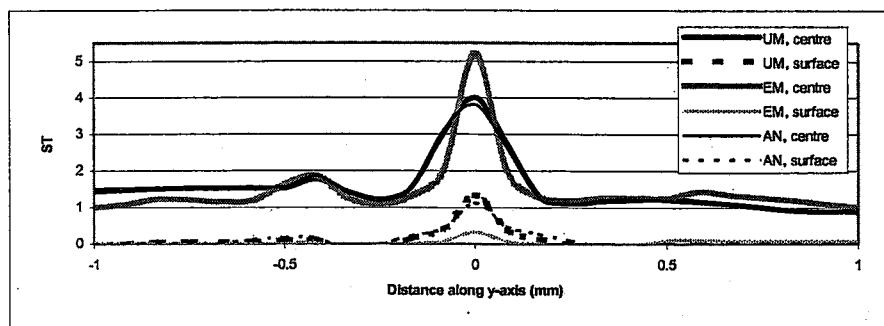
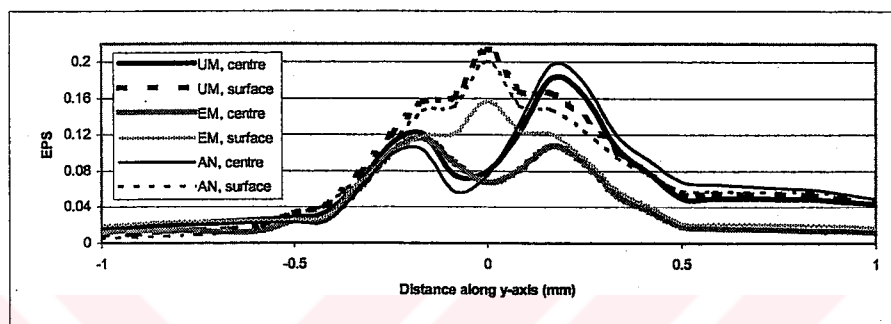


Figure 10.36. (a) Stress triaxiality, (b) equivalent plastic strain values along crack front in the centre and on the surface of the under-matched, annealed and even-matched models for 5.1 mm crack length on the location 4.

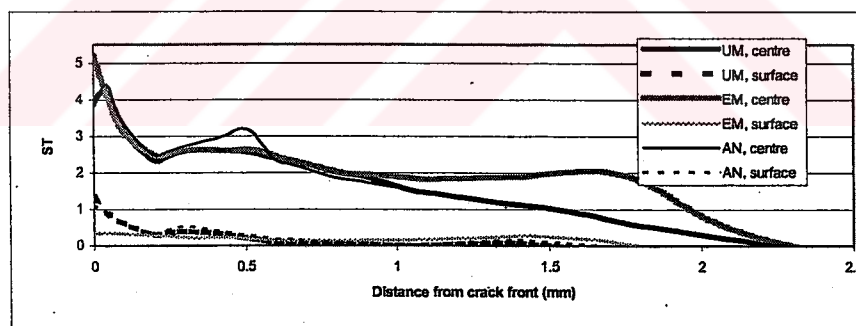


(a)

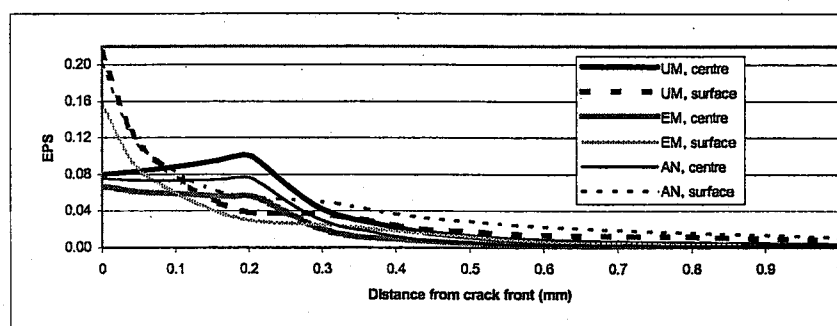


(b)

Figure 10.37. (a) Stress triaxiality, (b) equivalent plastic strain values along y axis around crack tip in the centre and on the surface of the under-matched, annealed and even-matched models for 5.2 mm crack length on the location 4.



(a)



(b)

Figure 10.38. (a) Stress triaxiality, (b) equivalent plastic strain values along crack front in the centre and on the surface of the under-matched, annealed and even-matched models for 5.2 mm crack length on the location 4.

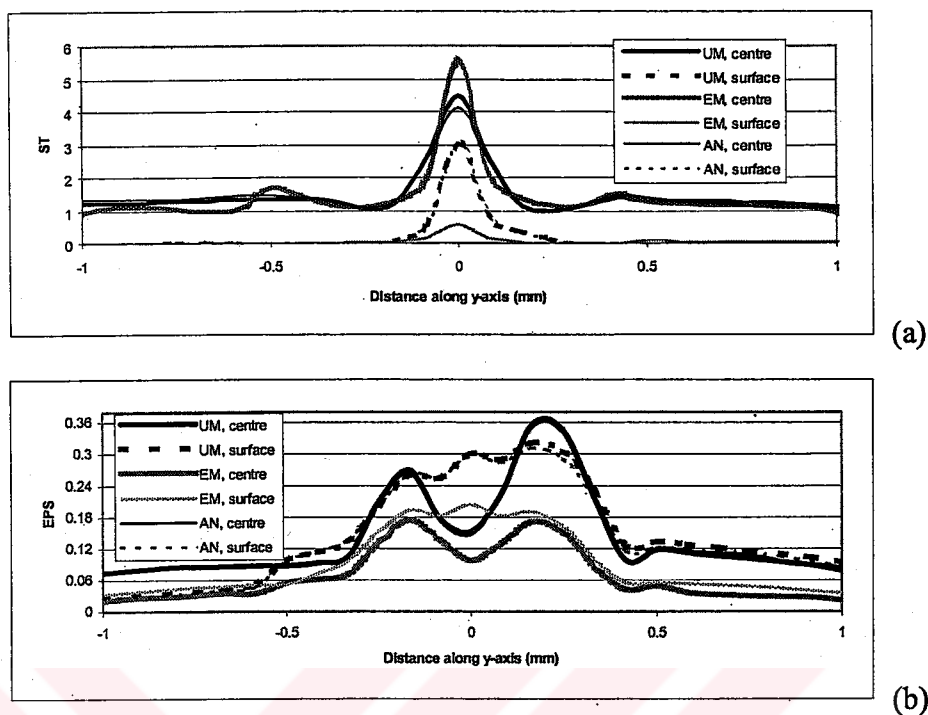


Figure 10.39. (a) Stress triaxiality, (b) equivalent plastic strain values along y axis around crack tip in the centre and on the surface of the under-matched, annealed and even-matched models for 5.85 mm crack length on the location 4.

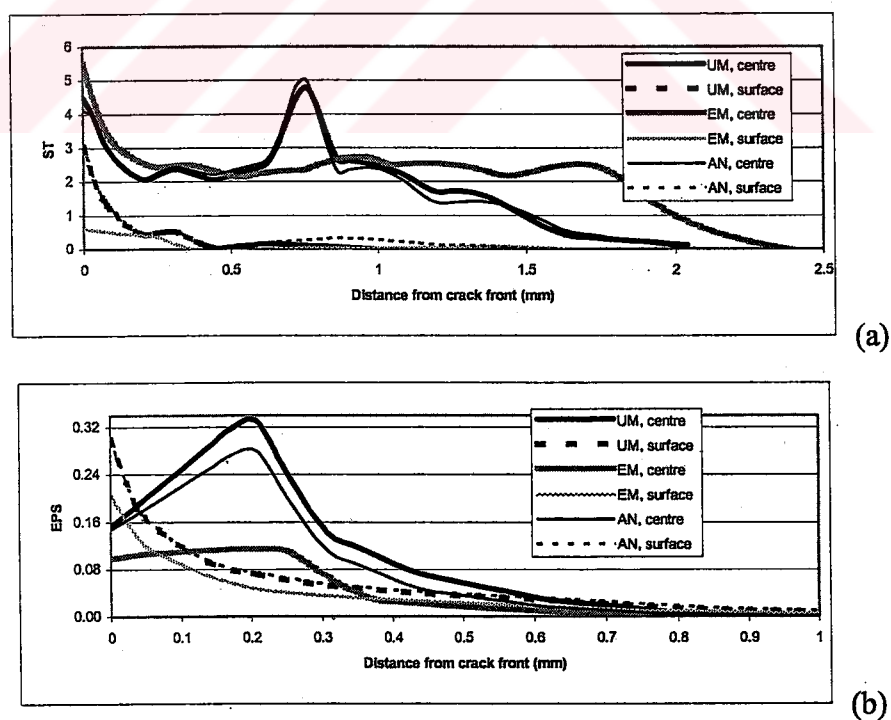


Figure 10.40. (a) Stress triaxiality, (b) equivalent plastic strain values along crack front in the centre and on the surface of the under-matched, annealed and even-matched models for 5.85 mm crack length on the location 4.

Figures 10.41, 10.42, 10.43 and 10.44 show the variation of stress triaxiality values at 0.01 mm away from the crack front in the center of under-matched, annealed and even-matched specimens for the crack locations 1, 2, 3 and 4. Annealed models have the minimum stress triaxiality values for all crack lengths but even-matched models have the maximum stress triaxiality values for these crack lengths. Stress triaxiality values of under-matched models are between that of annealed and even-matched models. In the crack location 1, stress triaxiality values occurred at 0.01 mm ahead of the crack front in the center of even-matched model are distinctive than that of under-matched and annealed models. Stress triaxiality values increase with increasing crack lengths. Annealing treatment does not decrease stress triaxiality values significantly. In the crack location 2, difference in stress triaxiality values of the models are not significant but even-matched models have slightly higher stress triaxiality values. The same situation can be seen on the crack location 3. As can be seen in Figure 10.44, there is a significant difference in stress triaxiality values among even-matched and other models. In longer crack lengths, stress triaxiality values increase for all models. This is important to make a conclusion on fracture resistance capability of the models: decrease in triaxial stress state at crack tip may lead to increasing the fracture resistance capability (Tong, W & Shi, Y.W., 1995).

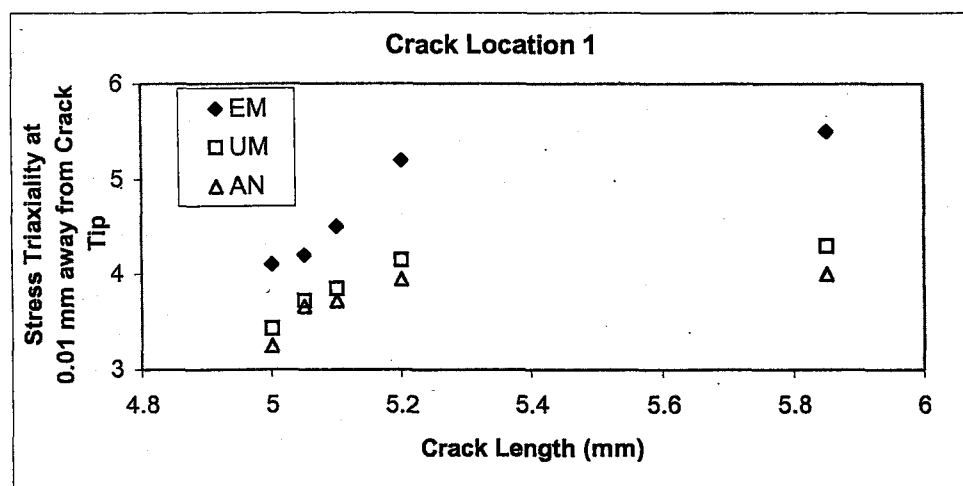


Figure 10.41. The results of stress triaxiality values at 0.01 mm away from the crack tip vs. crack lengths in the center of the under-matched, annealed and even-matched specimens for the crack location 1.

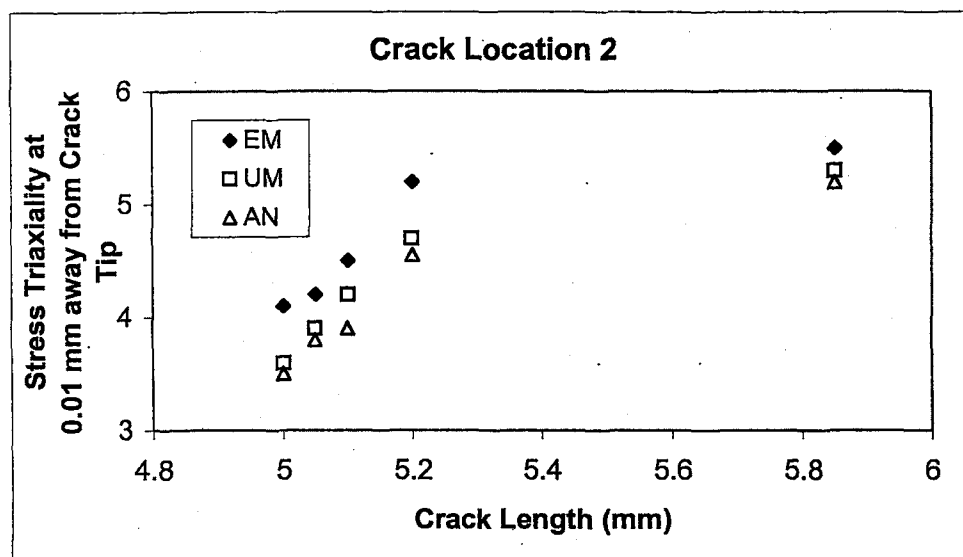


Figure 10.42. The results of stress triaxiality values at 0.01 mm away from the crack tip vs. crack lengths in the center of the under-matched, annealed and even-matched specimens for the crack location 2.

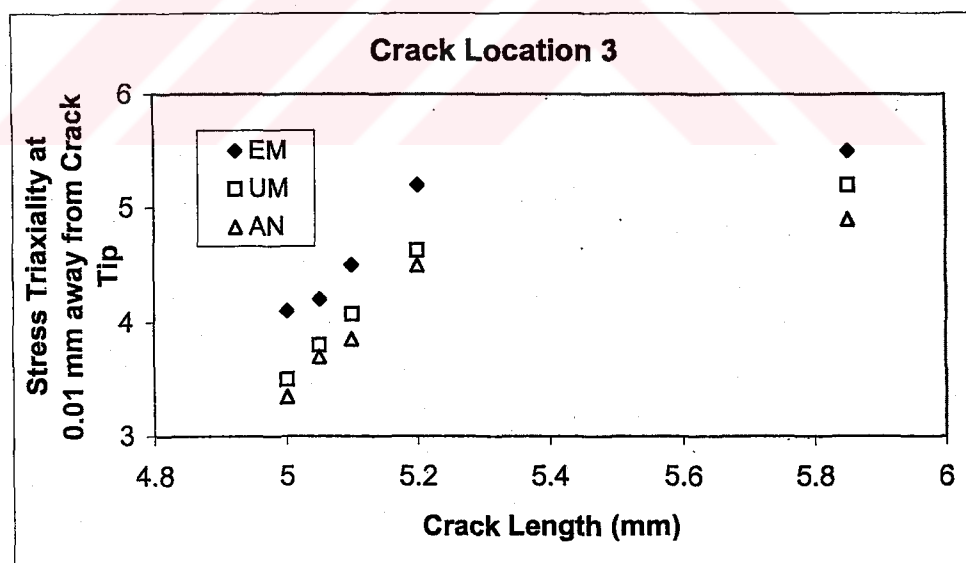


Figure 10.43. The results of stress triaxiality values at 0.01 mm away from the crack tip vs. crack lengths in the center of the under-matched, annealed and even-matched specimens for the crack location 3.

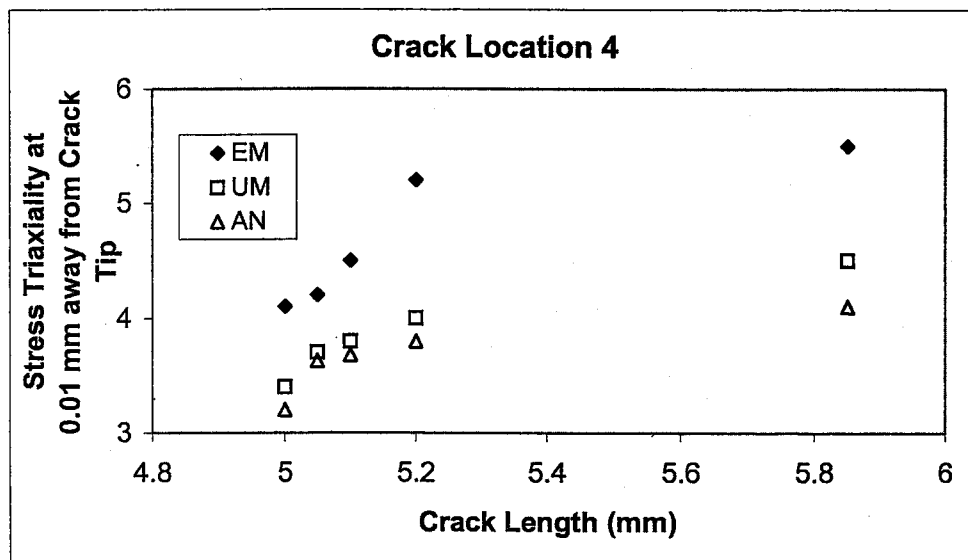


Figure 10.44. The results of stress triaxiality values at 0.01 mm away from the crack tip vs. crack lengths in the center of the under-matched, annealed and even-matched specimens for the crack location 4.

Figures 10.45a and 10.45b depict the variation of stress triaxiality values by crack length at 0.01mm away from the crack tip in the center of the even-matched, under-matched and annealed models comparing with even-matched specimens for different crack locations. As seen from Figure 10.45a, even-matched models have the higher stress triaxiality values for all crack lengths. In under-matched models with different crack lengths on different crack locations, higher stress triaxiality values occur on the crack location 2 placed between base metal and weld metal, because this crack location is the nearest one to HAZ where plastic strain flow confined. This hindrance more effective than that of other crack locations. In location 4, There is a small volume between the crack tip and HAZ region. Lower stress triaxiality values take place on the location 4 for shorter crack lengths but this situation changes with growing crack length and the lowest stress triaxiality values occur on the crack location 1. Figure 10.45b shows the similar situation for annealed models. Lower stress triaxiality values occur in annealed models for all crack locations than that of even-matched models. On locations 2 and 3, higher stress triaxiality values take place than that of locations 1 and 4. In shorter crack lengths, stress triaxiality values

on location 4 are lower than that of location 1. This situation changes with the growing crack length for crack locations 1 and 4.

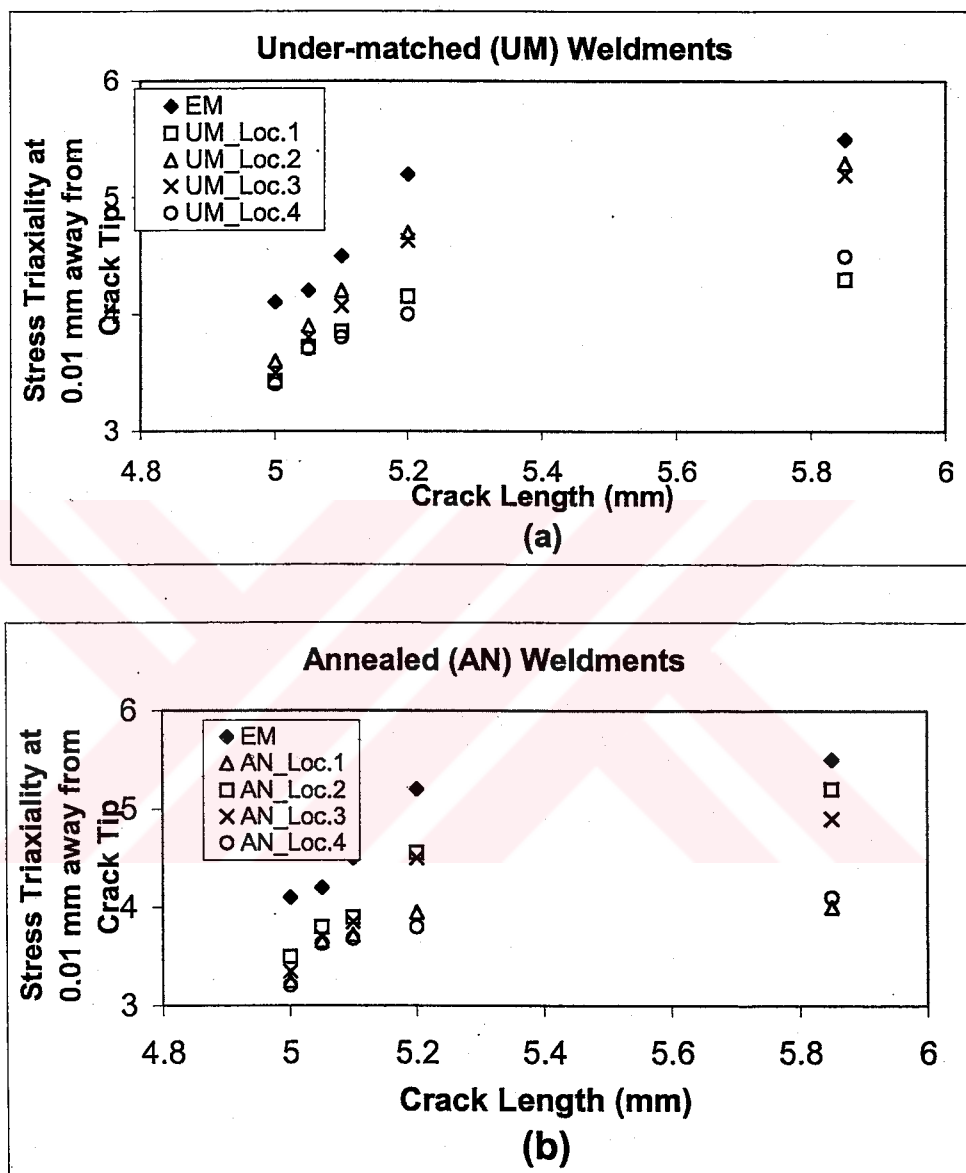


Figure 10.45. The results of stress triaxiality values at 0.01 mm away from the crack tip vs. crack lengths in the center of the (a) under-matched (b) annealed specimens comparing with even-matched specimens for the all crack locations.

Increase in stress triaxiality values with crack length arises from different regions with various work hardening exponents. Strengths of different regions increase by plastic deformation or crack growth. This increase is higher in the HAZ than that of

the base metal and the weld metal. Thus, mismatch between HAZ and other regions increases by deformation, so constraint at crack tip increase by plastic deformation or crack growth.

Figures 10.46, 10.47, 10.48 and 10.49 show the results of equivalent plastic strain values at 0.01 mm from the crack tip versus crack lengths in the center of the under-matched, annealed and even-matched specimens for the all crack locations. In Figure 10.46, it is seen that equivalent plastic strain values occurred in the under-matched and annealed models are higher than that of even-matched models. Difference in the equivalent plastic strain values increases with increasing crack length. Similar situation can be seen in the crack location 2 (Figure 10.47). Equivalent plastic strain values increase extensively in the highest crack lengths for under-matched and annealed models. In location 3, there is no significant difference in equivalent plastic strain values of the all models. In small crack lengths, annealed models have the higher equivalent plastic strain values. As can be seen in Figure 10.49, there is no significant difference in equivalent plastic strain values of under-matched and annealed models on crack location 4 but these values are higher than that of even-matched models especially for the longest crack length.

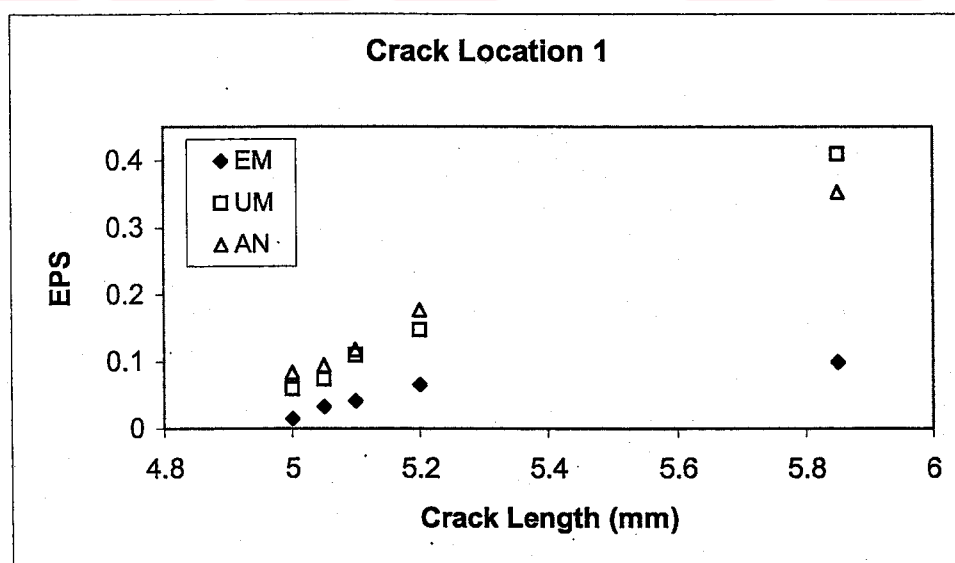


Figure 10.46. The results of equivalent plastic strain values at 0.01 mm away from the crack tip vs. crack lengths in the center of the under-matched, annealed and even-matched specimens for the crack location 1.

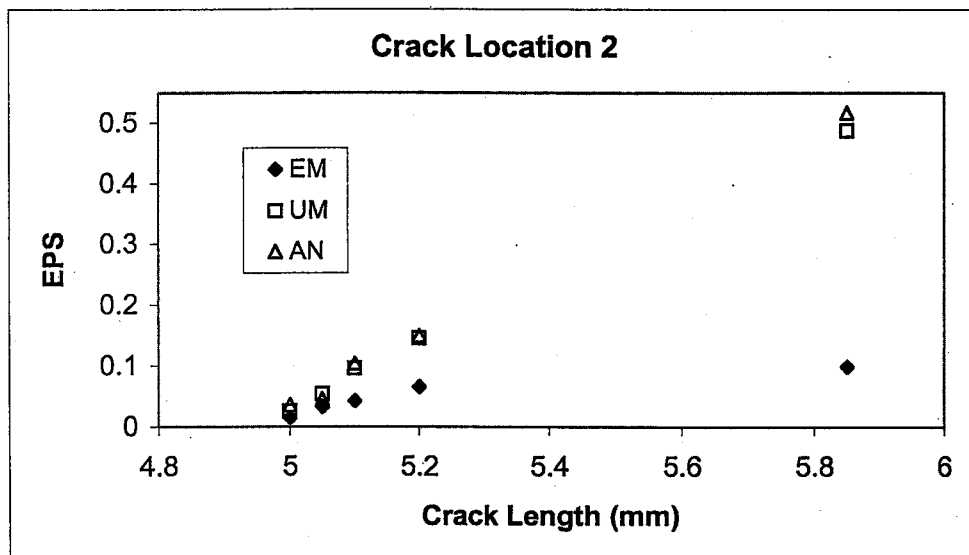


Figure 10.47. The results of equivalent plastic strain values at 0.01 mm away from the crack tip vs. crack lengths in the center of the under-matched, annealed and even-matched specimens for the crack location 2.

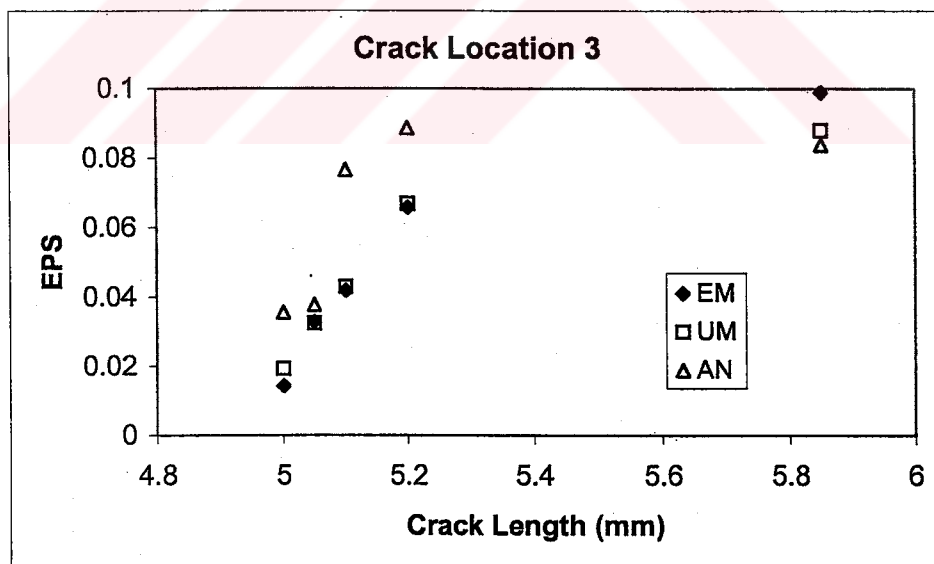


Figure 10.48. The results of equivalent plastic strain values at 0.01 mm away from the crack tip vs. crack lengths in the center of the under-matched, annealed and even-matched specimens for the crack location 3.

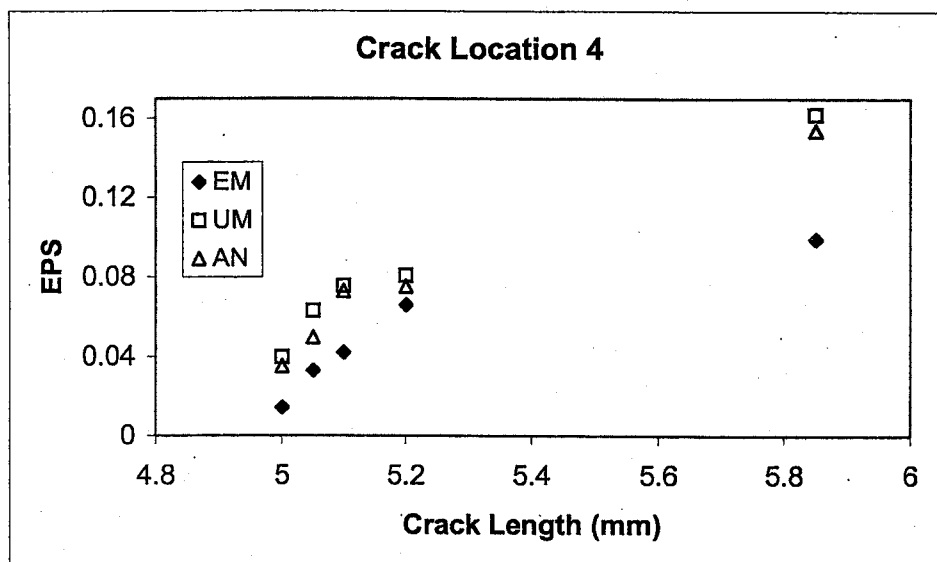


Figure 10.49. The results of equivalent plastic strain values at 0.01 mm away from the crack tip vs. crack lengths in the center of the under-matched, annealed and even-matched specimens for the crack location 4.

Figures 10.50a and 10.50b depict the variation of equivalent plastic strain values with crack length at 0.01mm ahead of crack tip in the center of the even-matched, under-matched and annealed models for different crack locations. As seen from Figure 10.50a, for shorter crack lengths, there is no significant difference in equivalent plastic strain values among even-matched and under-matched models including all crack locations but with increasing crack length, equivalent plastic strain values in crack locations 1 and 2 on under-matched models get higher than that of even-matched models and under-matched models with cracks in other location. In Figure 10.50b, the same situation can be observed for annealed models. There is no significant difference in equivalent plastic strain values for shorter crack lengths. Equivalent plastic strain values get lower with increasing crack length for location 3 and 4 on annealed and even-matched models. The increase in plastic deformation at crack tip reduces the stress triaxiality. Plastic deformation at crack tip may be exhausted if increase in equivalent plastic strain becomes extensive due to the lack of extension into the material. In even-matched models, this equivalent plastic strain values do not change significantly. Equivalent plastic strain distribution in the material is also important concept and it must be discussed.

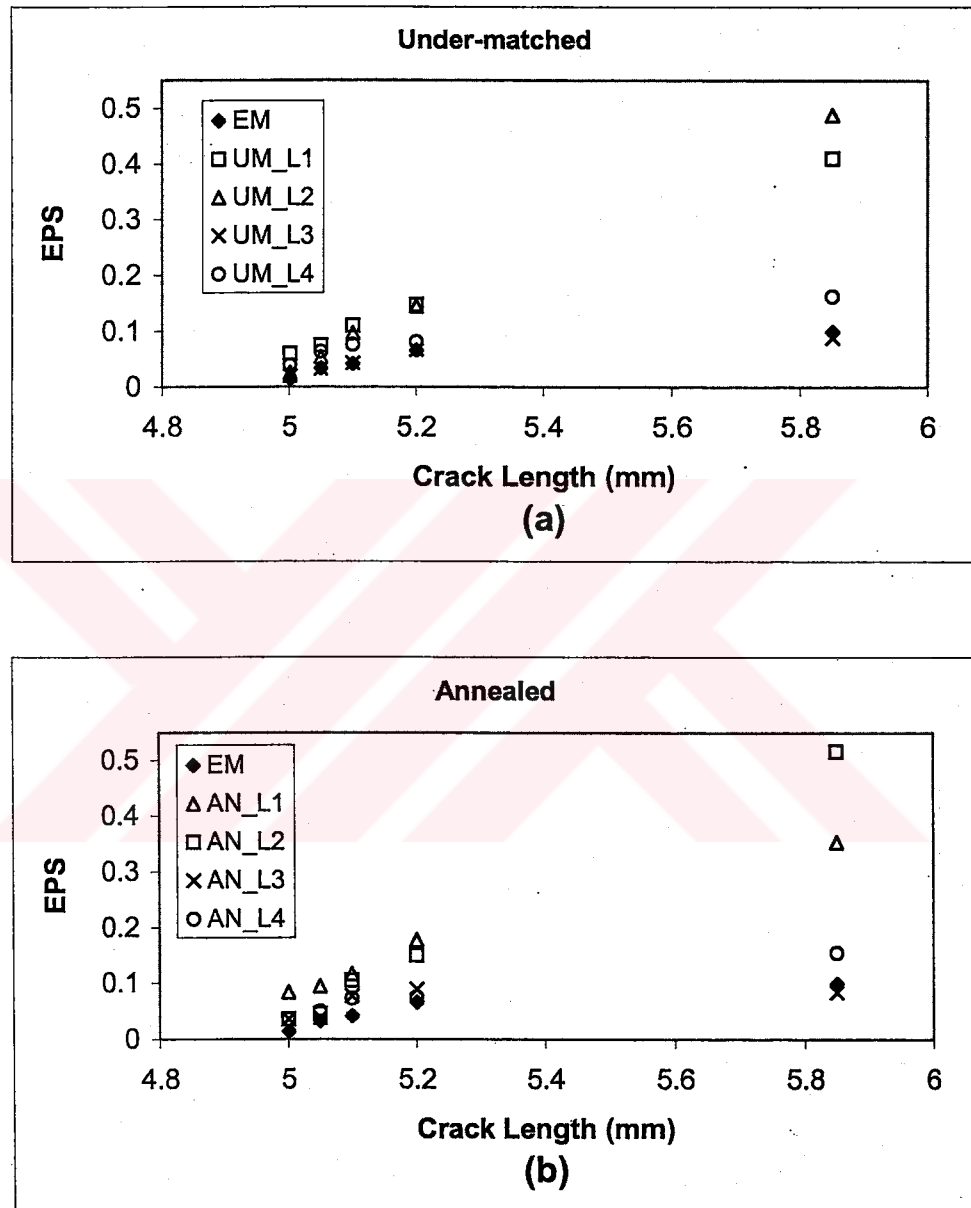


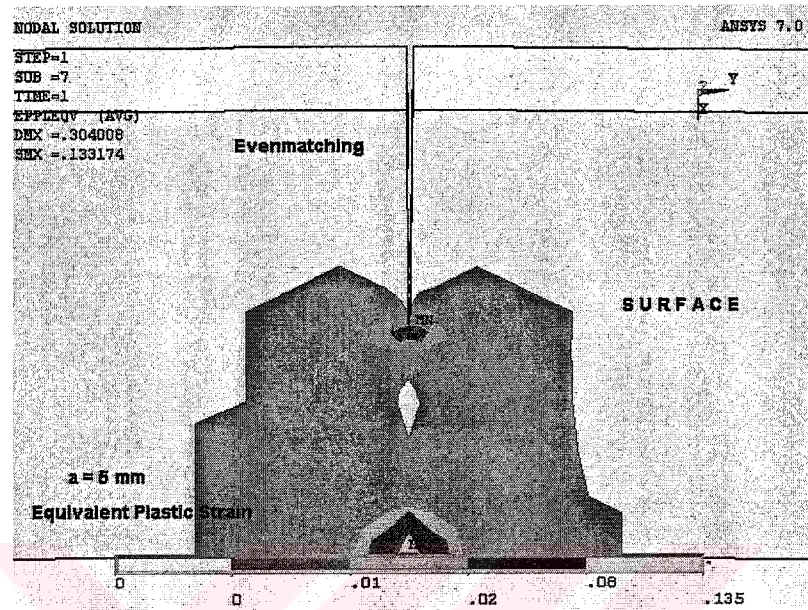
Figure 10.50. The results of equivalent plastic strain values at 0.01 mm away from the crack tip vs. crack lengths in the center of the (a) under-matched (b) annealed specimens comparing with even-matched specimens for the all crack locations.

10.2. Equivalent Plastic Strain Distribution on the Models

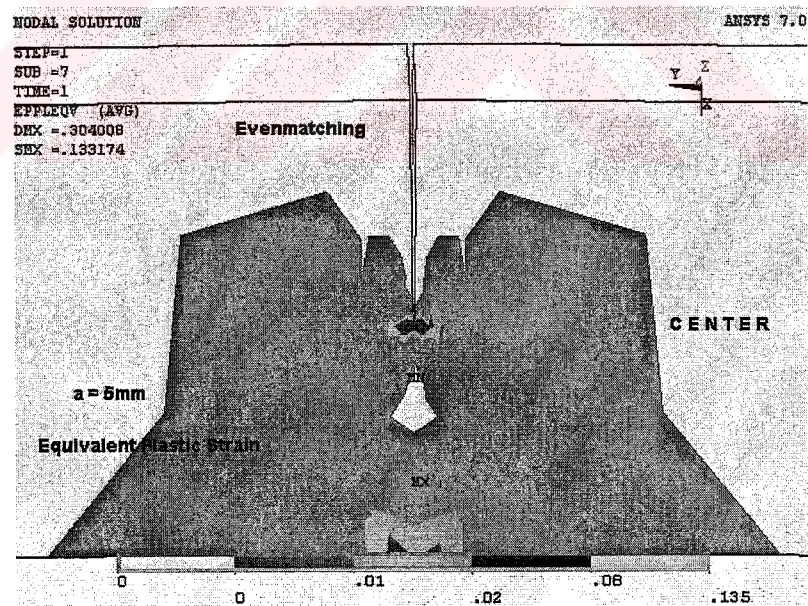
Appearance of the plastic zone behind the crack tip may change the stress state ahead of the crack tip. This result in reduce its triaxiality, so it is important that these zones must be examined carefully. Figures from 10.51 to 10.68 depict the equivalent plastic strain extension on the surface and in the center of the even-matched, under-matched and annealed models for 5 mm and 5.85 mm crack lengths on the different crack locations.

10.2.1. Even-Matched Models

Figure 10.51 and 10.52 show the equivalent plastic strain distribution on the surface (Figures 10.51a and 10.52a) and center (Figures 10.51b and 10.52b) of the even-matched models for 5 mm and 5.85 mm crack lengths. As can be seen in these Figures, net section yielding occurs in the models and there is no extensive difference in equivalent plastic strain values between center and surface of the models. For higher crack length, the amount of plastic deformation increases but there is no significant difference in plastic zone size. Extension of plastic deformation decreases the constraint at crack tip. In higher crack length, extension cannot observed, so constraint increases significantly by growing crack length.

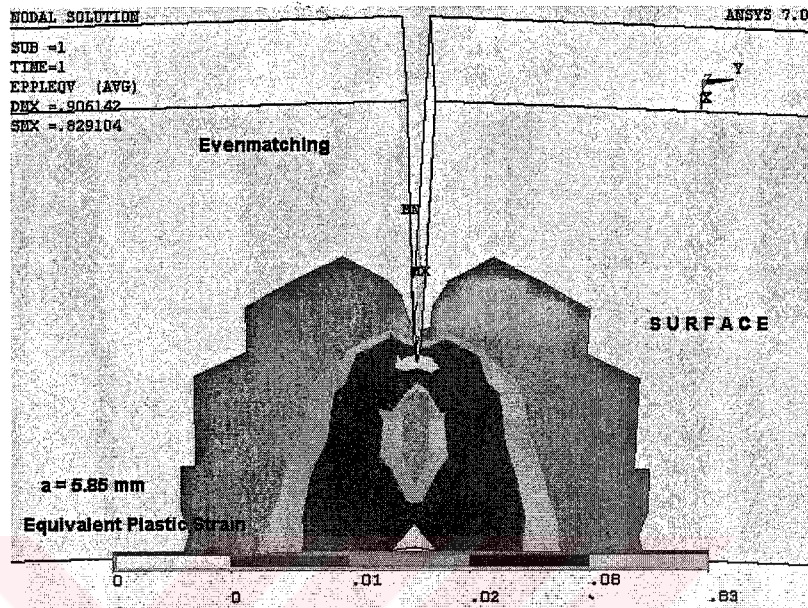


(a)

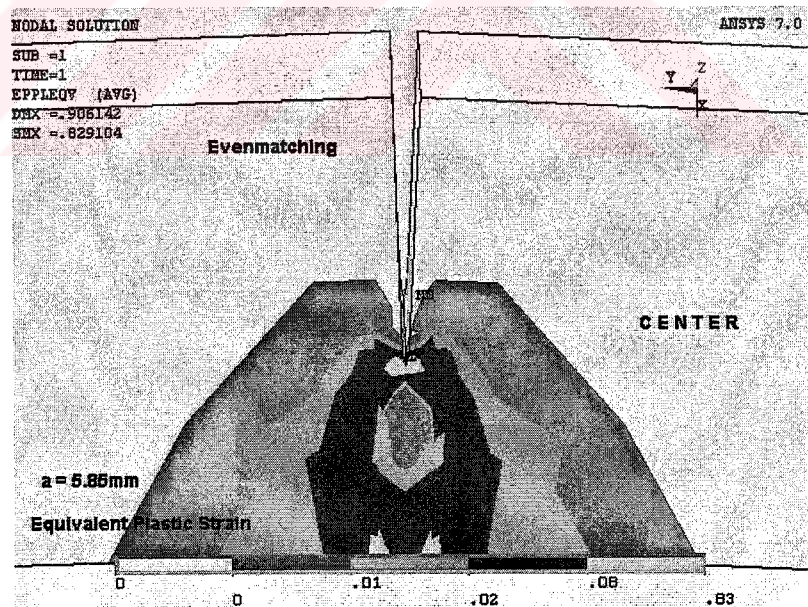


(b)

Figure 10.51. Equivalent plastic strain distribution (a) on the surface and (b) in the center of the even-matched model for 5 mm crack length.



(a)



(b)

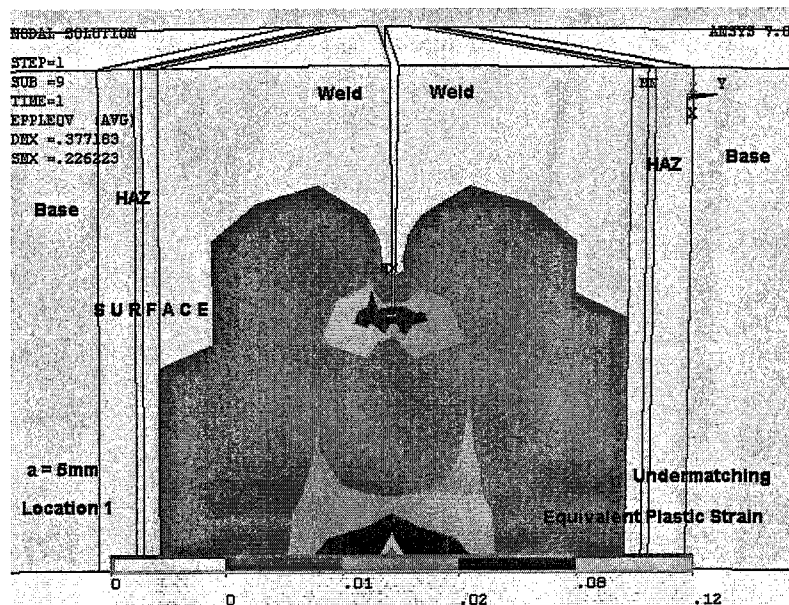
Figure 10.52. Equivalent plastic strain distribution (a) on the surface and (b) in the center of the even-matched model for 5.85 mm crack length.

10.2.2. Under-matched Models

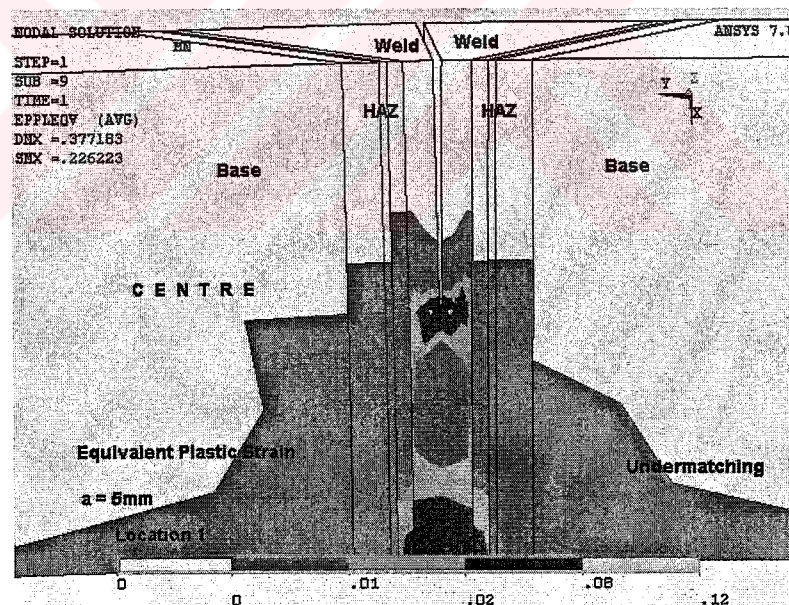
Figures from 10.53 to 10.60 indicate the equivalent plastic strain distribution on the surface and in the center of the under-matched models for 5 mm and 5.85 mm crack lengths on the different crack locations. The effect of the regions with different yield strengths on plastic deformation can be seen in these figures. In over-matched weldments, plastic deformation develops not only in the crack tip but also across HAZ into the base metal starting from an early stage of global loading. The early development of plastic deformation in the base metal leads to relaxation of the crack tip loading. In under-matched weldments, this situation is not valid. Plastic deformation is limited by HAZ. Thus, constraint causes extra triaxial stresses at crack tip.

In Figures 10.53 and 10.54, equivalent plastic strain extension on the models can be observed for crack location 1 with 5 mm and 5.85 mm crack lengths. Crack location is in the weld metal. There is a net section yielding over un-cracked ligament. On the surfaces of the models, plastic strain cannot enter the HAZ. This situation is valid for both the shortest and the longest crack lengths (Figures 10.53a and 10.54a). In the center, plastic strain passes the HAZ but there is discontinuation in plastic flow lines (Figures 10.53b and 10.54b). In higher crack lengths, distribution of plastic strain is obstructed by HAZ. As we know, HAZ higher work hardening exponent, so its effect on hindrance becomes more significant. As a result, plastic deformation is forced to stay in weld metal, so stress triaxiality at crack tip increases.

Figures 10.55 and 10.56 show the equivalent plastic strain distribution on the surface and in the center of under-matched models with 5 mm and 5.85 mm crack lengths on the crack location 2 where is between HAZ and weld metal. On the surfaces of the models with 5 mm and 5.85 mm crack lengths, plastic strain cannot across the HAZ but plastic strain passes this region with discontinuous plastic flow lines in the center of the models. Plastic strain intends to flow into weld metal because weld metal is softer than HAZ and base metal, so bending character forces plastic strain to flow into weld metal.

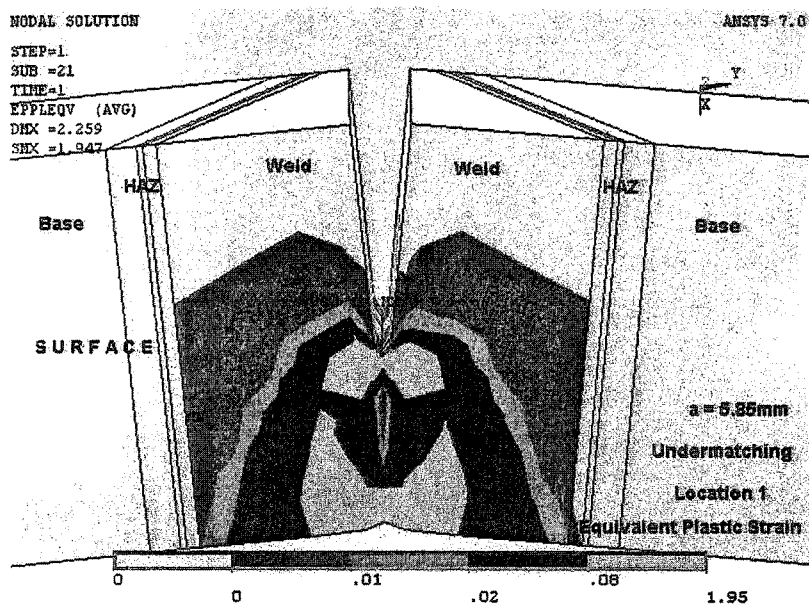


(a)

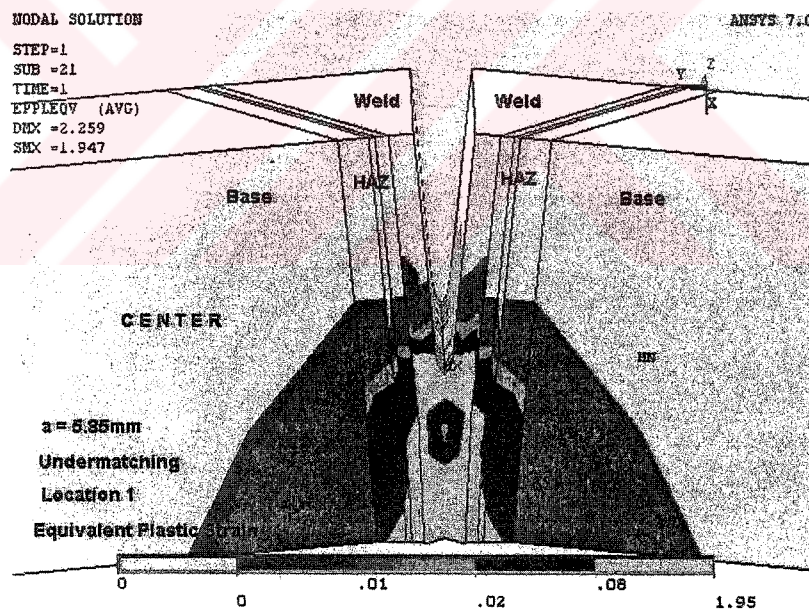


(b)

Figure 10.53. Equivalent plastic strain distribution (a) on the surface and (b) in the center of the under-matched model for 5 mm crack length in the crack location 1.

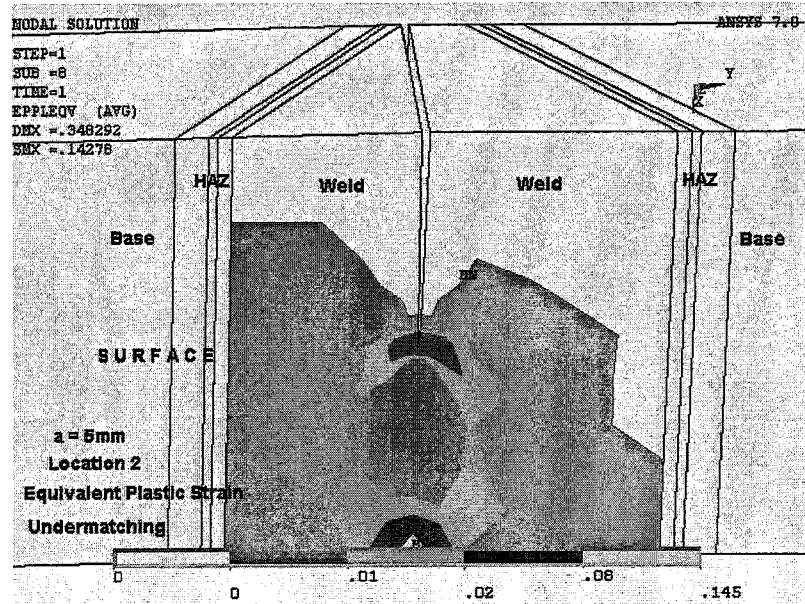


(a)

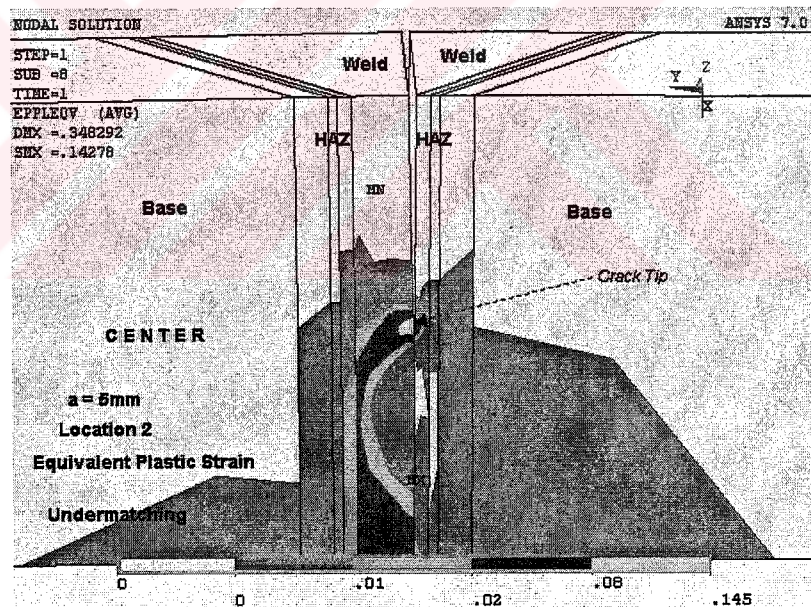


(b)

Figure 10.54. Equivalent plastic strain distribution (a) on the surface and (b) in the center of the under-matched for 5.85 mm crack length model in the crack location 1.

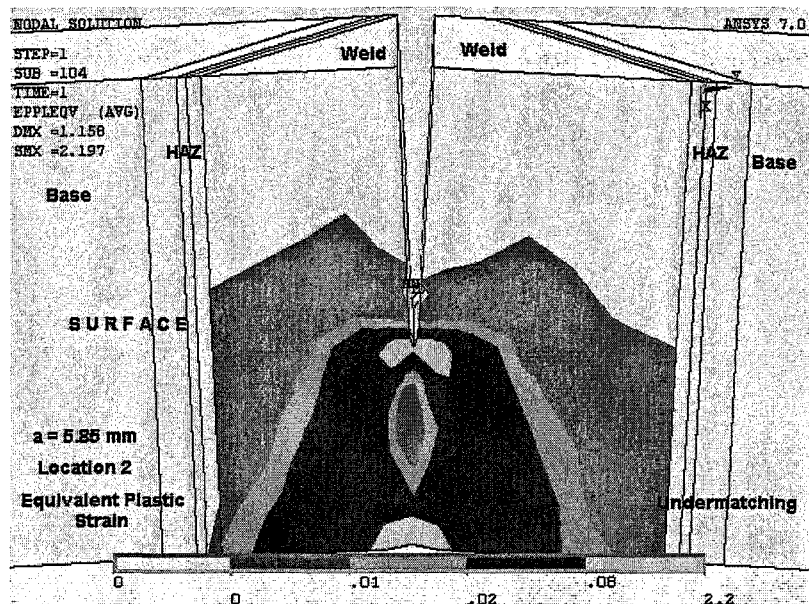


(a)

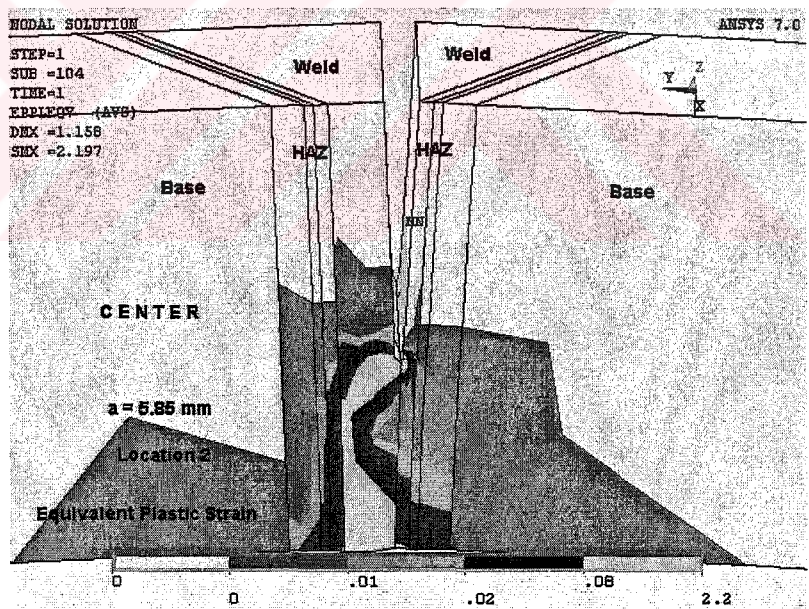


(b)

Figure 10.55. Equivalent plastic strain distribution (a) on the surface and (b) in the center of the under-matched for 5 mm crack length model in the crack location 2.



(a)

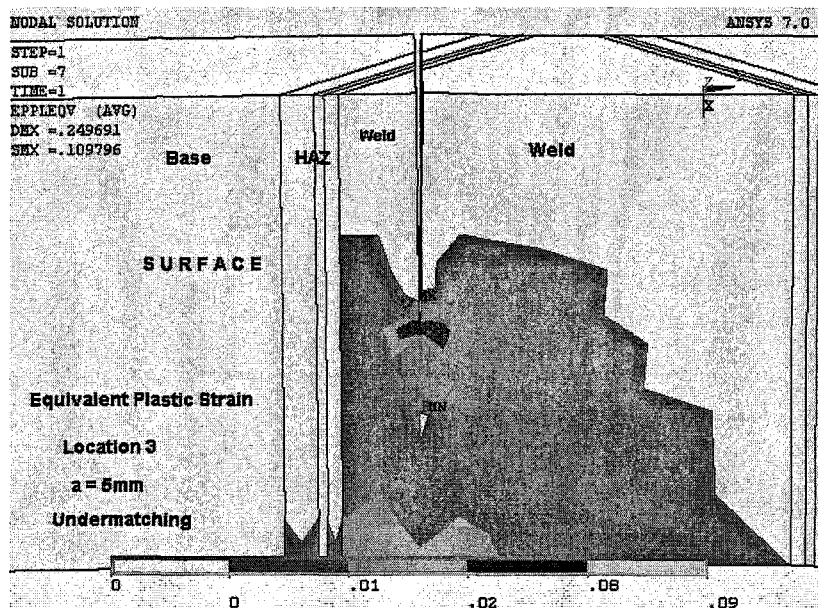


(b)

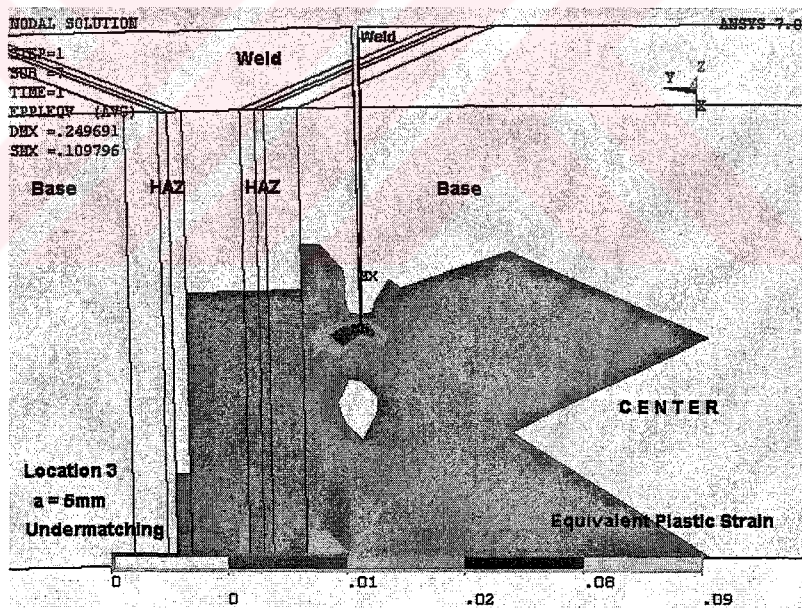
Figure 10.56. Equivalent plastic strain distribution (a) on the surface and (b) in the center of the under-matched model for 5.85 mm crack length in the crack location 2.

In Figures 10.57 and 10.58, equivalent plastic strain extension on the surface and in the center of the under-matched models with 5 mm and 5.85 mm crack lengths on the crack location 3 can be seen. Cracks pass through the base metal, weld metal and HAZ. On the surface of the models, plastic strain does not cross the HAZ and so spread into the weld metal for 5 mm crack length, but in the center, plastic strain crosses the HAZ (Figures 10.57a and 10.57b). On the surface of the model with 5.85 mm crack length, plastic strain passes the HAZ, but their higher values are detained in the weld metal (Figure 10.58a). This situation arises the stress triaxiality at crack tip due to extra constraint. On the other hand, different situation takes place in the center of the model. In Figure 10.58b, plastic strain intends to pass the HAZ rather than spreading into base metal because of the bending character of the bar. Difficulties in plastic strain passing through the HAZ cause extra constraint.

Figures 10.59 and 10.60 depict the equivalent plastic strain distribution on the surface and in the center of under-matched models with 5 mm and 5.85 mm crack lengths on the location 4. In this location, cracks cut the base metal, weld metal and HAZ. On the surface of the model with 5 mm crack length, plastic strain crosses the HAZ and spread into the base metal but its higher values are detained in the weld metal. Similar situation takes place in the center of the model but plastic strain flows into base metal (Figures 10.59a and 10.59b). On the other hand, plastic strain crosses the HAZ on the surface and in the center of the model with 5.85 mm crack length. Plastic flow lines appear discontinuous (Figures 10.60a and 10.60b). In Figure 10.60b, HAZ plays an important role in obstruction plastic strain. Only small amount of plastic strain enter the HAZ. Thus, this constraint arises the triaxial stresses at crack tip.

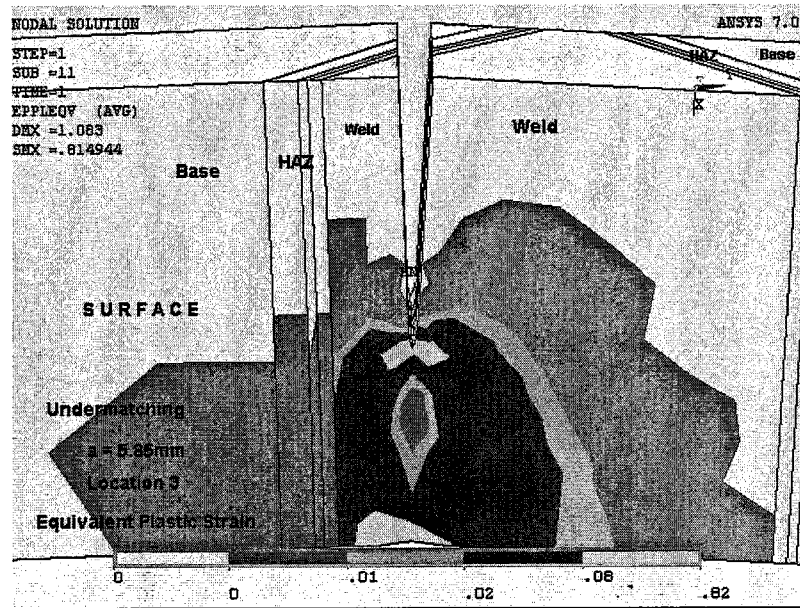


(a)

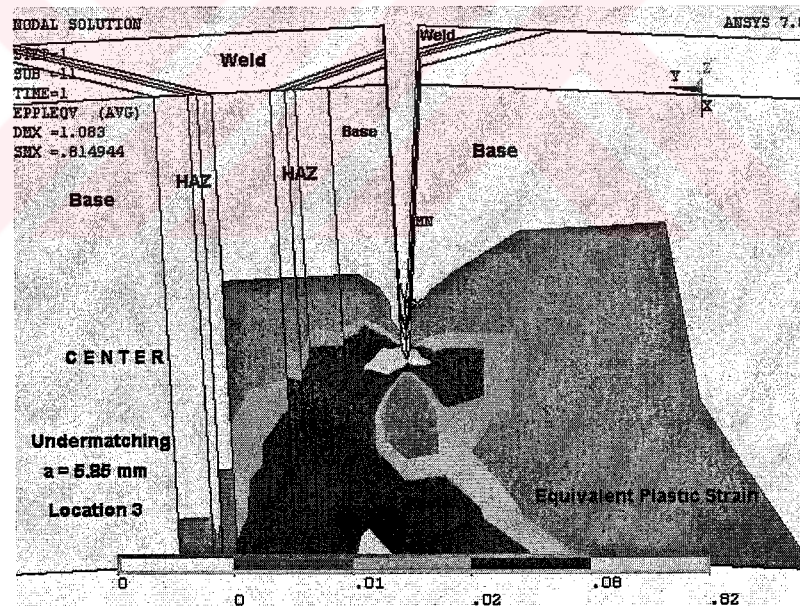


(b)

Figure 10.57. Equivalent plastic strain distribution (a) on the surface and (b) in the center of the under-matched model for 5 mm crack length in the crack location 3.

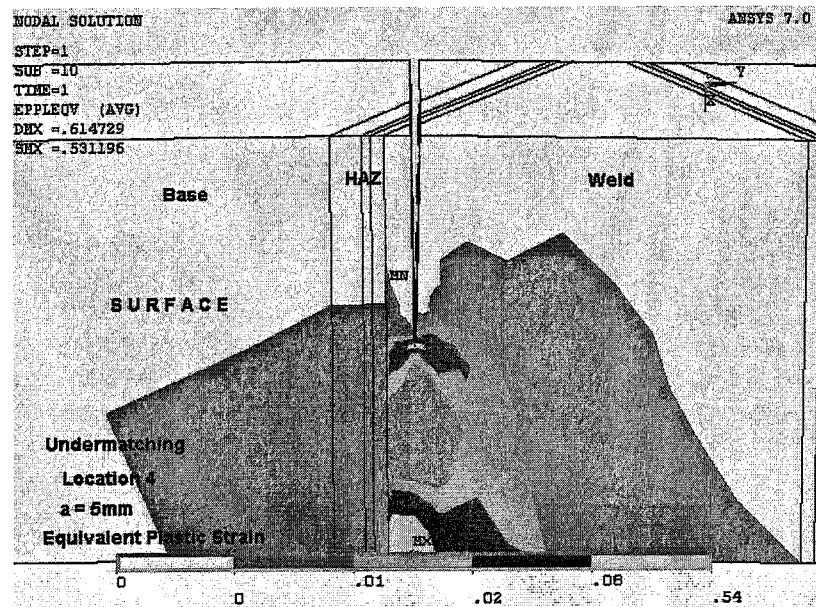


(a)

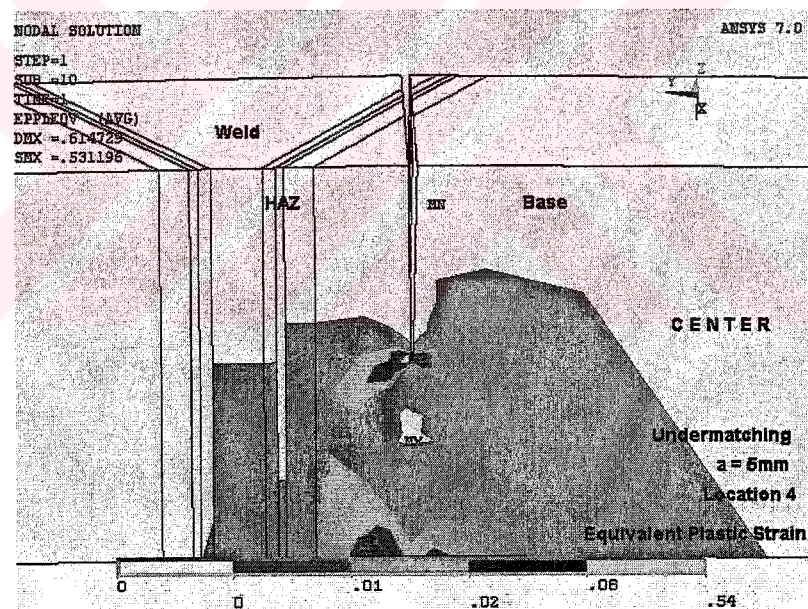


(b)

Figure 10.58. Equivalent plastic strain distribution (a) on the surface and (b) in the center of the under-matched model for 5.85 mm crack length in the crack location 3.

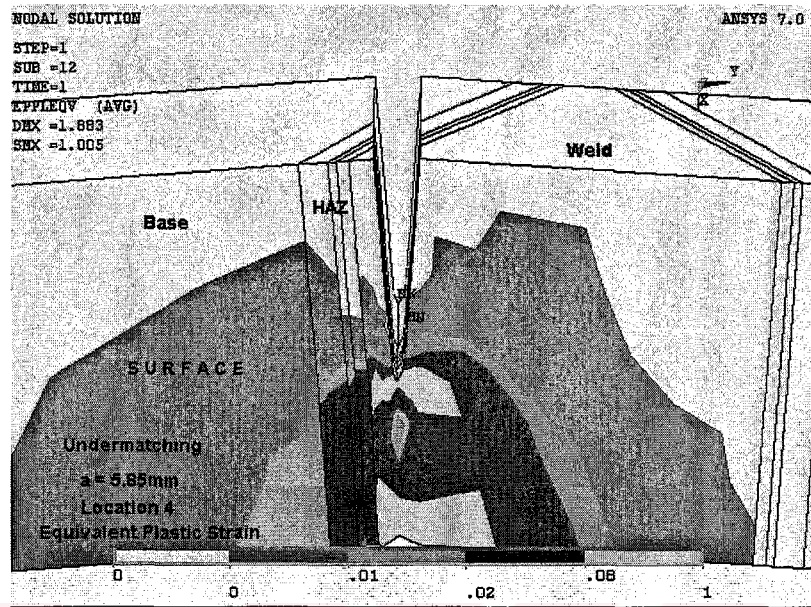


(a)

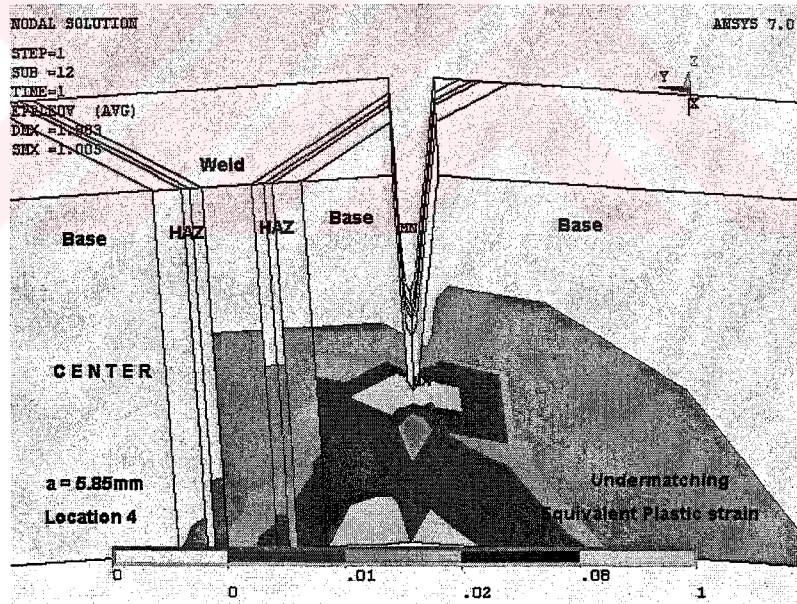


(b)

Figure 10.59. Equivalent plastic strain distribution (a) on the surface and (b) in the center of the under-matched model for 5 mm crack length in the crack location 4.



(a)



(b)

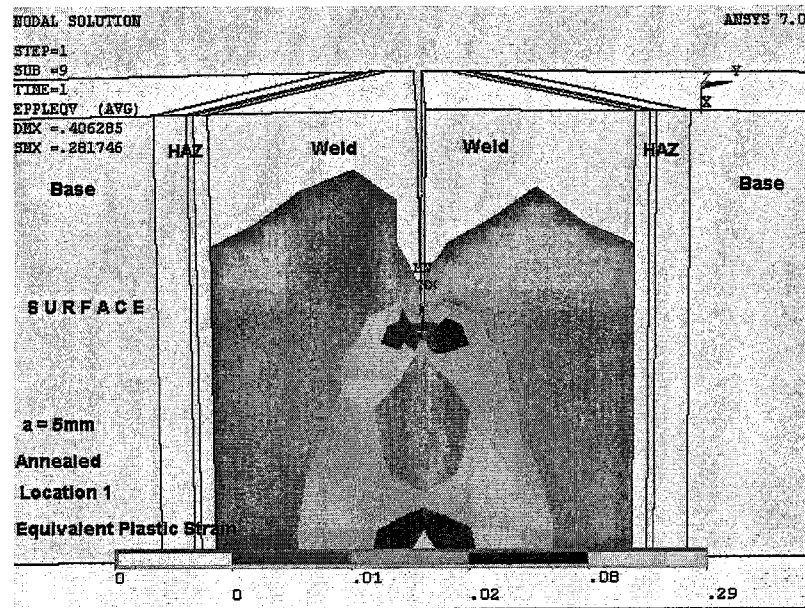
Figure 10.60. Equivalent plastic strain distribution (a) on the surface and (b) in the center of the under-matched model for 5.85 mm crack length in the crack location 4.

10.2.3. Annealed Models

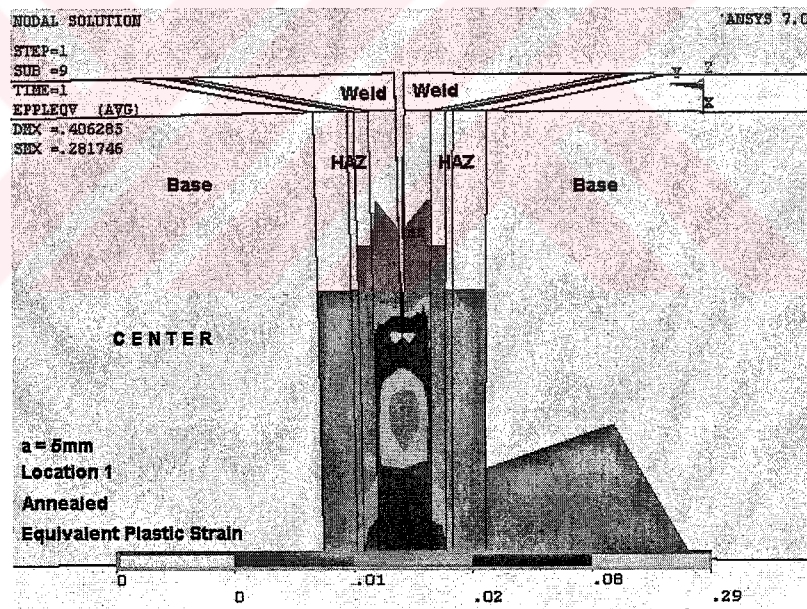
Figures from 10.61 to 10.68 show the equivalent plastic strain extension on the surface and in the center of the annealed models with 5 mm and 5.85 mm crack lengths for all crack locations. Mechanical properties of all regions were changed by annealing treatment. The effect of the regions with different strengths on plastic deformation can be recognized in the following figures. In annealed models, larger plastic strain is occurred compared with even-matched and under-matched models.

In Figures 10.61 and 10.62, equivalent plastic strain extension on the models with 5 mm and 5.85mm crack lengths can be observed for crack location 1. Crack location is in the weld metal. There is a gross yielding over uncracked ligament. Plastic deformation was shielded by HAZ. Thus, plastic flow lines cannot enter the HAZ and base metal on the surfaces of the models. Figures 10.61a and 10.62a show this situation for 5 mm and 5.85 crack lengths. In the center, plastic deformation occurs in HAZ for both crack lengths. In the shortest crack length, very small amount of plastic deformation can be observed in the base metal. Plastic strain has discontinuous lines when they pass the HAZ region (Figure 10.61b). In the longest crack lengths, the same situation observed but the values of plastic strain is larger than that of 5 mm crack length (Figure 10.62b). Constraint at HAZ border increases the stress triaxiality at crack tip. Plastic deformation arises extensive values around crack tip for longer crack length, plastic strain exhausts earlier.

Figures 10.63 and 10.64 show the equivalent plastic strain extension on the surface and in the center of annealed models with 5 mm and 5.85 mm crack lengths on the crack location 2 where is between HAZ and weld metal. Plastic strain cannot across the HAZ on the surfaces of the models with 5 mm and 5.85 mm crack lengths (Figure 10.63a) but they pass the HAZ with discontinuous plastic flow lines in the center of the models. Plastic strain intends to flow into weld metal because weld metal is softer than HAZ and base metal. Thus, bending character of the models forces plastic strain to flow into weld metal and plastic strain exhausts earlier.

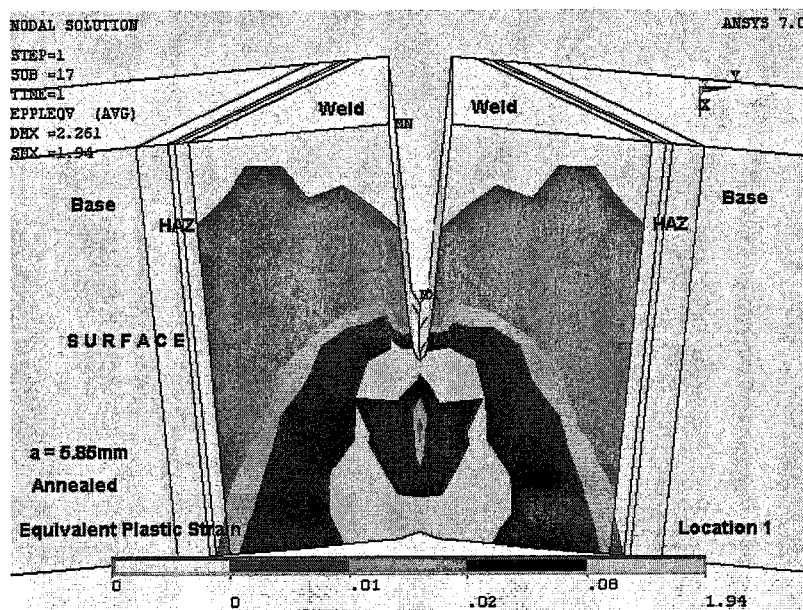


(a)

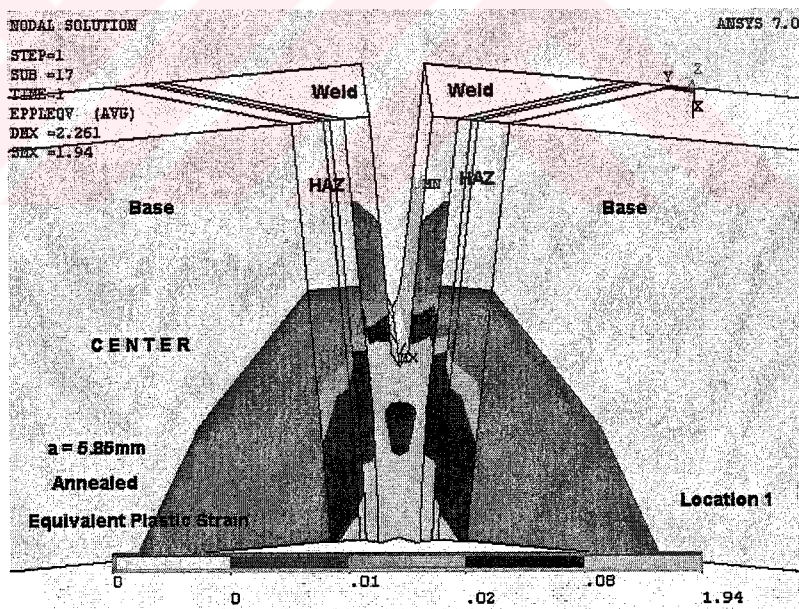


(b)

Figure 10.61. Equivalent plastic strain distribution (a) on the surface and (b) in the center of the annealed model for 5 mm crack length in crack the location 1.

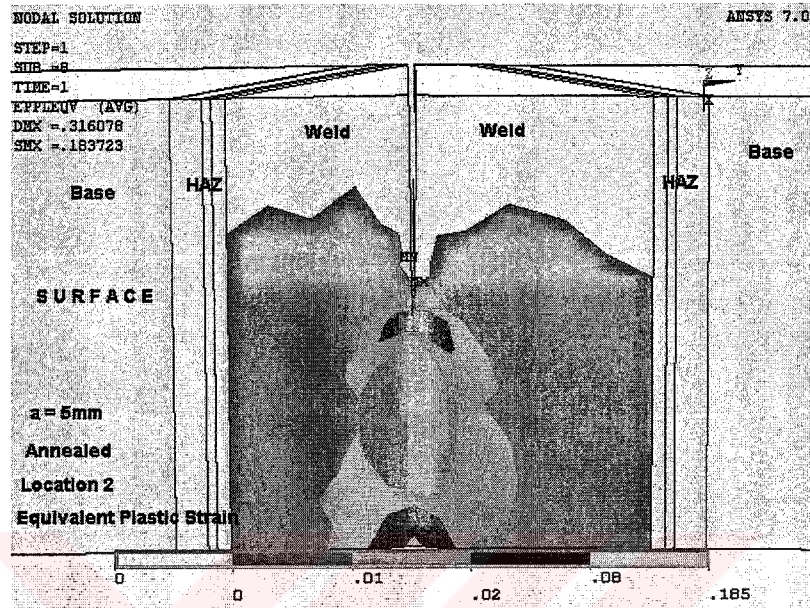


(a)

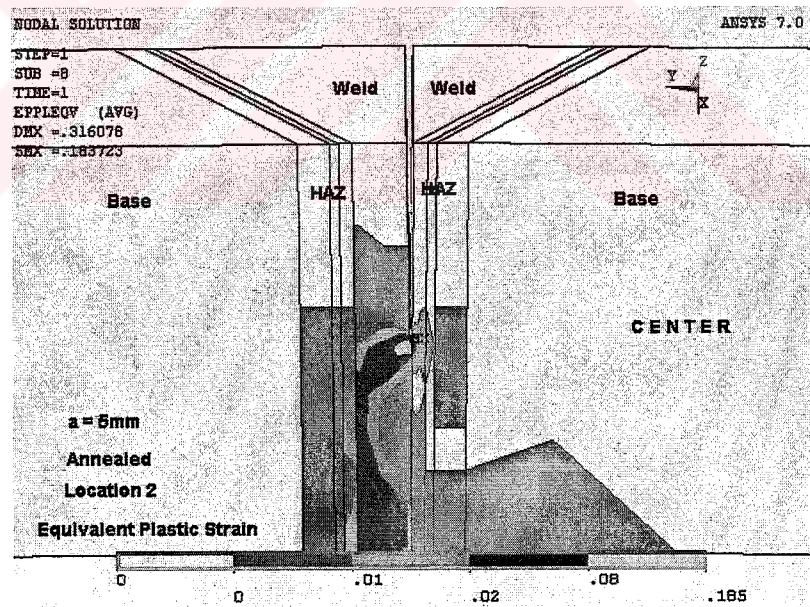


(b)

Figure 10.62. Equivalent plastic strain distribution (a) on the surface and (b) in the center of annealed model for 5.85 mm crack length in the crack location 1.

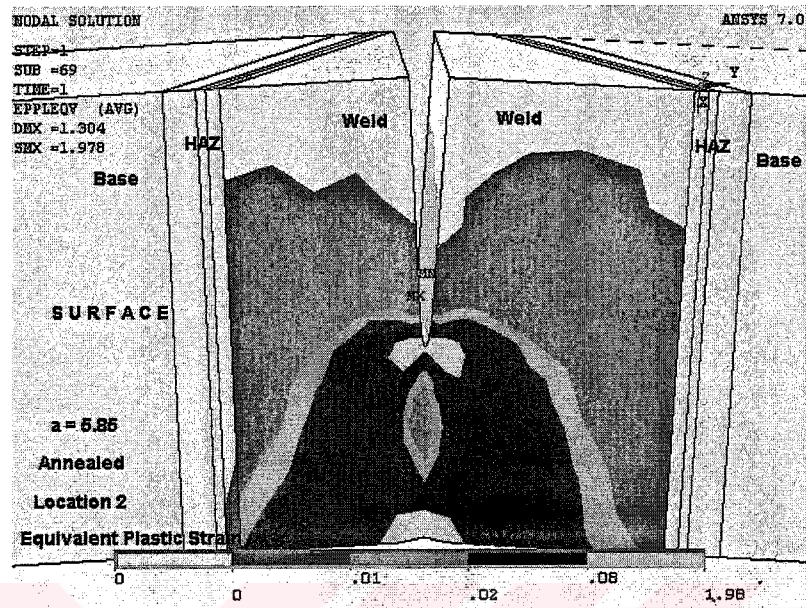


(a)

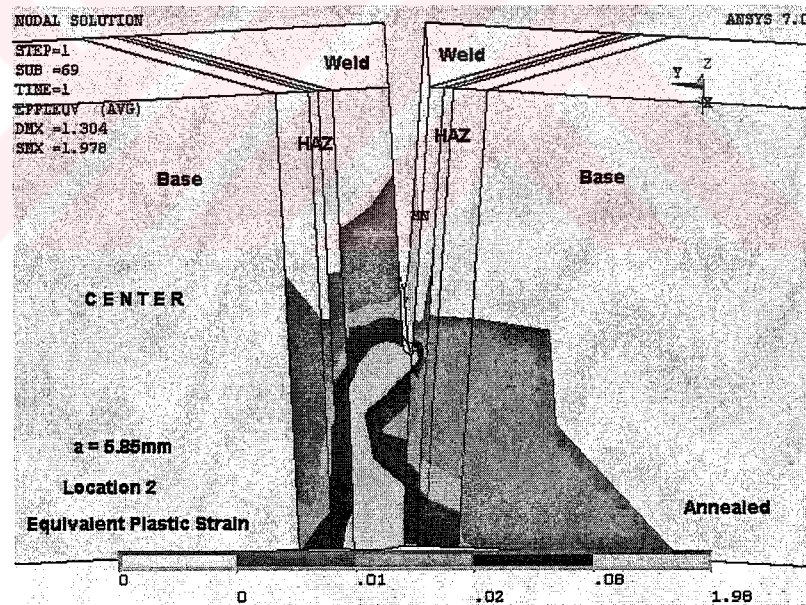


(b)

Figure 10.63. Equivalent plastic strain distribution (a) on the surface and (b) in the center of the annealed model for 5 mm crack length in the crack location 2.



(a)

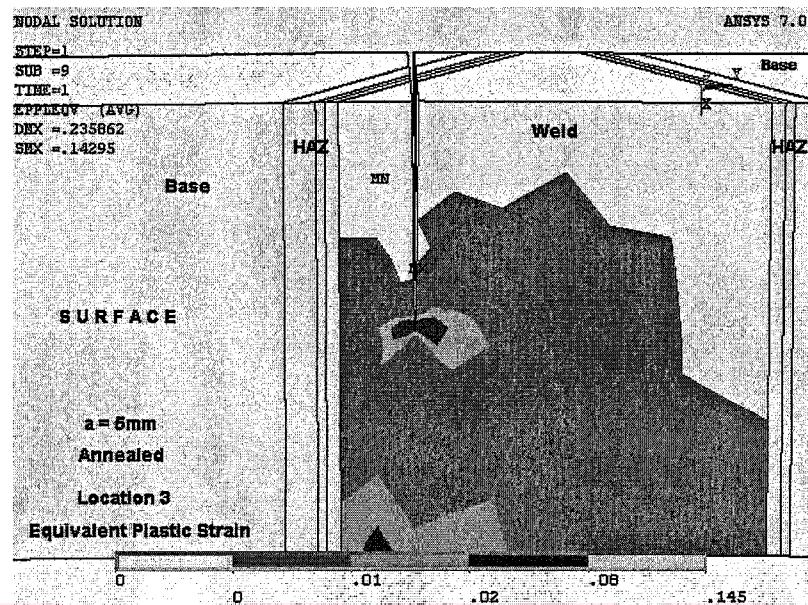


(b)

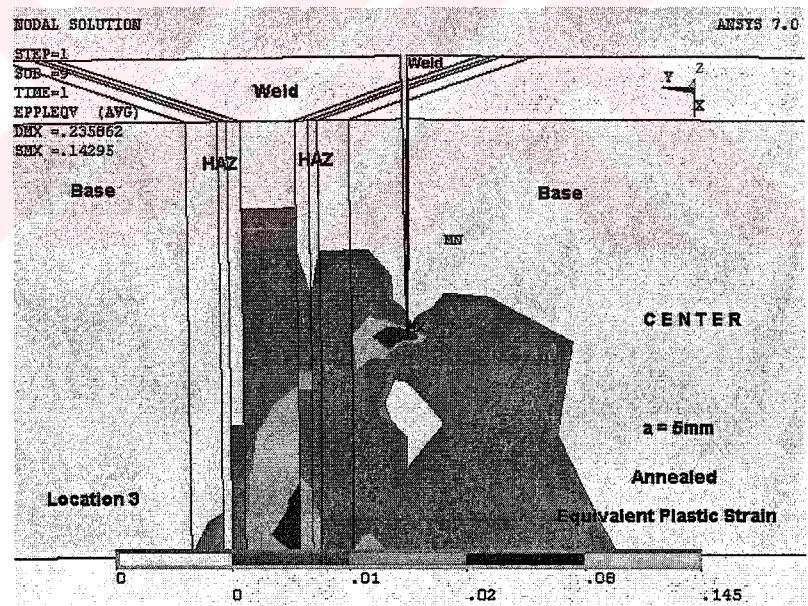
Figure 10.64. Equivalent plastic strain distribution (a) on the surface and (b) in the center of annealed model for 5.85 mm crack length in the crack location 2.

Figures 10.65 and 10.66 depict the equivalent plastic strain extension on the surface and in the center of the annealed models with 5 mm and 5.85 mm crack lengths on the crack location 3. Cracks pass through the base metal, weld metal and HAZ. In the shortest crack length, plastic strain cannot pass the HAZ and spreads into weld metal on the surface of the model but in 5.85 mm crack length situation, plastic strain passes the HAZ and reaches the base metal (Figure 10.65a and 10.66a). In Figures 10.65b and 10.66b, plastic strain passes the HAZ with discontinuous flow lines. In the longest crack length, larger plastic strain occurs than that of the shortest crack length. Hindrance to plastic deformation becomes more effective for longer crack length due to HAZ's higher work hardening exponent, because deformation strengthens the HAZ more than the weld metal and the base metal. This situation increase the stress triaxiality at crack tip.

In Figures 10.67 and 10.68 equivalent plastic strain distribution on the surface and in the center of the annealed models with 5 mm and 5.85 mm crack lengths on the crack location can be seen. Cracks cut the base metal, HAZ and weld metal on this location 4. On the surface of the model with 5 mm crack length, small amounts of plastic strain crosses the HAZ but equivalent plastic strain crosses the HAZ with discontinuous flow lines for the longest crack length (Figure 10.67a and 10.68a). As seen in Figure 10.67b, in the center of the model with 5 mm crack length, large amount of equivalent plastic strain does not occur in the HAZ. In the largest crack length situation, equivalent plastic strain spreads into base metal and weld metal passing through the HAZ with discontinuous flow lines in the center of the model (Figure 10.68b). This obstruction to plastic deformation at HAZ causes an increase in triaxial stresses at crack tip.

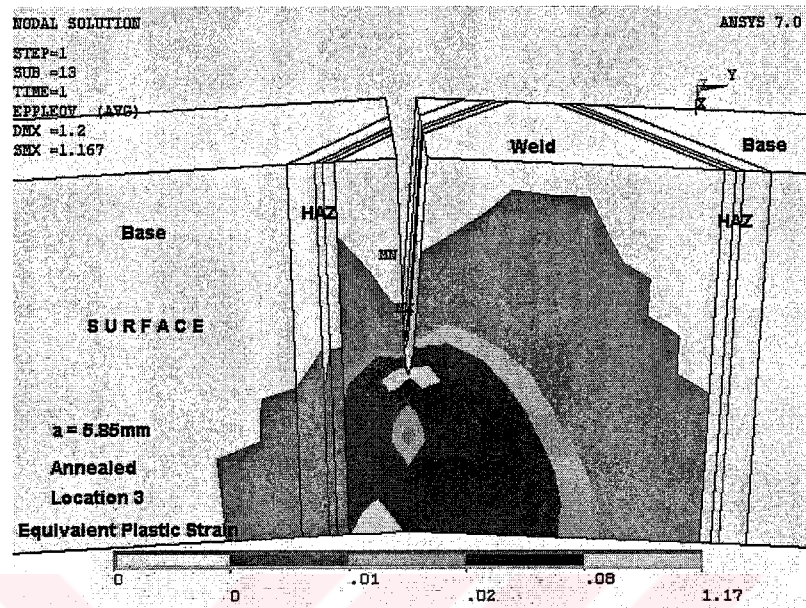


(a)

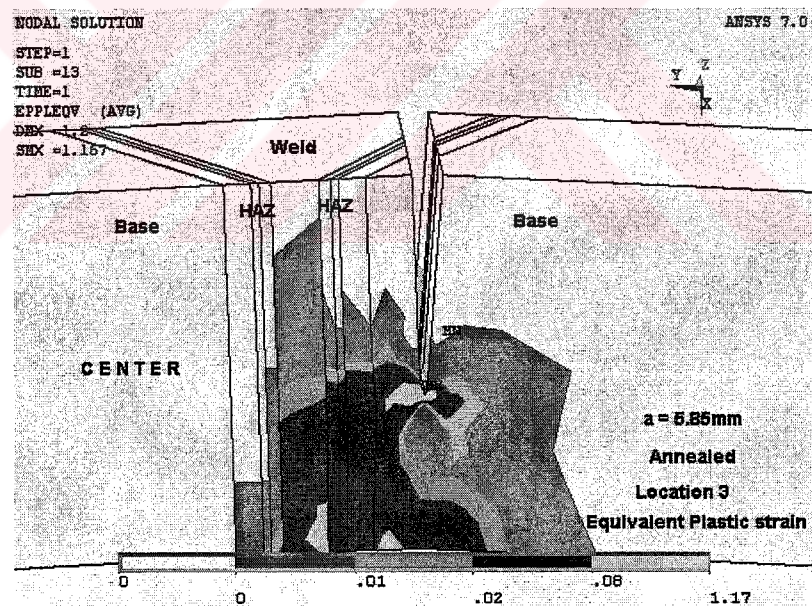


(b)

Figure 10.65. Equivalent plastic strain distribution (a) on the surface and (b) in the center of the annealed model for 5 mm crack length in the crack location 3.

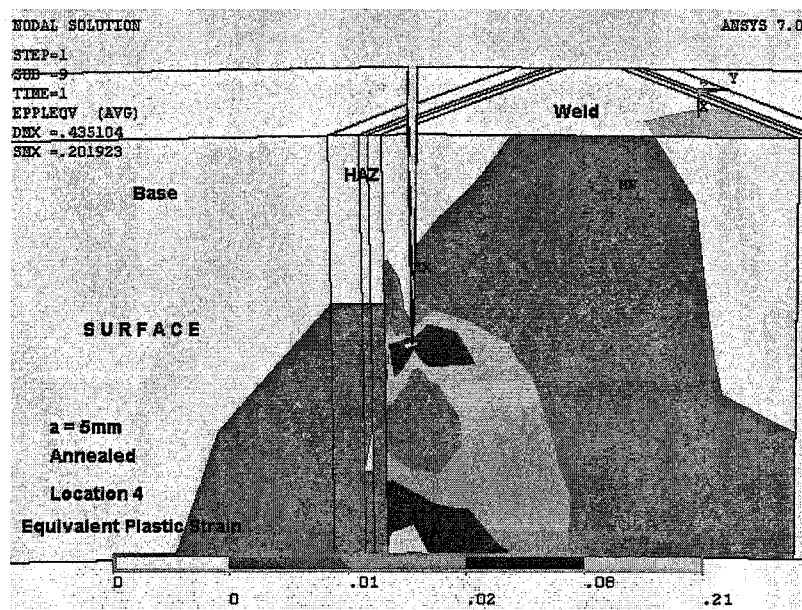


(a)

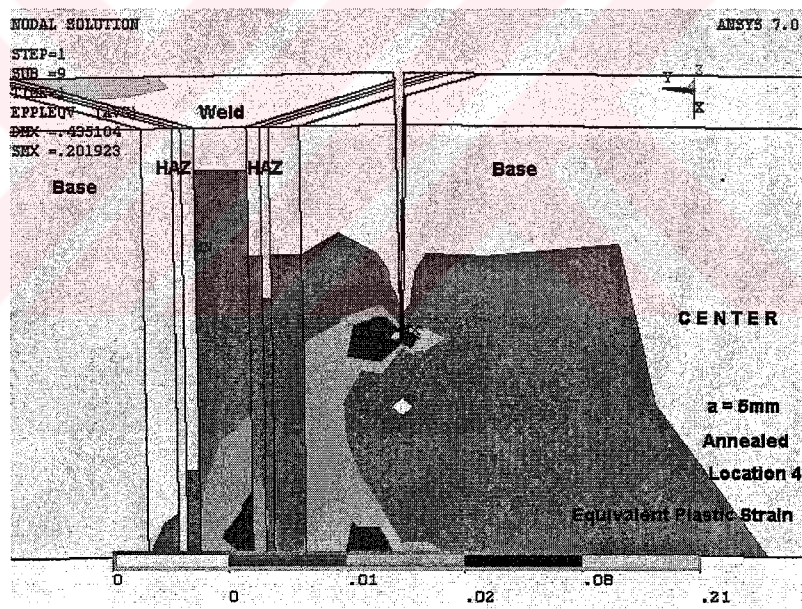


(b)

Figure 10.66. Equivalent plastic strain distribution (a) on the surface and (b) in the center of annealed model for 5.85 mm crack length in the crack location 3.

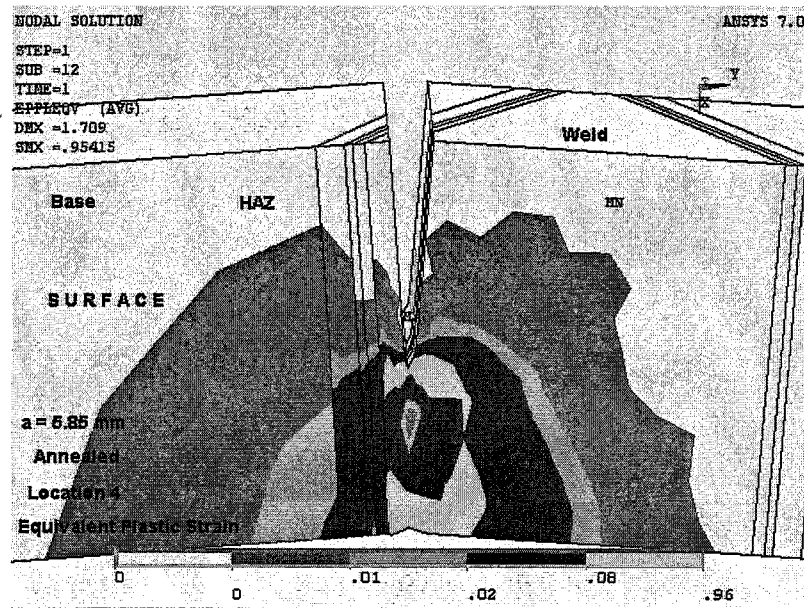


(a)

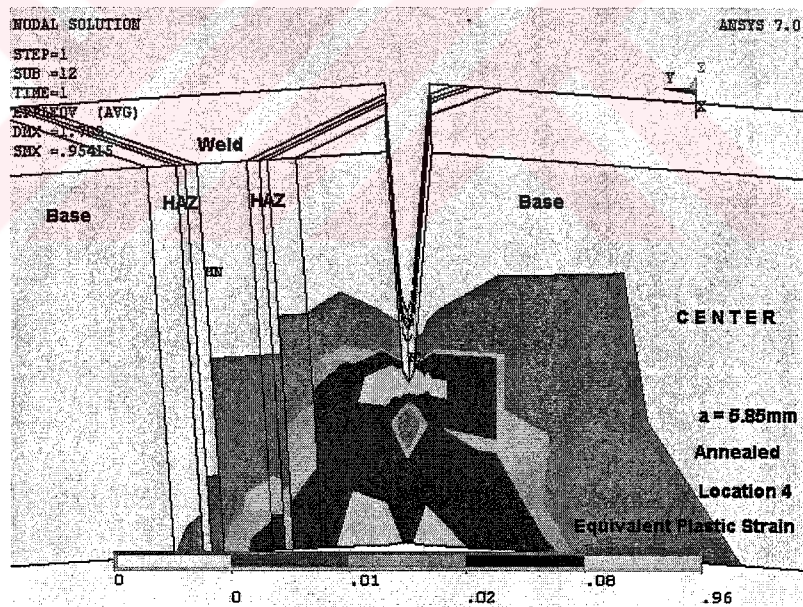


(b)

Figure 10.67. Equivalent plastic strain distribution (a) on the surface and (b) in the center of the annealed model for 5 mm crack length in the crack location 4.



(a)



(b)

Figure 10.68. Equivalent plastic strain distribution (a) on the surface and (b) in the center of annealed model for 5.85 mm crack length in the crack location 4.

CHAPTER ELEVEN

CONCLUSIONS

1. The difference in mechanical properties of weld metal, HAZ and base metal was investigated and it is determined that weld metal and base metal have distinctive modulus of elasticity. In addition, true stress – true strain curves of weld metal, HAZ and parent metal appear different. All of these affect the crack tip plasticity and stresses during crack propagation process and bending character of the specimens.
2. Graphite sizes in the weld metal and in the base metal are very distinctive. Graphites are known as crack arresters so they affect the crack tip blunting with their different diameters. On the other hand, cracks initiate graphite/matrix interface, so their sizes affect the crack initiation process.
3. In load vs. CMOD curves of crack location 2, 3 and 4 apart from weld metal region (crack location 1), load values decrease dramatically after some peak values and the increases in compliance are more significant for each locations.
4. In load vs. crack length diagrams, crack growth starts at higher load values for the crack locations 3 and 4 than that of crack locations 1 and 2. This indicates that loss of ductility in deformation process for the cracks cut through the HAZ.
5. In J-integral vs. crack growth curves, weld metal shows the maximum resistance to crack propagation. On the contrary, base metal is the lowest resistant region to crack propagation. The other crack locations cut through the base metal, HAZ and weld metal have the average J-integral toughness values.

6. In FE analyses, higher stress triaxiality values occur at crack tip in the center of even-matched (nodular iron) models for all crack lengths than that of under-matched and annealed models, and these σ_h / σ_e values are generally diminished with the decreasing values of crack length. Loss of constraint can occur if plasticity extends to a free surface. In the case of a ductile layer (weld metal) between HAZs, additional constraint of the plastic zone occurs when plasticity extends across the weld metal. This constraint also results in higher triaxial stresses ahead of crack tip. The increasing constraint limits the crack tip blunting, thereby raising local crack tip stresses.
7. Stress triaxiality values increase with increasing crack length because HAZ has the higher work hardening exponent than that of base metal and weld metal, so strength of HAZ increases by plastic deformation or crack growth. Thus, higher mismatch occurs and higher triaxial stresses take place at crack tip.
8. Annealing treatment provides slightly lower stress triaxiality values than that of under-matched models for all crack lengths. Significant decrease in stress triaxiality values around crack tip could not be obtained by annealing treatment because yield strengths of the HAZ, base and weld metal decreased proportional to original state so mismatch factor did not change significantly. In this manner, annealing process must be discussed as expensive and prolonged treatment in order to promote higher crack propagation resistance.
9. In FE analyses, equivalent plastic strain values have lower amounts at crack tip in the center of the even-matched models for all crack lengths than that of under-matched and annealed models. This means that crack tip blunting process is more effective for under-matched and annealed models than that of even-matched models.
10. In equivalent plastic strain distribution on the models, plastic zone of the weld metal is larger than that of the base metal and HAZ. When the mechanical property of the weld metal is analysed for the structure, the under-matched

welded metal may have greater strain, which results in the crack opening driving force increasing. The opposite conclusion can be reached for the HAZ and base metal. Dissimilarity in the yield strength of the weld metal, HAZ and base metal clearly affects the plastic strain extension. When the plastic zone expands to the HAZ, the development of the plastic zone to base metal is suppressed. Hindrance in plastic deformation shielding by HAZ also causes high local strain hardening and high local magnification in the strain rate. All of these result in increasing the tendency of brittle fracture.

11. The most important finding is that using the under-matched weld metal improves the fracture resistance of the welded material although its yield strength is about 33% lower than that of cast iron material.



CHAPTER ELEVEN

FURTHER WORK

Annealing treatment of under-matched weldments did not change the stress triaxiality and equivalent plastic strain values significantly. In future work, fracture toughness of over-matched nodular iron weldment with cracks on different locations should be investigated. It is expected that the character of plastic strain expansion in over-matched welded material will be different, so amount of the triaxial stresses occurred at crack tip will change. Annealing treatment of over-matched weldments may change the stress triaxiality and equivalent plastic strain values significantly. The effect of different regions with various mechanical properties should be examined in over-matched welds.

REFERENCES

- Angus, H.T. (1967). Cast Iron: Physical and Engineering Properties, (2nd ed.), Butterworths Inc.
- American Society for Metals. (1977). Source Book on Ductile Iron. Metals Park, OH. pp. 254-292
- American Society for Metals. (1988) Ductile Iron, Metals Handbook, Ductile Iron, (9th ed.), Vol. 15.
- American Society for Metals. (1989). Metals Handbook. (9th ed.) Vol. 6 Welding, Brazing and Soldering. Metals Park, OH. pp. 307-319.
- American Society for Metals. (1990). Metals Handbook. (10th ed.). Vol. 1 Metals Park, OH. pp. 33-55.
- ASTM Committee. (1991). Standard Test Method for J, A Measure of Fracture Toughness. (E813-89).
- AWS, The American Welding Society. (1983). Welding Handbook. (7th ed.) Miami, FL. Vol.4.
- AWS, The American Welding Society. (1989). Guide for Welding Iron Casting. 550N.W. Lejeune Road, P.O. Box.351040, Miami Florida 33135.USA.

British Cast Iron Research Association (1981). BCIRA Broadsheet 157-2, Stress/Strain Behaviour of Nodular and Malleable Cast Irons.

Bishel, R.A. & Conaway, H.R. (1976) Flux-cored Arc Welding for High- quality joints in Ductile Iron, Transactions, American Foundrymen's Society, Vol. 84, pp. 124-133.

Bornstein, H. (1957). Progress in Iron Castings, The Charles Edgar Hoyt Lecture, Transactions of the American Foundrymen's Society, Vol 65, p 7.

Brocks, W. & Künecke, G. (1991). On the Influence of Triaxiality of the Stress State on Ductile Tearing Resistance, Defect Assessment in Components-Fundamentals and Applications, ESIS/EGF9, J.G. Blauel and K.-H. Schwalbe, Eds., Mechanical Engineering Publications, London, United Kingdom, pp. 189-201

Caine, J. B. (1984). Design of Ferrous Castings, American Foundrymen's Society, Des Plaines, IL, USA

Castolin Sociele Anongome. (1985). Cast Iron. Technical Report. pp. 1-20

Cheung, S. & Luxmoore, A.R. (2002). A Finite Element Analysis of the Stable Crack Growth in an Aluminum Alloy. Engineering Fracture Mechanics. v.70 no.9 pp. 1153-1169.

Cox, G.J. (1973). The Impact Properties of Different Types of Ferritic Spheroidal Graphite Cast Iron. British Foundryman, 1973.

Crews, D.L. (1974). Quality and Specifications of Ductile Iron. Transactions, American Foundrymen's Society, Vol. 82, pp. 223-228.

Davila, M.A., Olson, D.L. & Freese, T.A. (1977). Submerged Arc Welding of Ductile Iron. Transactions, American Foundrymen's Society, Vol 85, pp. 79-86.

- Denys, R. M. (1990). Implications of Overmatching / Undermatching of Weld Metal Yield Strength. AWS. Houston. USA.
- El-Banna, E.M. (1999). Effect of Preheat on Welding of Ductile Cast Iron. Materials Letters, 41, pp. 20-26.
- El-Banna, E.M., Nageda, M.S. & El-Saadat, M.M.A. (1999). Study of restoration by welding of Pearlitic Ductile Cast Iron. Materials Letters, v. 42, pp. 311-320.
- Elliot, R. (1988). Cast Iron Technology. Butterworth and Co., London.
- Everest, A.B. (1950). Spheroidal-Graphite Cast Iron. Foundry Trade Journal, pp. 57-64.
- Fu, J.Q. & Shi, Y. W. (1996). Effect of Cracked Weld Joint and Yield Strength Dissimilarity on Crack Tip Stress Triaxiality. Theoretical and Applied Fracture Mechanics, 25 pp. 51-57.
- Fuller, A.G. (1977). Effect of Graphite Form on Fatigue Properties of Pearlitic Ductile Irons. Transactions, American Foundrymen's Society, Vol. 85, pp. 527-536.
- Gilbert, G.N.J., (1957). Tensile and Fatigue Tests on Normalized Pearlitic Nodular Irons, Journal of Research, British Cast Iron Research Association, Vol. 6, No. 10, pp. 498-504.
- Gilbert, G.N.J. (1974). Engineering Data on Nodular Cast Irons, British Cast Iron Research Association, Birmingham, England.
- Gordon, JR & Wang, Y.-Y. (1992). The Effect of Weld Metal Mismatch on Structural Integrity Assessments, EWI Report J6154-6-92.

- Hafiz, M. (2003). Mechanical Properties of SG-Iron Subjected to Variable and Isothermal Austempering Temperatures Heat Treatment. Materials Science and Engineering A. Vol.340 No.1-2. pp. 1-7.
- Hallen, G. (1984). Some Aspects on the Formation of Microstructure in Multipass Welds in Ferritic Ductile Iron. 3rd. Int. Symp. on the Physical Metallurgy of Cast Irons. Stockholm, Sweden, Aug., 1984. pp. 457-465.
- Harding, R.A. (1987). Progress in Joining Iron Castings. British Foundrymen, pp 444-455.
- Haverstraw, R.C. & Wallace, J.F. (1966). Fatigue Properties of Ductile Iron. Gray & Ductile Iron News, Gray & Ductile Iron Founders' Society, Inc., pp. 5-19.
- Hencky, H. (1943). Ermüdung, Bruch, Plastizität (Fatigue, Fracture, Plasticity), Stahlbau, Vol.16, pp. 95-97.
- Heuser, A., Twickler, R. & Dahl, W. (1987). Experimental Investigations of the Failure Behaviour of Welded Joints and its Numerical Simulation by Using Elastic-Plastic Finite Element Calculations. The Fracture Mechanics of Welds, EGF Pub.2 (Edited by J.G. Blauel and K.-H. Schwalbe, Mechanical Engineering Publications, London, United Kingdom, pp. 97-124.
- Hornet P. & Kocak M (1994). Fracture of Bi – material joints: Effect of Strength Mismatch on Crack Resistance Curves. 10th European Conference on Fracture, ECF10, Berlin, FRG, 20-23 September.
- Huke, E. E. & Udin, H. (1953). Welding Metallurgy of Nodular Cast Iron. Weld J. 32. pp. 378-385.

Hutchinson, J.W. (1968) Singular Behavior at the End of a Tensile Crack in a Hardening Material. Journal of the Mechanics and Physics of Solids, Vol.16, pp. 13-31.

Iron Casting Society. (1981). Iron Casting Handbook. pp. 599-665.

Ishizaki, K., Moram, J.G., Marifler, S. L. & Davila, A. (1984). Simulation Study on Ductile Cast Iron welding by Austenitic Filler Metal. Trans. Of Japan Welding Society.15 (2) pp. 3-9

Isleib, C. & Savage, R. (1957). Ductile Iron-Alloyed and Normalized. Transactions, American Foundrymen's Society, Vol. 65 pp.28-39.

Janowak, J.F., Alagarsamy, A. & Venugopalan, D.(1990). Fatigue Strength of Commercial Ductile Irons. Transactions, American Foundrymen's Society, Vol. 98, pp. 90-123.

Karsay, S. I. (1972) Ductile Iron II, Quebec Iron and Titanium Corporation.

Kelly, J. J., Bishel, R. A. & Vision, R. K. (1985). Welding of DI with Ni-Fe_Mn Filler Metal. Welding J. 64 pp. 79s-85s.

Kim, Y-J. & Schwalbe, K. (2001). Mismatch Effect on Plastic Yield Loads in Idealised Weldments I. Weld Centre Cracks. Engineering Fracture Mechanics, 68. pp. 163-182.

Kim, Y.-J. (2002). Experimental J Estimation Equations for Single-Edge-Cracked Bars in Four-Point Bend : Homogeneous and Bi-Materials Specimens. Engineering Fracture Mechanics. 69. pp. 793-811.

- Kinney, K. E., Bradley, W.L. & Gerhardt Jr. P.C. (1984), An evaluation of the Toughness of Ductile Iron vs. Cast Steel Using Modified Charpy Test Specimens. Transactions, American Foundrymen's Society, Vol. 92, pp. 239-250.
- Kirk, M.T., & Dodds, R.H. (1991). An Analytical and Experimental Comparison of J_i Values for Shallow Through and Part Through Surface Cracks. Engineering Fracture Mechanics, Vol. 39, No. 3, pp. 535-551.
- Kiser, S.D. (1977). Production Welding of Cast Irons. Transactions, American Foundrymen's Society, Vol 85, pp 37-42.
- Kiser, S. D. & Irving, B. (1993). Unraveling the Mysteries of Welding Cast Iron. Welding J. pp. 39-44.
- Kocak, M., Schwalbe, K.-H., Chen, L. & Gnriss, G. (1988). Effect of notch position and weld metal matching. GKSS 88/E/74, U.K., 21-24 November.
- Kocak, M., Yao, S., Chen, L. & Schwalbe, K.-H. (1989). Evaluation of HAZ Toughness by CTOD and Tensile Panels. Proc. of the European Symposium on EPFM, Elements of Defect Assessment, Freiburg, FRG, Oct. 9-12.
- Kocak, M., Es-Souni, M., Chen, L. & Schwalbe, K.-H. (1989). Microstructure and Weld Metal Matching Effects on HAZ Toughness. Proc. 8th Int. Conf. On Offshore Mech. And Arctic Eng. (OMAE). Vol.3 March.
- Kocak, M., Knaack, J. & Schwalbe, K.-H. (1990). Fracture Behaviour of Undermatched Weld Joints. Proc. Of the 9th Int. Conf. On Offshore Mechanics and Arctic Eng. (OMAE). Vol. 3B. pp. 453-459.
- Kocak, M. & Denys, R. (1995). CTOD and Wide Plate Testing of Welds with Particular Emphasis on Mis-matched Welded Joints. Proc. of the 2nd Intermediate

Meeting of the IIW Sub. Comm. X-F 24 April 1995, GKSS Research Center. pp. 120-137.

Kruzic, J.J., McManey, J.M., Canon, R.M. & Ritche, R.O. (2004). Effects of Plastic Constraint on the Cyclic and Static Fatigue Behavior of Metal/Ceramic Layered Structures. Mechanics of Materials, V.36, pp. 57-72

Lin, S.C., Lui, T.S. & Chen, L.H. (2000). Effect of Nodularity on Resonant Vibration Fracture Behavior in Upper Bainitic and Ferritic Cast Irons. Metallurgical and Materials Transactions A, vol. 32A, pp.2193-2203.

Marrow, T.J. & Çetinel, H. (2000). Short Fatigue Cracks in Austempered Ductile Cast Iron (ADI). Fatigue and Fracture of Engineering Materials and Structures. Vol.23 No.5, pp. 425-434.

Marrow, T.J., Çetinel, H., Weir, N. & Brough, I. (2000). Observation of Retained Austenite by Electron Backscatter Diffraction in Austempered Ductile Cast Iron (ADI). Heat Treat 2000. 20th ASM Heat Treating Conference, St Louis, Missouri, USA, pp. 491-496.

Marrow, T.J., Çetinel, H., Al-Zalmah, M., MacDonald, S., Withers, P.J. & Walton, J. (2002). Fatigue Crack Nuclei in Austempered Ductile Cast Iron. Fatigue and Fracture of Engineering Materials and Structures, Vol.25 No.7, pp. 635-648.

Marston. G.J. (1990). Better Cast Than Fabricated. The Foundryman, pp. 108-113.

Matharu, I.S. & Selby, K. (1990). The Charpy v-notch and tensile properties of a ferritic ductile iron welded using MIG and FCAW methods. BCIRA Research and cast metals practice, pp. 195-201.

McClintock, F.A. (1968). A Criterion for Ductile Fracture by the Growth of Holes. Transactions of ASME, Journal of Applied Mechanics, Vol.35, pp. 363-371.

McKeown, D. (1990). Foundry Trade J. ESAB Group. 164. pp. 157-161.

McMeeking, R.M. & Parks, D.M. (1979). On the Criteria for J-Dominance of Crack-Tip Fields in Large Scale Yielding. Elastic-Plastic Fracture, ASTM STP 668, American Society for Testing and Materials, Philadelphia, pp. 175-194.

Medana, R., Natale, E. & Remondino, M.S. (1978). High Strength Welding of Ductile Iron Castings. Transactions, American Foundrymen's Society, Vol 86, pp. 611-616.

Megahed, H. (1995). Effect of Weld Heat Input, Number of Passes and Interpass Temperature on the Mechanical and Structural Properties of Ductile Cast Iron. J. Eng. Appl. Sci., Fac. Eng., Cairo University 42 pp. 931-947.

Minkoff, I. (1983). The Physical Metallurgy of Cast Iron. John Wiley&Sons Ltd. New York, NY.

Morrison, J. C. & Smith, K.J. (1989). Cost effective substitution of steel components by SG ductile iron. The Foundryman, pp 121-129.

Mukae, S., Nishio, K., Katoh, M. & Nakamura, N. (1990) Impact Characteristics of Diffusion Bonds of Ferritic Spheroidal Graphite Cast Iron. Transactions, Japan Welding Society, Vol 21, pp. 41-51.

Nichols, R.W. (1984). The Use of Fracture Mechanics as an Engineering Tool. The ICF Honor Lecture, ICF 6, New Delhi, India.

Nippes, E. F. (1960). The Heat Affected Zone of Arc Welded Ductile Iron. Weld J. 39 pp. 465-472.

- Nishio, K. Katoh, M. & Mukae, S. (1988). Fatigue Strengths of Diffusion Bonds of Spheroidal Graphite Cast Irons. Transactions, Japan Welding Society, Vol 19, pp. 17-27.
- O'Dowd, N. P. & Shih, F. (1991). Family of Crack-Tip Fields Characterized by A Triaxiality Parameter-I. Structure of Fields. J. Mech. Phys. Solids vol. 39, No.8. pp. 989-1015.
- Ogi, K., Jin, Y. C. & Loper Jr., C. R. (1988). A Study of Some Aspects of the Austenitization Process of Spheroid Graphite Cast Iron. AFS Trans. pp. 75-82.
- Onsøiew, M.I., Grong, Ø., Gundersen, Ø. & Skaland, T. (1999). A Process Model for the Microstructure Evolution in Ductile Cast Iron: Part I. The Model. Metallurgical and Materials Transactions A vol. 30A, pp. 1053-1068.
- Palmer, K.B. & Gilbert, G.N.J. (1953). The Fatigue Properties of Nodular Cast Iron. Journal of Research, British Cast Iron Research Association, Vol. 5, No. 1, pp.2-15.
- Palmer, K.B. (1970). Fatigue Properties of Cast Irons. Engineering Properties and Performance of Modern Iron Castings. British Cast Iron Research Association, Birmingham, England.
- Palmer, K.B. (1988). The mechanical and physical properties of engineering grades of cast iron at subzero temperatures. British Cast Iron Research Association.
- Parks, D.M. & Wang, Y.-Y. (1988). Elastic-Plastic Analysis of Part-through Surface Cracks Analytical, numerical and experimental Aspects of Three Dimensional Fracture Processes. A.J. Rosakis, K. Ravi-Chandar, and Y. Rajapakse, Eds., ASME AMD-Vol.91, American Society of Mechanical Engineers, New York, NY, pp. 19-32.
- Pease, G. R. (1960). The Welding of Ductile Iron. Welding J. 39 pp. 15-95.

Petrovski, B. & Sedmak, S. (1990). Evaluation of Crack Driving Force for HAZ of Mismatched Weldments Using Direct J Integral Measurements in Tensile Panels. Proc. Of the Welding-90, Int. conf. Ed. By M. Kocak. 22-24 October 1990. GKSS-Research Centre, Geesthacht, F.R. Germany. pp. 341-353.

Petrovski, B. Kocak, M. & Sedmak, S. (1991). Fracture Behavior of Undermatched Weld Joint With Short Surface Crack. OMAE, Vol. III-A Materials Engineering., ASME, pp. 101-107.

Petrovski, B. & Kocak, M. (1994). Evaluation of the Fracture Behaviour of Strength Mis-Matched Steel Weld Joints with Surface Cracked Tensile Panels and SENB Specimens. Mis-Matching of Welds, ESIS 17 (Edited by K.-H. Schwalbe and M. Kocak). Mechanical engineering Publications, London. pp. 511-536.

Plenard, E. (1962). Cast Iron Damping Capacity, Structure and Related Properties. Transactions, American Foundrymen's Society, Vol. 70, pp. 298-305.

Plenard, E. (1966). Damping Capacity of Cast Iron. Foundry Trade Journal, pp. 541-549.

QIT-Fer et Titane Inc. (1990). A Design Engineer's Digest of Ductile Iron, 7th Edition, Montreal, Quebec, Canada.

Reed, R.P., Kasen, M. B. McHenry, H. I., Fortunko, C. M. & Read, D. T. (1984). Fitness-for-Service Criteria for Pipeline Girthweld Quality. Welding Res. Council Bul. 296 July.

Rice, J.R. (1968). A Path Independent Integral and the Approximate Analysis of Strain Concentration by Notches and Cracks. Journal of Applied Mechanics, Vol.35 pp. 379-386.

- Rice, J.R. & Rosengren, G.F. (1968). Plane Strain Deformation Near a Crack Tip in a Power Law Hardening Material. Journal of Mechanics and Physics of Solids, Vol.16, pp. 1-12.
- Rice, J.R. & Tracey, D.M. (1969). On the Ductile Enlargement of Voids in Triaxial Stress Fields. Journal of Mechanics and Physics of Solids, Vol.17, pp. 201-217.
- Roehrig, K. (1978). Thermal Fatigue of Gray and Ductile Irons. Transactions, American Foundrymen's Society, Vol. 86, pp. 75-88.
- Satoh, K. & Toyoda, M. (1975). Joint Strength of Heavy Plates with Lower Strength Weld Metal. Welding Journal Research Supplement September. pp. 311-319.
- Schwalbe, K.-H. & Cornec, A. (1991). The Engineering Treatment Model (ETM) and its Practical Application. Fatigue and Engineering of Materials and Structures. Vol. 14, pp. 405-412.
- Schwalbe, K.-H. & Gruter, L. (1991). Application of the Engineering Treatment Model (ETM) to the Prediction of the Behavior of a Circumferential Cracked. IUTAM Symposium, Lulea, Sweden, June 10-14, pp. 1125-1134.
- Sedmak, S., Radovi, A. & Nedeljkovic L. (1979). The Strength of Welds in HSLA Steel After Initial Plastic Deformation. In Mechanical Behaviour of Materials. Proc. Of the 3rd Int. Conf. On Mech Behaviour of Materials, Pergamon Press, Oxford Vol3. pp. 435-446.
- SG Iron Producers Association. (1970). The Joining and Fabrication of Nodular Iron Casting by Welding. pp. 3-34.
- Shih, C.F. & German, M.D. (1981). Requirements for a One Parameter Characterization of Crack Tip Fields by the HRR Singularity. International Journal of Fracture, Vol.17, pp. 27-43.

- Shih, C.F. (1985). J-Dominance Under Plane Strain Fully Plastic Conditions: the Edge Crack Panel Subject Combined Tension and Bending. International Journal of Fracture, Vol.29, pp. 73-84.
- Siefer W. & Orths, K. (1970). Evaluation of Ductile Iron in Terms of Feasible Properties of the Material. Transactions, American Foundrymen's Society, Vol. 78, pp. 382-387.
- Simpson, B.L. (1969). History of the Metalcasting Industry, American Foundrymen's Society, Des Plaines, IL.
- Soete, W. (1978). An Experimental Approach to Fracture Initiation in Structural Steel, in Advances in Research on the Strength and Fracture of Materials (Edited by D.M.R. Taplin), Pergamon Press, Oxford Vol1. pp. 775-804.
- Sofue, M., Okada, S. & Sasaki, T. (1978). High-Quality Ductile Cast Iron with Improved Fatigue Strength. Transactions, American Foundrymen's Society, Vol. 86, pp. 173-182.
- Sommer, E. & Aurich, D. (1991). On the Effect of Constraint on Ductile Fracture. Defect Assessment in Components-Fundamentals and Applications, ESIS/EGF9, J.G. Blauel and K.-H. Schwalbe, Eds., Mechanical Engineering Publications, London, United Kingdom, pp. 141-174.
- Sumpter, J.D.G. (1987). J_C Determination for Shallow Notch Welded Bend Specimens. Fatigue Fract. Engng. Mater. Struct. Vol. 10, No. 6. pp. 479-483.
- Tang, W. & Shi, Y.W. (1995). Influence of Strength Matching and Crack Depth on Fracture Toughness of Welded Joints. Engineering Fracture Mechanics. Vol.51 No.4. pp. 649-659.

- Thaulow, C. Ranestad, Ø., Hauge, M., Zhang, Z., Toyoda, M. & Minami, F. (1997). FE Calculations of Stress Fields from Cracks Located at the Fusion Line of Weldments. Engineering Fracture Mechanics. Vol.57 No.6. pp. 637-651.
- Thaulow, Hauge, M., Zhang, Z., C. Ranestad, Ø. & Fattorini, F. (1999). On the Interrelationship between Fracture Toughness and Material Mismatch for Cracks Located at the Fusion Line of Weldments. Engineering Fracture Mechanics. Vol.64 pp. 367-382.
- The International Nickel Company (MOND) Limited. SG Iron Properties and Applications. Tillotsons (Bolton Ltd). Bolton and London.
- Toyoda, M. & Minami, F. (1989). Evaluation Procedure of Structural Reliability of Weldments Based on CTOD Results. Eighth Int. Conf. On Offshore Mechanics and Arctic Engineering (OMAE), vol.III, Editors; Salam, M.M, Bangaru, N.V. Rhee, H.C., and Toyoda M., Book no.I0285C.
- Turner, C.E. (1979). Methods for Post-yield Fracture Assessment, in Post-yield Fracture Mechanics (Edited by D.G.H. Latzko), Applied Science Publishers, London, pp. 23-210.
- Turner, C.E. & Braga, L. (1993). Energy Dissipation Rate and Crack Opening Angle Analyses of Fully Plastic Ductile Tearing, Constraint Effect in Fracture, ASTM STP 1171, E. M. Hackett, K.-H. Schwalbe and R.H. Dodds, Eds., American Society for Testing and Materials, pp. 158-175.
- Xue, H. & Shi, Y. (1998). Effects of Mechanical Heterogeneity on Plastic Zones of Welded Three-Point Specimens. Int. J. of Pressure Vessels and Piping, 75. pp. 575-580.

Venugopalan D. & Alagarsamy, A. (1990). Effects of Alloy Additions on the Microstructure and Mechanical Properties of Commercial Ductile Iron. Transactions, American Foundrymen's Society, Vol. 98, pp. 90-122.

Voigt, R.C. & LoperJR., C. R. (1983). A Study of heat affected Zone Structure in Ductile Cast Iron. Welding J. 62. pp. 82s-88s.

Voigt, R.C. & LoperJR., C. R. (1986). Welding Metallurgy of Gray and Ductile Cast Irons. Transactions, American Foundrymen's Society, Vol. 94. pp.105-112.

Wang, Y.Y.. & Gordon, J.R. (1992). The Limits of Applicability of J and CTOD Estimation Procedures for Shallow-cracked SENB specimens in Proceedings of Shallow Cracks Fracture Mechanics, Cambridge, England 23-24 September.

Ya, S. K. & Loper Jr., C. R. (1988). The Effect of Molybdenum, Copper and Nickel on the Pearlitic and Martensitic Hardenability of Ductile Cast Iron. AFS Trans. pp. 811-822.